MAGNETIC FIELD INDUCED STRAIN IN POLYCRYSTALLINE MAGNETIC

SHAPE MEMORY FOAM

By

Cassie Witherspoon

A thesis

submitted in partial fulfillment

of the requirements for the degree of

Master of Science in Materials Science & Engineering

Boise State University

May 2011

BOISE STATE UNIVERSITY GRADUATE COLLEGE

DEFENSE COMMITTEE AND FINAL READING APPROVALS

of the thesis submitted by

Cassie Witherspoon

Thesis Title: Magnetic Field Induced Strain in Polycrystalline Magnetic Shape Memory Foam

Date of Final Oral Examination: 3-3-2011

The following individuals read and discussed the thesis submitted by student Cassie Witherspoon, and they evaluated her presentation and response to questions during the final oral examination. They found that the student passed the final oral examination.

Peter Müllner, Ph.D.   Chair, Supervisory Committee

David Dunand, Ph.D.   Member, Supervisory Committee

Amy Moll, Ph.D.   Member, Supervisory Committee

The final reading approval of the thesis was granted by Peter Müllner, Ph.D., Chair of the Supervisory Committee. The thesis was approved for the Graduate College by John R. Pelton, Ph.D., Dean of the Graduate College.

ABSTRACT

Magnetic shape memory alloys (MSMA) are fascinating materials that show a recoverable shape change in a rotating magnetic field. Single crystalline MSMA's display magnetic-field-induced strains (MFIS) up to 10%. However, single crystals have inherent drawbacks such as cost and chemical segregation during production. Polycrystalline materials are easier to produce and display chemical homogeneity but display a much smaller MFIS than single crystals. It has been shown recently that adding porosity to polycrystalline Ni-Mn-Ga (i.e. metal foam) can increase MFIS.

Variables that affect the performance of polycrystalline Ni-Mn-Ga foam include phase transformation temperature, pore architecture, spatial distribution of pores, porosity, training, and magnetic anisotropy/texture. Samples were tested for MFIS and phase transformation temperatures to probe for a correlation. Single pore foam architecture with a mono-modal pore size distribution and dual pore foam architecture with a bi-modal pore size distribution were compared in terms of microstructure and magneto-mechanical behavior. Pore distributions were characterized with x-ray tomography and compared with the temperature dependent MFIS, to deduce the role of the large and small pores. Samples were systematically etched and tested for MFIS to investigate the effect of porosity on strain. Magneto-mechanical, thermo-magnetic, and thermo magneto-mechanical training effect on MFIS was also investigated.

The results are discussed in terms of a concept of a network of struts (bridging metal) with hard and soft links. Where, hard links are struts that are unable to deform. It was found that increasing porosity increased strain, confirming the hypothesis that porosity is responsible for enhanced MFIS. The porosity strain relationship indicated strut thickness is a crucial factor in determining the strain, i.e. the thicker the strut the "harder the link." The dual pore foam has much smaller struts and therefore has fewer hard links. Pore distribution affected the number and distribution of hard links. The metal is more compliant when the sample temperature approaches the phase transformation temperature. Therefore, samples with transformation temperatures close to the testing temperature contain softer links and produce more MFIS. Hard links can also be softened by training

For optimal MFIS and fatigue resistance foams of dual pore architecture with a spatially homogenous distribution of pores, high porosity (65-70%) and a martensitic phase transformation temperature close to testing temperature should be employed. Foams with such optimized microstructures and chemical homogeneity are expected to perform reproducibly and consistently.

TABLE OF CONTENTS

LIST OF TABLES

LIST OF FIGURES

LIST OF ABREVIATATIONS

Abbreviation	Description
EDS	Energy Dispersive Spectroscopy
NOL	Naval Ordinance Laboratories
Ni-Mn-Ga	nickel-manganese-gallium
NiTi	nickel-titanium
SEM	Scanning Electron Microscope
SMA	Shape Memory Alloy
MSMA	Magnetic Shape Memory Alloy
MFIS	Magnetic Field Induced Strain
VSM	Vibrating Sample Magnetometer
MMC	Magneto-Mechanical Cycle
TMC	Thermo Magneto-Mechanical Cycling
$NaAlO_2$	Sodium Aluminate
H_2SO_4	Sulfuric Acid
HCl	Hydrochloric Acid
XRD	X-ray diffraction
H/C	Heating Cooling cycle

TABLE OF SYMBOLS

Symbol	Unit	Description
I	A	Current
A	mm^2	Area
$\vec{\mu}$	J/T	Magnetic moment
m	kg	Mass
e	C	Charge of an electron
$\vec{L}$		Angular momentum
$\vec{S}$		Spin
$\vec{M}$	Am^{2}kg^{-1}	Magnetization
$\vec{B}$	A/m	Magnetic induction, magnetic flux field
μ_0	Wb/Am	Magnetic permeability of free space
$\vec{H}$	T	Applied magnetic field
χ	4π	Magnetic susceptibility
M_r	Am^{2}kg^{-1}	Remnant magnetization
H_c	T	Coercivity
$\vec{H}_{int}$	T	Internal magnetic field
$\vec{H}_{eff}$	T	Effective magnetic field

$\vec{H}_{app}$	T	Applied magnetic field
N		Demagnetization factor
A_s	°C	Austenitic start transformation temperature
A_f	°C	Austenitic finish transformation temperature
T_C	°C	Curie temperature
M_s	°C	Martensitic start transformation temperature
M_f	°C	Martensitic start transformation temperature
ΔG_c	J/mol	Chemical free energy from the structural change
ΔG_s	J/mol	Surface energy between parent and martensite,
ΔG_e	J/mol	Elastic or plastic strain energy
ΔG_{nc}	J/mol	Non-chemical free energy
σ_{mae}	Pa	Magneto stress
σ_{tbm}	Pa	Twinning stress
d_{gb}	m	Grain size
σy	Pa	Yield stress
σ_o	Pa	Single crystalline yield stress
P	%	Porosity
m_{foam}	g	Mass of the foam sample
V_{total}	cm^3	Total sample volume without pores
$\rho_{Ni\text{-}Mn\text{-}Ga}$	g/cm^3	Density of the alloy
q		Factor used for shape anisotropy correction
n		Integer multiple

λ	nm	Wavelength,
d	nm	Lattice spacing of crystallographic planes
2θ	°	Diffraction angle
v_{free}		Unconstrained volume fraction
w	μm	Strut width
l	μm	Strut length and
α	°	Angle between the twin boundary and node
MFIS	%	Magnetic field induced strain
x	mm	Short sample length
y	mm	Intermediate sample length
z	mm	Long sample length
a	Å	Lattice parameter
b	Å	Lattice parameter
c	Å	Lattice parameter
β	°	Angle between a and c axis

TABLE OF CONSTANTS

Symbol	Description	Quantity
e	electron charge	1.602×10^{-19} C

1   INTRODUCTION

Fifty years ago materials science focused on strength and mechanical properties. Present day material science has evolved the focus unto functional materials and materials for devices. Unique materials properties such as magnetic, thermal, and electrical have been utilized for applications that have revolutionized the world. In 1903 a German miner /chemist Heusler discovered that if he alloyed three non metallic metals (Cu, Al, and Mn) the resulting alloy would be found to be magnetic. These types of alloys would later be called Heusler alloys, named after the discoverer [1]. In the late 1960's at a naval ordinance lab, 12 intermetallic alloys, including Nickel Titanium (NiTi), were selected for work on missile reentry nose cones [2]. During testing it was discovered that NiTi had unusual properties such as temperature dependent sound dampening and significant length changes after annealing [2]. At a Naval Ordinance Lab (NOL) management meeting, Dr. William J. Buehler brought a thin sheet of the unusual metal to the meeting and bent it in multiple places in an accordion shape. Associate Director of NOL, Dr. David Muzzey , then heated the sample with his tobacco pipe and found the metal returned to its original shape "with considerable force" [2]. The shape memory alloy NiTi was discovered out of pure curiosity and some say accidentally.

Shape memory alloys (SMA) are a class of functional materials that can change their shapes and dimensions under the application of external fields [3-5]. The external fields used may be the thermal, electric or magnetic. Thermal activated SMA, such as NiTi, may exhibit plastic deformation up to 6% which is recovered by heating the deformed martensite through the martensitic/austenitic transformation temperature [6]. Magnetic Shape Memory Alloys (MSMA) are activated by a magnetic field, in the martensitic state, in which strains can be recovered by rotation of the magnetic field [7-11]. Therefore, MSMAs do not have to proceed through a phase transformation to recover the original shape. MSMA include antiferromagnetic materials, such as $Ni_{45}Co_5Mn_{36.7}In_{13}$. and Mn–Fe–Cu which can show strains of 3% and 1.6% at magnetic fields of 8 and 3.8 T respectively [12, 13]. Ferromagnetic MSMA, include Fe–Pd, Fe–Pt and Ni–Mn–Ga. FePd demonstrates strains up to 0.5% [11, 14, 15]. In 1996, Ullakko et al. found a 0.2% magnetic field induced strain (MFIS) in a Ni-Mn-Ga single crystal [11]. The MFIS of Ni–Mn–Ga single crystal increased up to 6% in 2000 [16] and to 9.5% in 2002 by slightly varying the composition and martensite variant selection (otherwise called training) [7, 10, 17, 18]. Therefore off stoichiometric Ni-Mn-Ga has been one of the most promising MSMA and has been widely studied.

2   MOTIVATION

Ni-Mn-Ga has high potential for uses as an actuators, sensors, and power generation because of the magnetic shape memory properties [18-23]. One advantage of MSMA over thermally activated SMA is that the actuation frequency can be 1000 times faster, depending on size, due to the low thermal conductivity of SMA [24]. Piezoelectric materials can deform at frequencies up to 10^7 Hz but at much lower strains than MSMAs. Magnetostrictive materials such as Terfenol-D ($Tb_{0.27}Dy_{0.73}Fe_2$) can deform with the same frequency as MSMA s but only to 0.1% strain [25].

Giant MFIS, at room temperature, has only been shown in single crystals of Ni-Mn-Ga. Single crystal growth is time consuming with high production costs. Crystal growth also leads to chemical segregation throughout the crystal rod [26, 27]. Consequently there are many hindrances in studying and producing single crystals with reproducible properties. Polycrystalline materials show chemical homogeneity and have much lower production costs. Polycrystalline Ni-Mn-Ga alloys are not widely studied due to the small amounts of Magnetic Field Induced Strain (MFIS) [28-30]. It is assumed that the low MFIS is due to geometric constraints of the grain boundary on twin boundary motion. To reduce the hindrance on twin boundary motion in polycrystals often highly

textured, large grained specimens with extensive mechanical training or thin films are studied [28, 31-38].

Recently is has been proposed that porosity may also be an additional means of increasing MFIS [39]. Pores take up grain boundaries and effectively reduce the degree of internal constraint within the polycrystal. The first Ni-Mn-Ga foams, with a monomodal pore size distribution, demonstrated MFIS larger than reported values for other polycrystalline Ni-Mn-Ga giving credence to the assumption [39]. Therefore porosity may lead to enhancement of MFIS.

3   BACKGROUND

3.1   Magnetism

The magnetic moment can be thought of classically with a current loop model given by 1, where I is current and A is area[40, 41].

$$\vec{\mu} = I \cdot A \tag{1}$$

A magnetic moment $\vec{\mu}$ can also be attributed to an electron orbiting a nucleus given below [40, 41].

$$\vec{\mu} = -\frac{e}{2m}\vec{L} \tag{2}$$

Where m is the mass of the electron, e is the charge and $\vec{L}$ is the angular momentum. The magnetic moment can also be written in terms of the spin $\vec{S}$ as shown in 3[40, 41].

$$\vec{\mu} = -\frac{e}{m}\vec{S} \tag{3}$$

In a solid, the magnetic moments of atoms are summed up to give the macroscopic magnetic moment per unit volume, otherwise known as magnetization $\bar{M}$.

A magnetic field can be described by the magnetic field induction $\vec{B}$ and the magnetic field intensity $\vec{H}$ which are related through the permeability of free space [40, 41].

$$\vec{B} = \mu_0 \vec{H} \tag{4}$$

In a material, $\vec{B}$ and $\vec{H}$ are related through 5. The magnetization and magnetic field intensity in a material are related through the magnetic susceptibility (χ) given in 6.[41]

$$\vec{B} = \mu_0 (\vec{H} + \vec{M}) \tag{5}$$

$$\vec{M} = \chi \vec{H} \tag{6}$$

Magnetic susceptibility can either be positive for paramagnetic materials or negative for diamagnetic materials.

3.1.1 Diamagnetism

In diamagnetic materials no magnetic dipoles exist without a magnetic field. In a diamagnetic material when a field is applied a dipole is created through the induction phenomenon described by 1. The induced dipole orients opposite to the applied field due to Lenz law (Figure 3.1). Diamagnetic materials typically have no unpaired electrons.
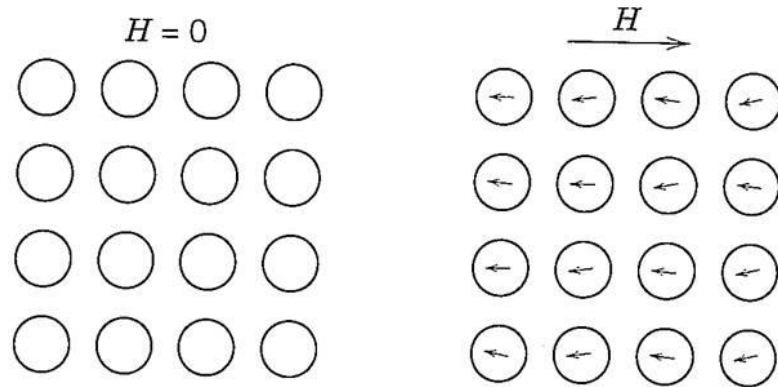
Figure 3.1 Atomic Dipoles Without (Left) and With (Right) a Magnetic Field Applied to a Diamagnetic Material. Reprinted with Kind Permission From [42].

3.1.2   Paramagnetism

In a paramagnetic material there exist magnetic dipoles without the presence of a magnetic field. Due to thermal energy the dipoles are randomly oriented. When a field is applied the dipoles will align parallel to the field and exhibit a net magnetization (Figure 3.2). Typically, materials that exhibit paramagnetic properties are those with unpaired electrons.
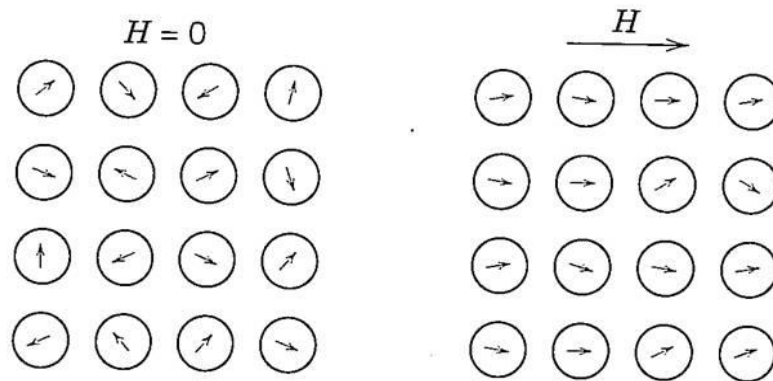
Figure 3.2 Atomic Dipoles of a Paramagnetic Material Without an Applied Field (Left) And With An Applied Field (Right). Reprinted With Kind Permission From [42].

3.1.2.1 Ferromagnetism

Neighboring magnetic moments can couple parallel to each other and be considered ferromagnetic or couple anit parallel and be considered antiferromagnetic illustrated in Figure 3.3. Ferromagnetic materials can exhibit spontaneous magnetization without an applied field.
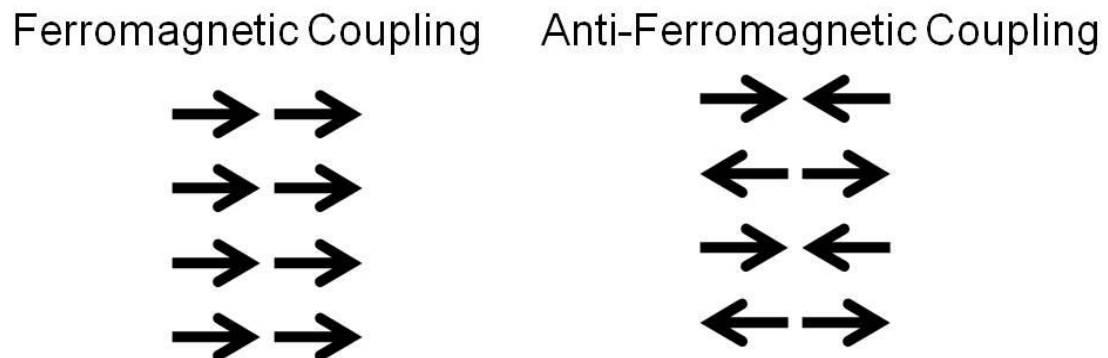
Figure 3.3 Magnetic Coupling can be Ferromagnetic and Align Parallel to Each Other or Antiferromagnetic And Align in Opposite Direction to Each Other.

Magnetic domains are groups of magnetic dipoles; they form such that areas of the material show different orientations of the magnetic moments. Figure 3.4 shows the change in magnetic domains of a ferromagnetic material with increasing field. At first the magnetic domains are oriented such that there is no net magnetization. As the magnetic field increases the domains that are oriented with the applied field, grow and the other domains shrink. As the domains grow the magnetization increases. At some magnetic field only one domain remains that is slightly rotated from the direction of the applied magnetic field. With an increase in magnetic field the domain rotates parallel to the direction of the magnetic field and results in magnetization saturation. The point at which the field increase no longer changes the net magnetization is called magnetization saturation.
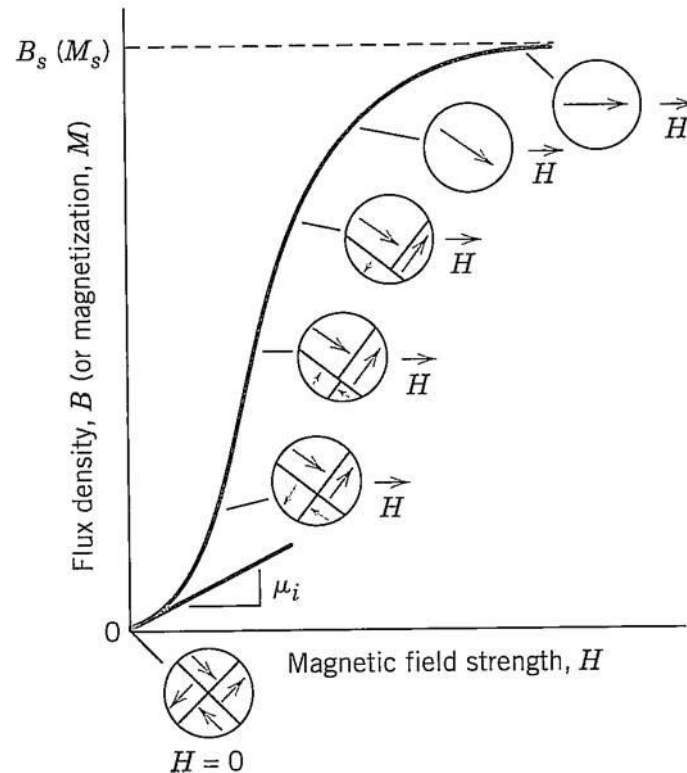
Figure 3.4 The Change in Magnetization with Increasing Field Strength is Shown Along with the Change in Magnetic Domain Structure. Domain Barriers are Marked with Solid Lines and the Direction of Net Magnetization are Marked with the Arrow. The Dotted Line is the Magnetization Saturation Point Where All Magnetic Domains are Fully Aligned with the Field. Reprinted with Kind Permission from [42].

If the field is decreased back to zero the magnetization will not fallow the same path and there will be some remnant magnetization M_r (Figure 3.5). In fact to return the magnetization back to zero the field must be reversed. The negative field that is required to give a magnetization of zero is called the coercivity H_c (Figure 3.5). A magnetic hysteresis exists because energy has to be dissipated for domain wall motion.
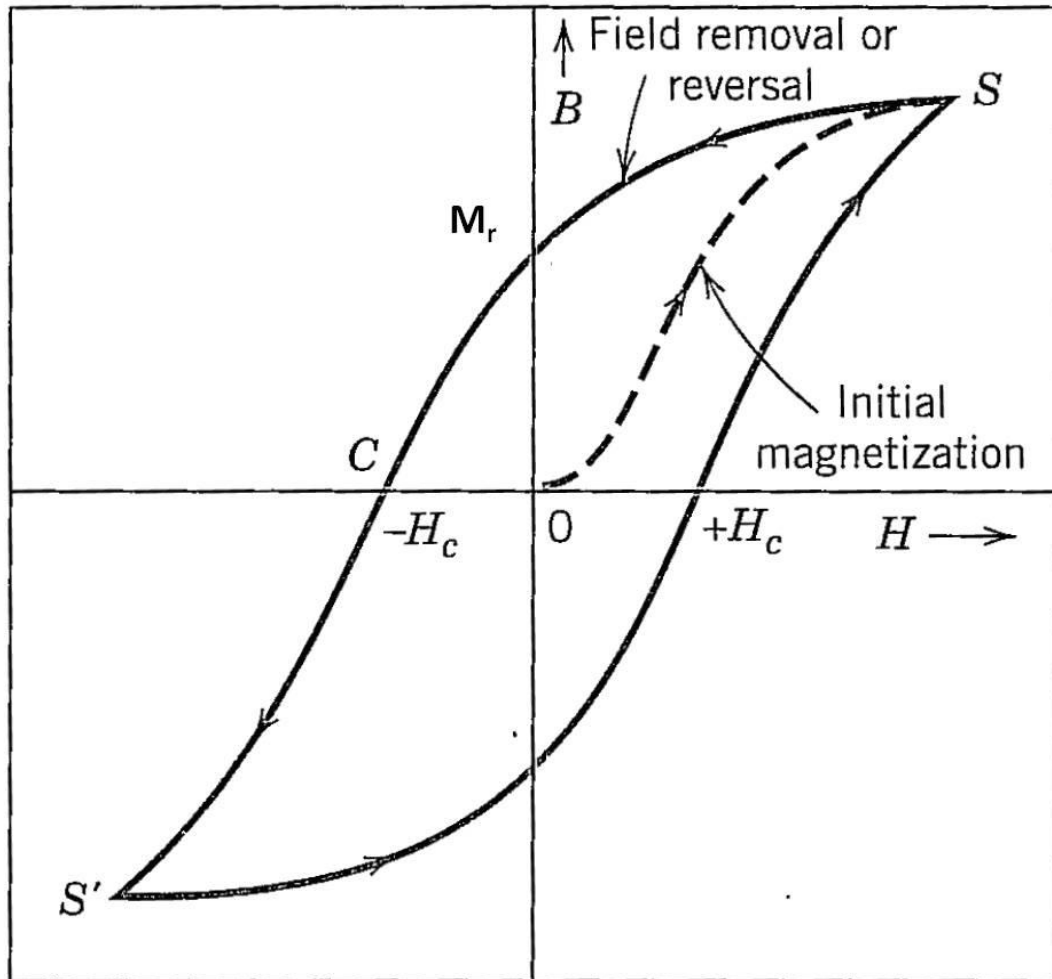
Figure 3.5 Hysteresis Loop of a Ferromagnetic Material Showing Remnant Magnetization M_r and Coercivity H_c. Starting at the Origin to Initial Magnetization (Dashed Line)Up to Saturation (S). The Magnetic Field is Then Decreased to Zero Where Some Remnant Magnetizations M_r is Observed. A Negative Magnetic Field is Applied Past the Point of Zero Magnetization (H_c) Until the Domains are Fully Saturated in the Opposite Direction as the Original Saturation Magnetization. The Magnetic Field is Once Again Driven to Zero and Then Increased Until Domains are Once Again Saturated. Reprinted with Kind Permission from [42]

3.1.2.2 <u>Magnetic Ordering in Heulser Alloys</u>

In Heusler alloys the ordering of the $L2_1$ lattice is crucial for formation of the magnetic moments. In Ni_2MnGa, manganese atoms carry most of the magnetic moment in the unit cell. Normally in elemental manganese magnetic dipoles couple antiferromagnetic between neighboring atoms. However, in the $L2_1$ structure the manganese atoms couple through the adjacent atomic orbital, to give rise to ferromagnetic ordering. The magnetic coupling is driven by the spacing of the manganese atoms. Therefore MSMs magnetic properties are extremely compositionally sensitive. In off stoichiometric Ni-Mn-Ga excess Nickel, Manganese, or Gallium fill positions not specified by the $L2_1$ structure and may lead to localized antiferromagnetic coupling.

3.1.2.3 <u>Magnetic Transitions</u>

Thermal fluctuation disrupt any magnetic order and therefore cause second order magnetic transitions. In a ferromagnetic material the temperature at which a sample loses magnetization is called the Curie temperature or T_c seen in Figure 3.6. Similarly in antiferromagnetic materials the temperature at which the antiferromagnetic ordering is lost is called the Ne`el Temperature.
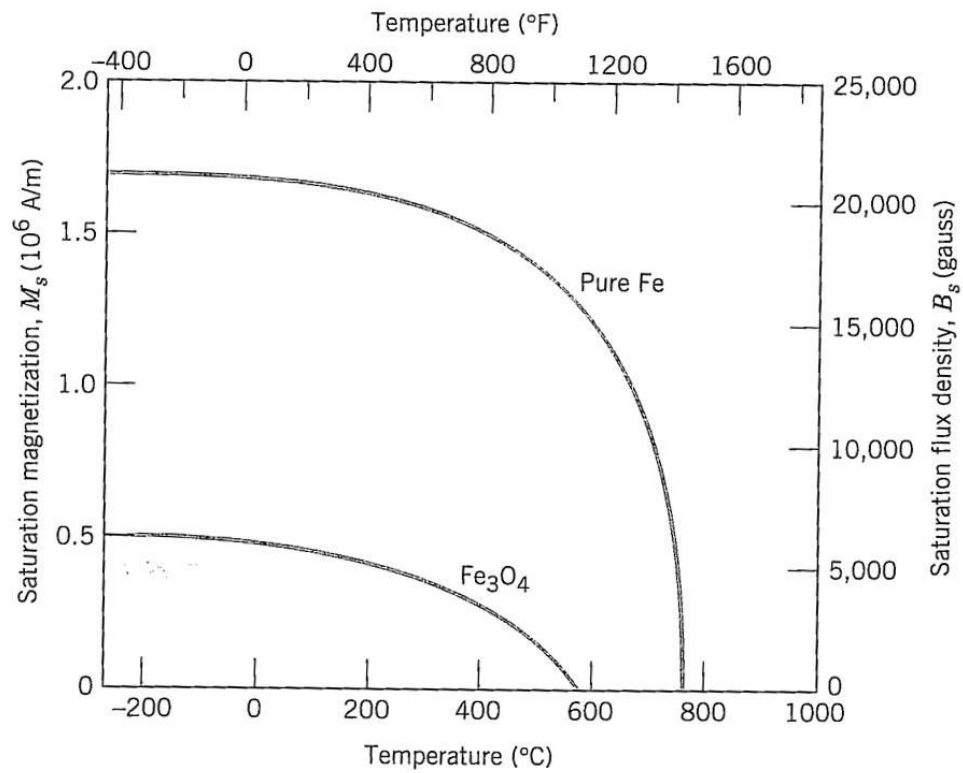
Figure 3.6 Curie Transformation of Iron and Ferrite. The Saturation Magnetization Decreases with Increasing Temperature until All Magnetization is Lost. The Temperature at Which Magnetization Reaches Zero or T_c, is 750 °C and 560 °C for Iron and Ferrite Respectively. Reprinted with Kind Permission from [42]

3.1.3   Anisotropy

      Anisotropy occurs in a material when material properties have a directional

dependence. Magneto crystalline anisotropy occurs when the magnetic properties depend

on the crystallographic direction. With magneto crystalline anisotropy there will be an

"easy" and "hard' direction of magnetization, that correlates to some crystallographic

direction. The easy direction of magnetization is such that a lower magnetic field is

needed to reach magnetization saturation (marked by a dashed line in Figure 3.7). The

hard direction of magnetization is the crystallographic direction that requires a higher

magnetic field, to reach magnetization saturation. Figure 3.7 shows a plot of

magnetization versus field, in two different crystallographic orientations, of a single

crystal of magnetite. Both curves reach the same saturation magnetization, but the slopes

of the *M-H* curve before saturation are very different. The steeper *M- H* curve correlates

to applying a magnetic field parallel to the easy axis of magnetization, and the shallow

slope corresponds to applying the magnetic field parallel to the hard axis of

magnetization. Therefore the magnetization at any field below saturation will be higher

for the easy axis of magnetization.
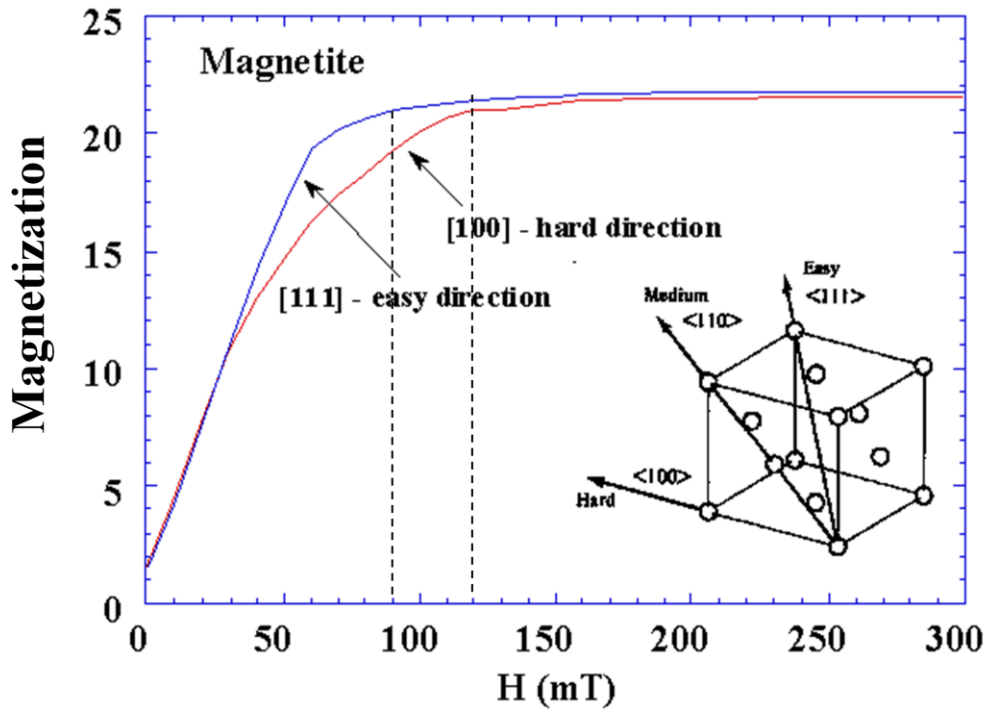
Figure 3.7 Magneto Crystalline Anisotropy for Magnetite. The Easy Direction (blue) of Magnetization Requires Less Field to Reach Saturation than the Hard Direction (red) of Magnetization (Marked by Dotted Line). The Easy and Hard Directions of Magnetization Correlate to Crystallographic Orientation Shown in the Unit Cell. Reprinted with Kind Permission from [43]

The area between the curves corresponds to the magneto crystalline anisotropy energy. In polycrystals magneto crystalline anisotropy arises from a preferred orientation of the easy and hard axis of magnetization (i.e. from crystallographic texture).

When a magnetic field is an applied to a material magnetization will occur. The magnetization in the media creates an internal magnetic field ($\vec{H}_{int}$) opposing the applied field which is leads to internal demagnetization. The internal demagnetization therefore reduces the applied magnetic field. The internal demagnetization depends on the shape.

Consequently shape anisotropy will exist for any non spherical shape. The effective field intensity $\vec{H}_{eff}$ is the applied field intensity $\vec{H}_{app}$ diminished by the internal magnetic field which is proportional to a size dependent demagnetization factor (N) and magnetization $\vec{M}$ [40, 41].

$$\vec{H}_{eff} = \vec{H}_{app} - \vec{H}_{int} = \vec{H}_{app} - N_{demag}\vec{M} \tag{7}$$

A detailed explanation of determining demagnetization factors for the parallelepiped samples of this study are given is section 4.2.1. The magneto crystalline anisotropy of Ni-Mn-Ga is discussed more in section 3.3.

3.2   Crystal Structures

The high temperature austenite phase of Ni_2MnGa has face centered cubic lattice with the atomic positions and space group shown in Table 3.1.

Table 3.1 Crystal Structure Information for the $L2_1$ Ordered Austenite Phase of Ni_2MnGa.

Space Group	Lattice Parameter	Atomic Positions				Illustration
Fm-3m	a= 5.81Å	Ga	0	0	0	
		Mn	0	0	0.5	
		Ni	0.25	0.25	0.25	
		Ni	0.25	0.25	0.75	

The low temperature martensite phase can adopt either modulated or non modulated structures. The most commonly reported structures are 14M, 10M (M meaning modulated) or non-modulated NM, for which crystal information can be found in Table A.1 in the appendix.

14M and 10M are modulated structures which are also referred to as 7M and 5M respectively. 14M and 10M structures are described with $(\bar{5}, 2)_2$ and $(\bar{3}, 2)_2$ stacking sequences using Zandov notation which is illustrated in Figure 3.8 [8, 44-46]. The modulated cell can be chosen from multiple reference frames but here a body centered monoclinic cell was chosen to fully reflect the lattice symmetry (Figure 3.8). The long period stacking occurs by displacement of $(001)_m$ (m is referring monoclinic martensite reference frame) in the $[100]_m$ direction[8]. The b axis of the austenite becomes the b axis of the modulated structures and the $(10\bar{1})$ of the cubic cell becomes the (001) plane in the Martensite cell.[8]
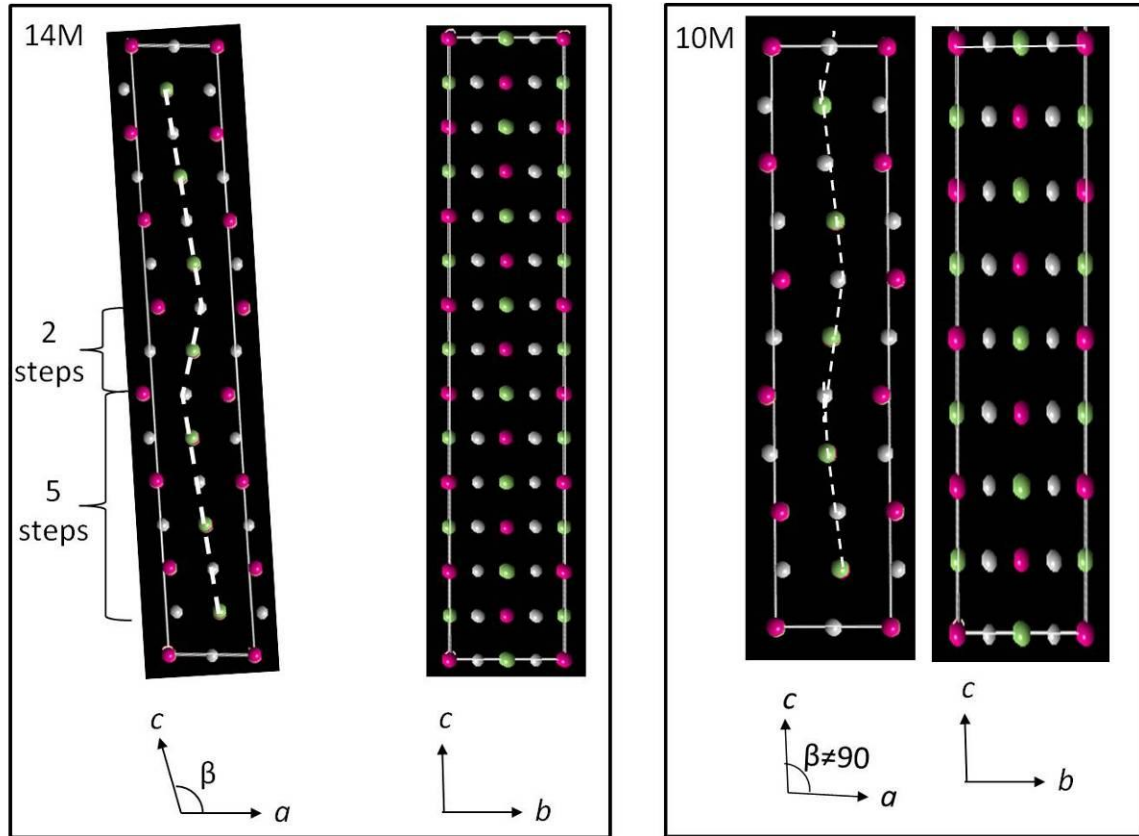
Figure 3.8 Crystal Structures of the Modulated Martensite Lattice. 14M (Left) Shows an Ordered Displacement, Traced by the Dotted Line, in the [100] Along the Long Period [001] Direction, and No Modulation Along the *b* Direction. The Ordered Displacement is Between (001) Type "Basal" Planes and is Described by 5 Steps in One Direction Followed by 2 Step in the Opposite Direction Repeated Twice. 10M (right) has Less Modulation as Described by the ($\bar{3}$,2)₂ Stacking Sequence (Traced with Dotted Line). Gray Circles Represent Nickel, Pink Represents Manganese and Green Represents Gallium.

The modulated structures can also be viewed from the reference frame of the austenite or parent lattice. If viewed from the austenite reference frame tetragonal and orthorhombic cells for 10M and 14M are reported. However if the austenite reference frame is drawn into the modulated lattice, it can be seen that the resulting cell cannot be

described with tetragonal or orthorhombic lattices since no angles are 90° and the shape

of the "exact" cell vary from layer to layer (Figure 3.9) . The tetragonal and orthorhombic

cells are therefore approximations of the modulated lattice and are thus pseudo-cells. If

the pseudo-cell is draw throughout the entire modulated unit cell the average of all angles

and lattice parameters result in lattice parameters which match experimentally determined

lattice parameters of tetragonal and orthorhombic cells [26]. The non modulated lattice

can be accurately described by a tetragonal cell and is described in Table 10.1 in the

appendix. Orthorhombic and tetragonal pseudo cells are convenient to describe the

magneto mechanical behavior and therefore will be used here.
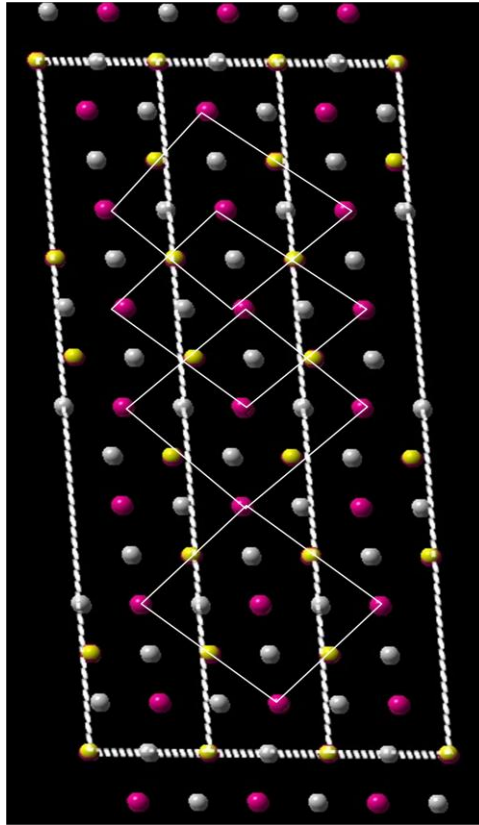
Figure 3.9 14M Lattice Viewed from the Austenite Reference Frame. The White Boxes are the Distorted Martensite Cells as Would be Viewed from the Austenite Reference Frame. The Cell are Traced up Through the Modulated Lattice do not Result in any 90° Angles and Therefore Cannot be Described with an Orthonormal Bravais Lattice.

Composition is one main factor affecting crystal structure. Richard et al. in 2006 characterized the crystal structure of powdered single crystals with varying compositions and found multiple combinations of structures shown in Figure 3.10 [26]. Furthermore, residual stress can change the crystal structure. [34, 47].
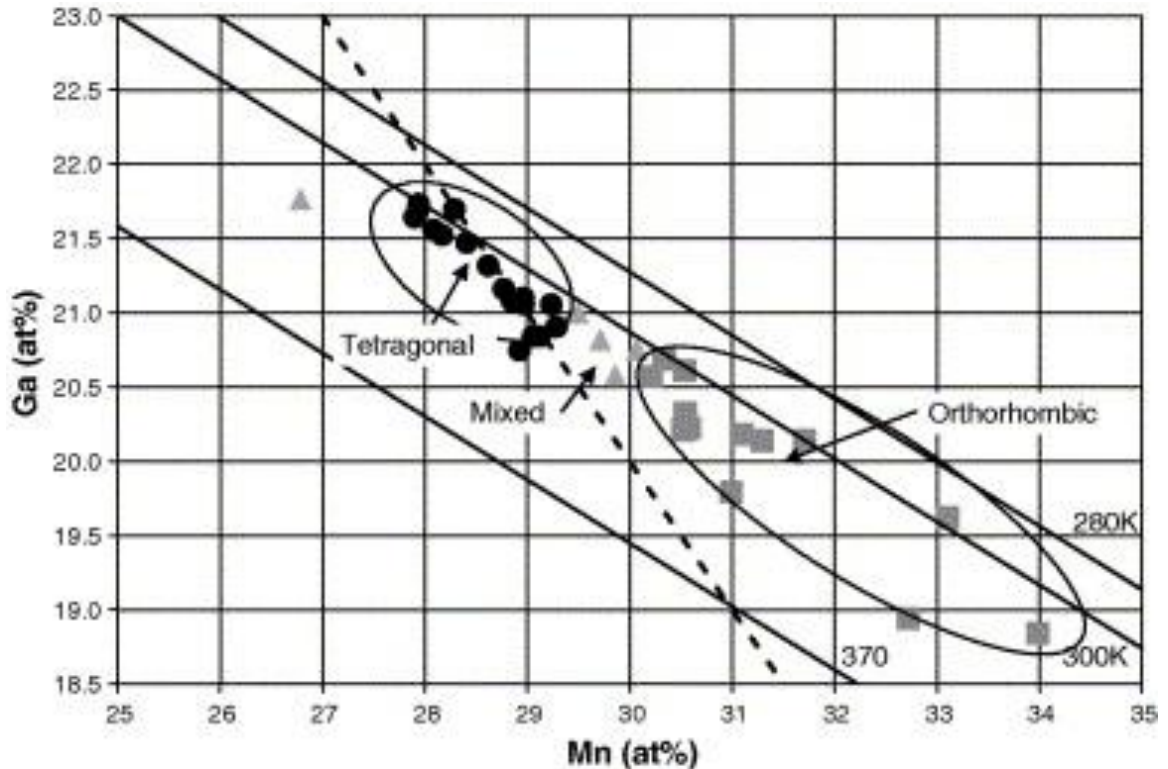
Figure 3.10 Composition Effects on Crystal Structure After Annealing. Orthorhombic is Plotted with Squares, Tetragonal with Circles, and Mixtures with Triangles. The Solid Sloped Lines are Different Temperatures. Reprinted with Kind Permission from [26].

3.3 Anisotropy of Ni-Mn-Ga

In the austenite phase the material has little magnetic anisotropy with saturation occurring at 0.04-0.05 T depending on composition [21, 48]. In the martensite phase the magneto crystalline anisotropy energy can range from 50-250 kJ/m^3 depending on the crystal structure[49, 50]. In the 10M, 14M, and NM tetragonal martensite the short lattice parameter of the pseudo unit cell is the easy axis (or plane) of magnetization (Figure 3.11) [50]. For the 10M crystal structure (Figure 3.11a) there is an easy direction of

magnetization parallel to the [001] direction (dashed line) and a hard plane of

magnetization in the (001) plane. In the NM martensite (Figure 3.11b) there is a easy

plane of magnetization (001) and a hard direction of magnetization parallel to the [001]

direction (black circles).The orthorhombic cell for the 14M martensite (Figure 3.11c)

shows three axis of magnetization: an easy axis parallel to [001] direction, an

intermediate axis (dotted line) parallel to [010], and a hard axis parallel to [100] [50].

Therefore for all four crystal structures discussed, at a low field the easiest direction of

magnetization will have the highest magnetization.
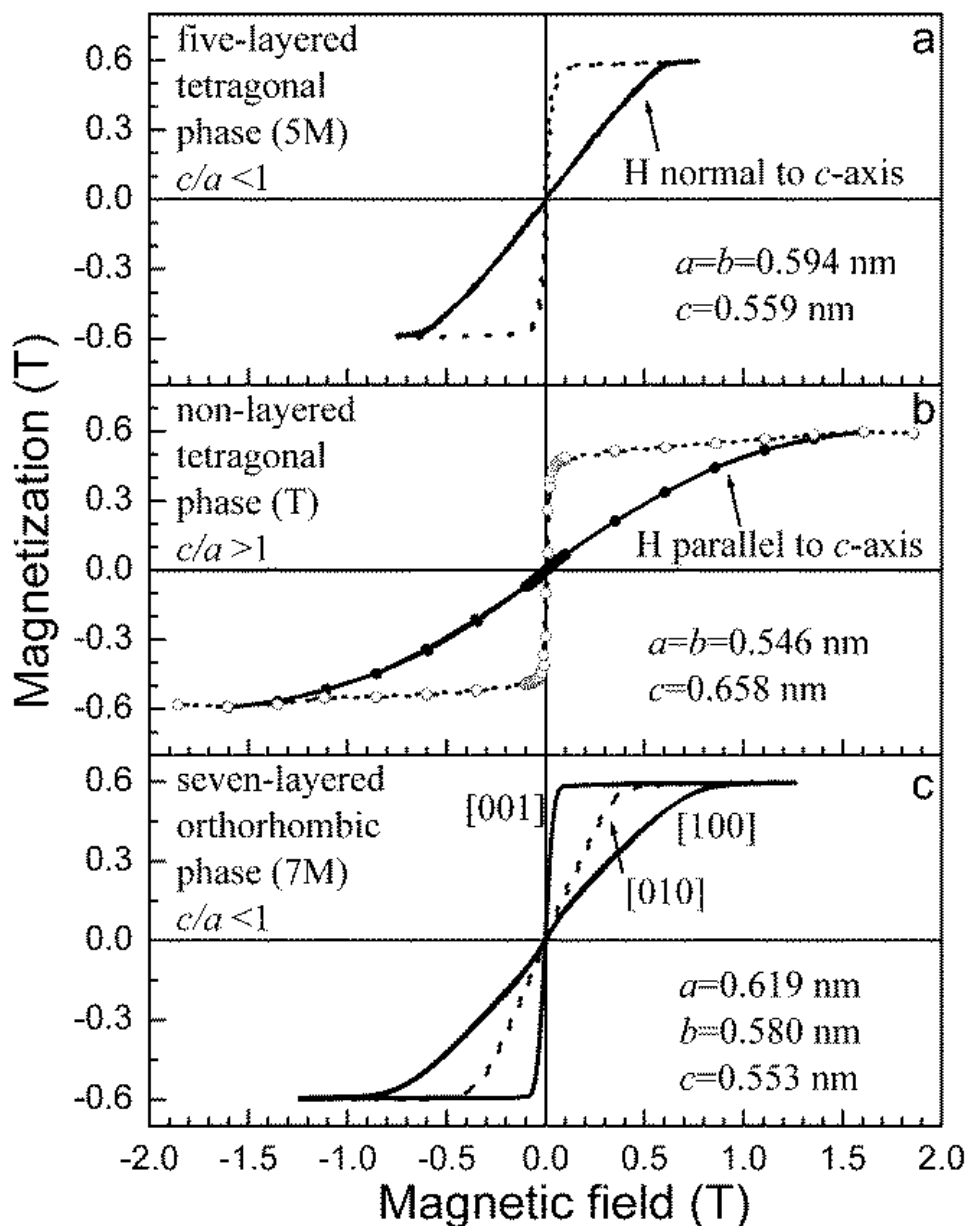
Figure 3.11 Magnetic Hysteresis Curves for Three Crystal Structures of Ni$_2$MnGa. For the 10M (a) there is an Easy Direction of Magnetization Parallel to the [001] Direction (Dashed Line) and a Hard Plane of Magnetization in the (001) Plane. In the NM Martensite (b) there is a Easy Plane of Magnetization (001) and a Hard Direction of Magnetization Parallel to the [001] Direction (Black Circles).The 14M Martensite (c) Shows Three Axis of Magnetization an Easy Axis Parallel to [001] Direction, a Medium Axis (Dotted Line) Parallel to [010], and a Hard Axis Parallel to [100] Lattice Parameters are Given for each Crystal Structure. Reprinted with Kind Permission from [50]. Copyright [2002] IEEE.

3.4 Martensite Phase Transformation

Martensite phase transformations are diffusionless displacive transformations[51]. In MSMA a high temperature phase (cubic for Ni-Mn-Ga) goes through a Bain distortion where two or three axes are distorted such that the symmetry is reduced[8, 52]. The distortion is followed by a lattice invariant shear in which twins are formed to minimize strain energy from the phase transformation[6]. Twins are defined as two crystals related through a mirror operation. Figure 3.12 shows a view of the austenite and martensite lattice, with a simplified interface relationship. Dislocations form at the twin interface and facilitate the motion of the twin boundaries. Thus, twinning dislocations are responsible for the MFIS seen in MSMA's, which will be discussed in section 3.5.1.
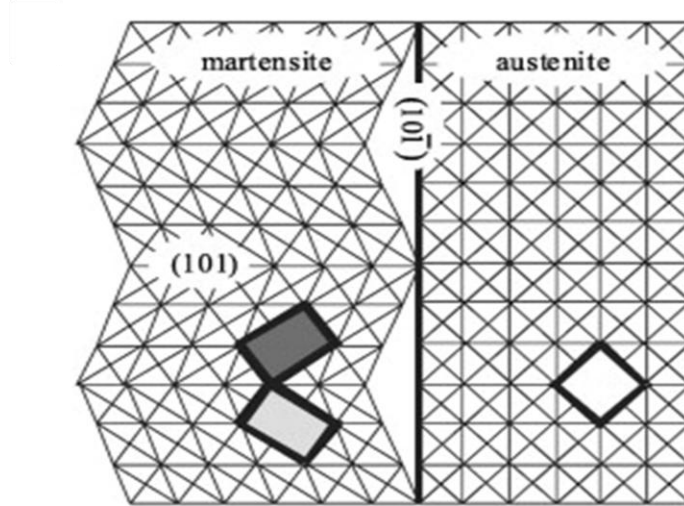
Figure 3.12 Change in Structure Upon the Martensite Phase Transformation. The Cubic Austenite is the Lattice on the Right Where the Cubic Cell is Marked. Upon the Martensite Phase Transformation (Left Lattice) the Lattice Goes Through a Tetragonal or Orthorhombic Distortion, Marked by the Gray Tetragonal Cells, Followed by Lattice Invariant Shear that Result in Twin Formation. The Mirror Symmetry by Twin Formation is Shown by the Mirror Relation of the Two Tetragonal Cells. Reprinted with Kind Permission from[53].

Once in the martensite phase it is possible for intermartensitic transformations to occur. Severe cooling or force can initiate the intermartensitic transformation. Intermartensitic transformations have been observed to occur such that a 14M structure transforms to a 10M and the 10M follows to NM structure [54-57].

3.4.1   Thermodynamics of Martensite Transformations

The strain energy caused by the nucleation and growth of the martensite phases causes a martensite phase transformation hysteresis with many measureable quantities

such as magnetization and strain (Figure 3.13). Upon heating the austenite starts to form

A_s resulting in an increase of magnetization. As the volume of austenite is increased the

magnetization is increased until the transformation is finished at A_f. Magnetization is lost

upon further heating at the Curie temperature T_c. Cooling restores the magnetization and

initiates the martensite phase transformation M_s. The magnetization is reduced as the

volume fraction of martensite is increased until the materials is fully martensite M_f.
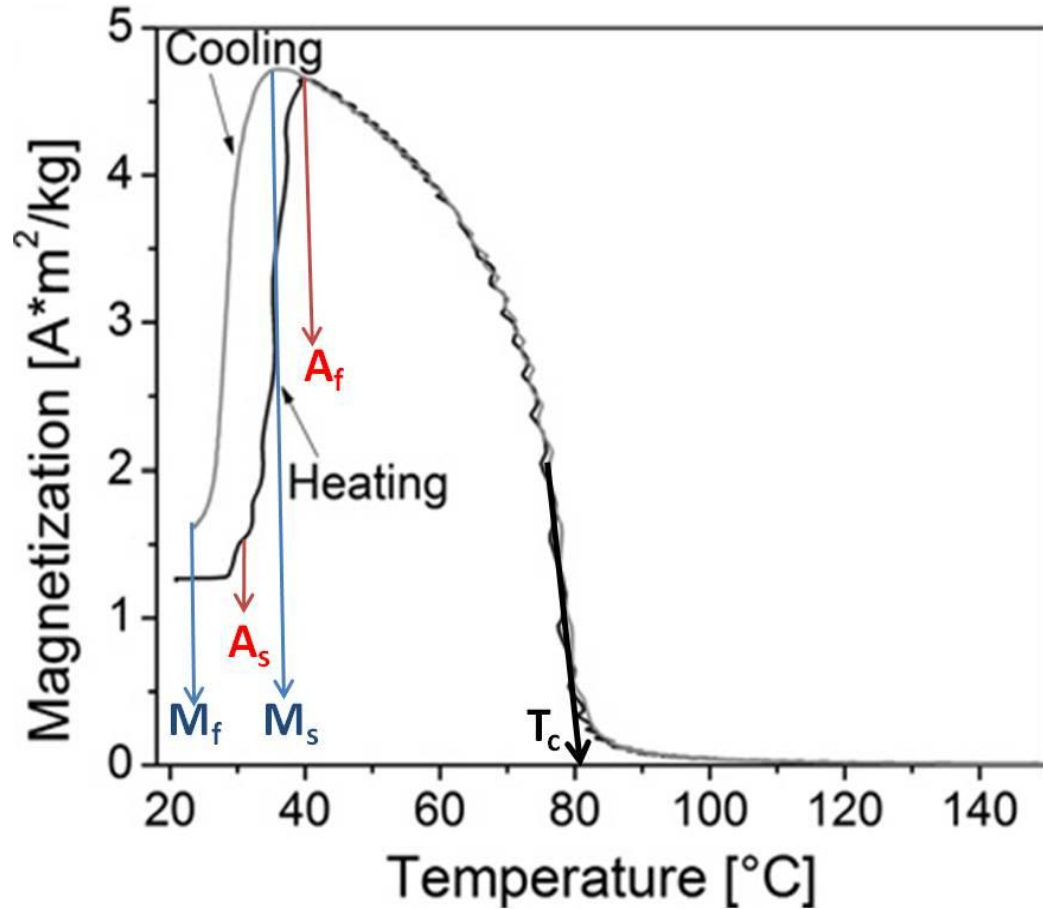
Figure 3.13 Phase and Magnetic Transformation for A Ni-Mn-Ga Polycrystal. Upon Heating the Austenite Starts to Form A_s Resulting in an Increase of Magnetization as the Volume of Austenite Increases until the Transformation is Finished A_f, Marked with Red Lines. Magnetization is Lost Upon Further Heating at the Curie Temperature T_c. Cooling Restores the Magnetization and Initiates the Martensite Phase Transformation M_s. The Magnetization is Reduced as the Volume Fraction of Martensite Increases Until the Materials is Fully Martensite M_f, Marked With Blue Lines.

The additional strain and surface energies due to martensite formation must be accounted for within any thermodynamic energy expression [6, 51, 58-61]. To proceed with a favorable transformation the specimen must be under cooled or over heated to a critical temperature at which the strain energy is overcome by the change in temperature

[6, 51, 58-61]. Additionally the formation of the second phase will add strain energy requiring more work to be put into the system for the phase transformation to proceed.[6, 51, 59] Therefore, the transformation will happen over a range in temperature such that $A_s \neq A_f$ and $M_s \neq M_f$ which is seen in Figure 3.13 [6, 26, 51, 59]. Finally the total Gibbs free energy of martensite formation is a function of the chemical free energy and the non-chemical free energy.[6] Where ΔG_c is the chemical energy from the structural change, ΔG_s is the surface energy between parent and martensite, ΔG_e is the elastic or plastic strain energy term around the martensite.

$$\Delta G^{p-m} = \Delta G_c + \Delta G_s + \Delta G_e \qquad (9)$$

Simplifying further the Gibbs free energy of transformation becomes,

$$\Delta G^{p-m} = \Delta G_c + \Delta G_{nc} \qquad (10)$$

Where ΔG_{nc} is non-chemical energy term and is the sum of the surface and elastic strain energy terms.

The non-chemical free energy can be different based on the type of transformation. There are thermoelastic and non thermoelastic transformations [6, 51, 58, 59]. Thermoelastic martensite transformation occurs when the austenite- martensite interface boundary is mobile and there is total elastic variant reversion [6, 58, 60, 61]. Elastic variant reversion means the orientation of the parent phase is remembered and recaptured during phase cycling [61]. Thermoelastic transformations are necessary for a working MSMA or SMA and often result in a small non chemical free energy term. Non-thermoelastic transformations do not have a mobile interface and upon variant reversion

the orientation is not remembered [6, 61]. Non-thermoelastic transformation results in an elastic and plastic strain, causing a larger non chemical free energy term. A non-thermal transformation is typical of martensite formation in steel [6, 61].

3.5 Magneto Mechanical Properties

3.5.1 Twin Boundary Motion

The magnetic shape memory effect is achieved by twin boundary motion, mediated through the motion of dislocation [8, 19, 53]. Twin boundaries will move in response to an applied force, such as stress or magnetic field illustrated in Figure 3.14 [7-9, 11, 17, 19, 53, 62, 63]. The anisotropy of the material is the driving force for twin boundary motion. The motion will proceed, such that twin variants that have the c axis aligned with the applied force will grow, at the expense of the surrounding variants [7-9, 11, 17, 19, 53, 62, 63]. The twin variant growth provides the overall shape change as shown in Figure 3.14. The theoretical strain of a single crystal can therefore be calculated by martensite lattice parameters. The theoretical strains for NM is 21% , 10M is 6%, and 14M is 10% [7, 11, 17, 62-64]. For twin boundaries to move in a rotating magnetic field the magneto stress on the twin dislocation σ_{mae} must be greater than the twinning stress σ_{tbm}.
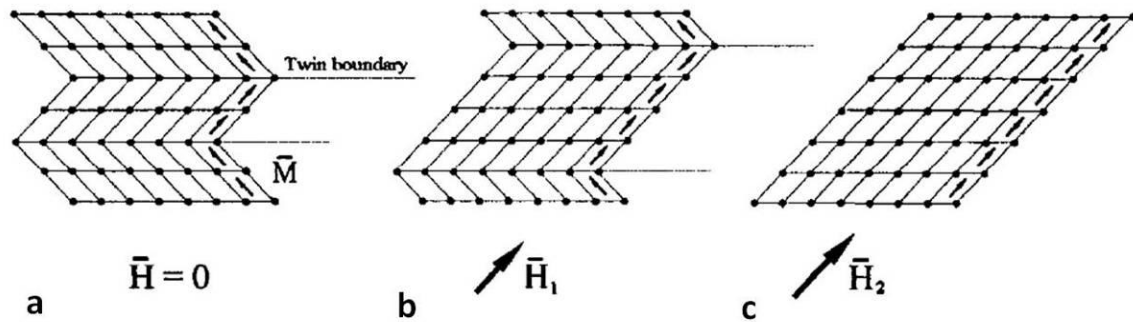
Figure 3.14 Twin Boundary Motion Due to an Applied Magnetic Field. The Easy Axis of Magnetization is Marked with an Arrow Inside the Cell. A) In the Initial State There are Two Distributions of the Easy Axis and Therefore Two Martensite Variants. B) In the Intermediate State A "Week" Magnetic Field is Applied Which is Enough to Move the Twin Boundaries. The Boundaries Move Such that the Variant with the Easy Axis of Magnetization Aligned with the Field Grows and the Second Variant Shrinks. C) Lastly with a Stronger Magnetic Field with Twin Boundaries Can Move Completely Through the Lattice Resulting in a Single Variant State. Reprinted with Kind Permission from[65].

3.5.2   Twinning Incompatibilities

Twin microstructure has a large impact on the magneto-mechanical properties as well as the fatigue life [8]. It is seen that self accommodated martensites (many twin variants) show very small strains as compared to the single variant or trained state, which is illustrated in Figure 3.15[8, 17]. Single variant microstructures show high strain but short fatigue lives. Fine twins show smaller strains but longer fatigue life [8, 66].
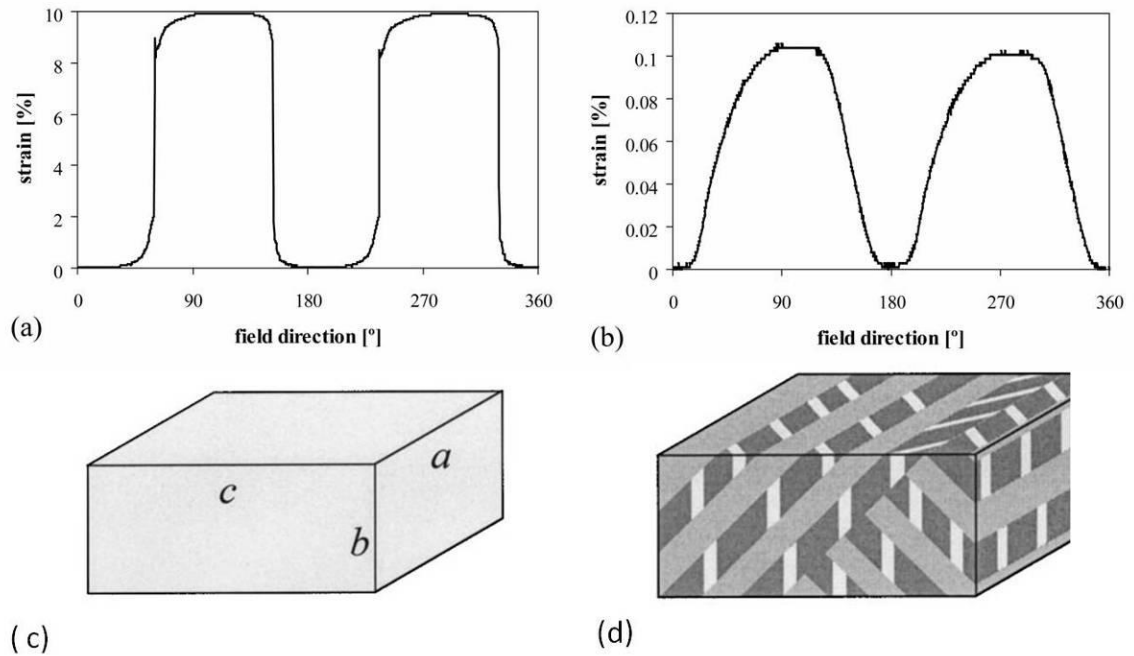
Figure 3.15 Changes in Magneto-Mechanical Behavior with Microstructure of Single Crystals. A Thermo-Mechanically Trained Sample with a 14M Structure Shows the Theoretical Maximum in Strain (A) With a Narrow Range of Field Angles that Resulted in Strain. The Strain Caused By a Magnetic Field is Small in a Self Accommodated State (B) and Occurs Over a Wide Range in Angles. Trained and Self Accommodated Microstructure Might Exist Which are Shown in (C,D). Adapted and Reprinted with Kind Permission from [8, 17]

Upon studying the fatigue life in single crystals, by mechanical cycling, voids and cracks were formed along the twin boundaries shown in Figure 3.16.
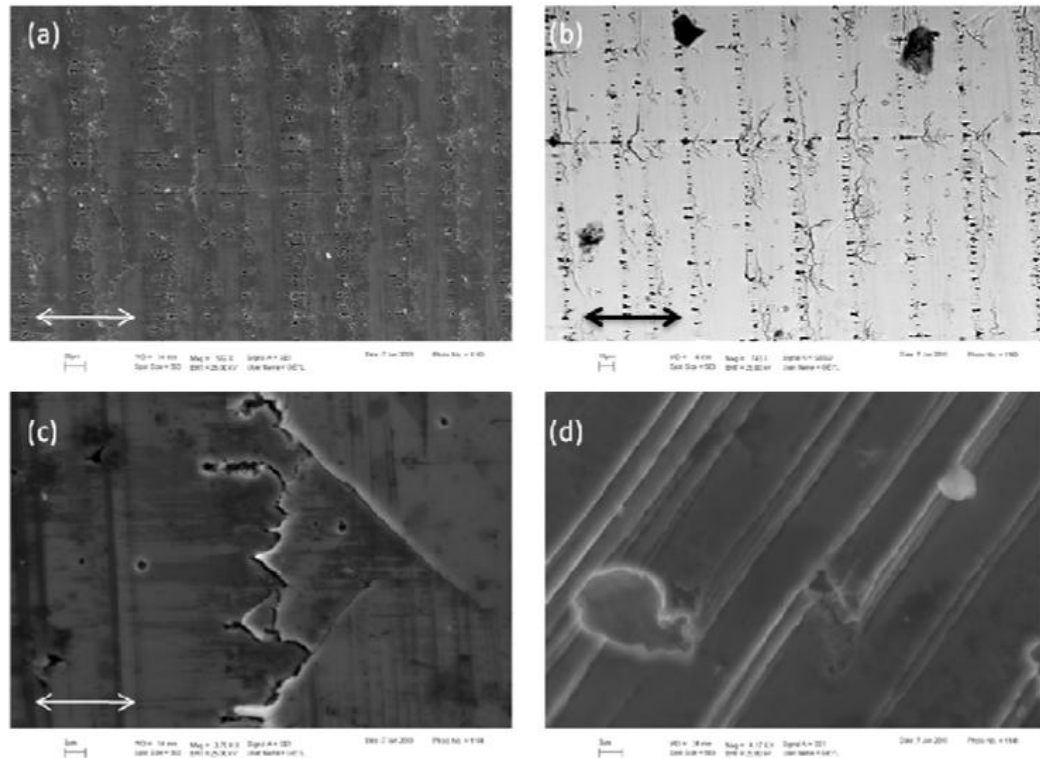
Figure 3.16 Micrographs of 10M Single Crystals After Mechanical Fatigue Testing. A,B) Show Pore Formation at the Twin Boundary and C,D) Show Cracking at the Twin Boundary Which was Often Connected to the Pores. Reprinted with Kind Permission from [67].

Cracks and voids are caused by dislocation pile ups. The pile ups initiate new surface in order to relax the high stress concentration [7, 17, 19, 53, 67]. Dislocation pinning by defects such as surface deformation, impurity atoms, or inclusions, decrease twin mobility [7, 17, 19, 53, 67, 68]. Twinning incompatibilities also hinder twin mobility through dislocation repulsion between twin variants. Twin interactions can therefore severely impact the strain and performance of MSMAs.

3.5.3   Martensite Variant Selection Via Training

Without internal or external constraints, all directions of Bain Strain and lattice invariant shear associated with twin formation are equally likely. Thus all twin variants have equal formation energies during the martensite phase transformation, and a self accommodated structure will arise [6]. However, if some external force is applied, martensitic variants with transformation strain in the direction of the force will have a lower non-chemical free energy term and therefore be more favorable to form. Hence, applying force during the martensite phase transformation allows for selection of a twinning system [7, 17, 68]. Twinning system selection is often referred to as training. Mechanical and magnetic forces can be used for training and are referred to as thermo-mechanical and thermo-magnetic training. Training can also proceed without thermal assistance. Deformation either mechanically or by magnetic field, moves twin boundaries such that after many cycles of deformation unfavorable twinning systems are eliminated [7, 17, 68]. Training is one method commonly used for reduction of twinning incompatibilities, and increasing twin boundary mobility.

3.6   Polycrystals

3.6.1   MFIS in Fine Grained Polycrystals

In polycrystalline materials the mechanical properties are dependent of the grain size. For example, the yield stress follows the Hall-Petch relationship.

$$\sigma_y = \sigma_o + \frac{K}{\sqrt{d_{gb}}} \tag{11}$$

The smaller the grain size d_{gb} the higher the yield stress where σ_o is the single crystalline

yield stress and K is a constant [69]. Smaller grains are therefore better for hardening, as

the dislocation motion responsible for plasticity, is hindered by the grain boundaries. In

MSMAs the yield stress must be low to allow for twin boundary motion during the

application of a magnetic field. Therefore very little MFIS can be achieved in fine

grained materials.

3.6.2   Grain Boundary as Internal Constraints

Grain boundaries will suppress twining due to internal geometric constraints at

the grain boundary. At the grain boundary twinning incompatibilities will wither lead to

the formation of voids or suppression of twin boundary motion. Grain boundaries can

constrain MFIS (or inhibit twin boundary motion) in a polycrystalline material in

multiple directions depending on the grain structure and the direction of strain (Figure

3.17). For comparison single crystals have no grain boundaries and can show up to 6 and

10% maximum strain for 10M and 14M respectively. Ni-Mn-Ga fibers with bamboo

grains where grains span the thickness of the fiber have one dimensional constraints.

Fibers with bamboo grains have been reported to show up to 1% MFIS [70]. Thin films,

in which the grains span the thickness of the film, have two dimensional constraints and

show up to 0.04% MFIS [71]. Bulk large grained polycrystals of Ni-Mn-Ga have three

dimensional constraints and show minimal MFIS. MFIS of up to 0.3% is only found in

highly textured, mechanical trained, bulk polycrystals [32, 33, 35]. Upon heating to temperatures close to the martensite phase transformation the MFIS may increase to 1% due to temperature effects on twin boundary mobility [33]. Texture diminishes incompatibilities across the grain boundaries. Training further reduces twinning incompatibilities within the grains [32, 33, 72].
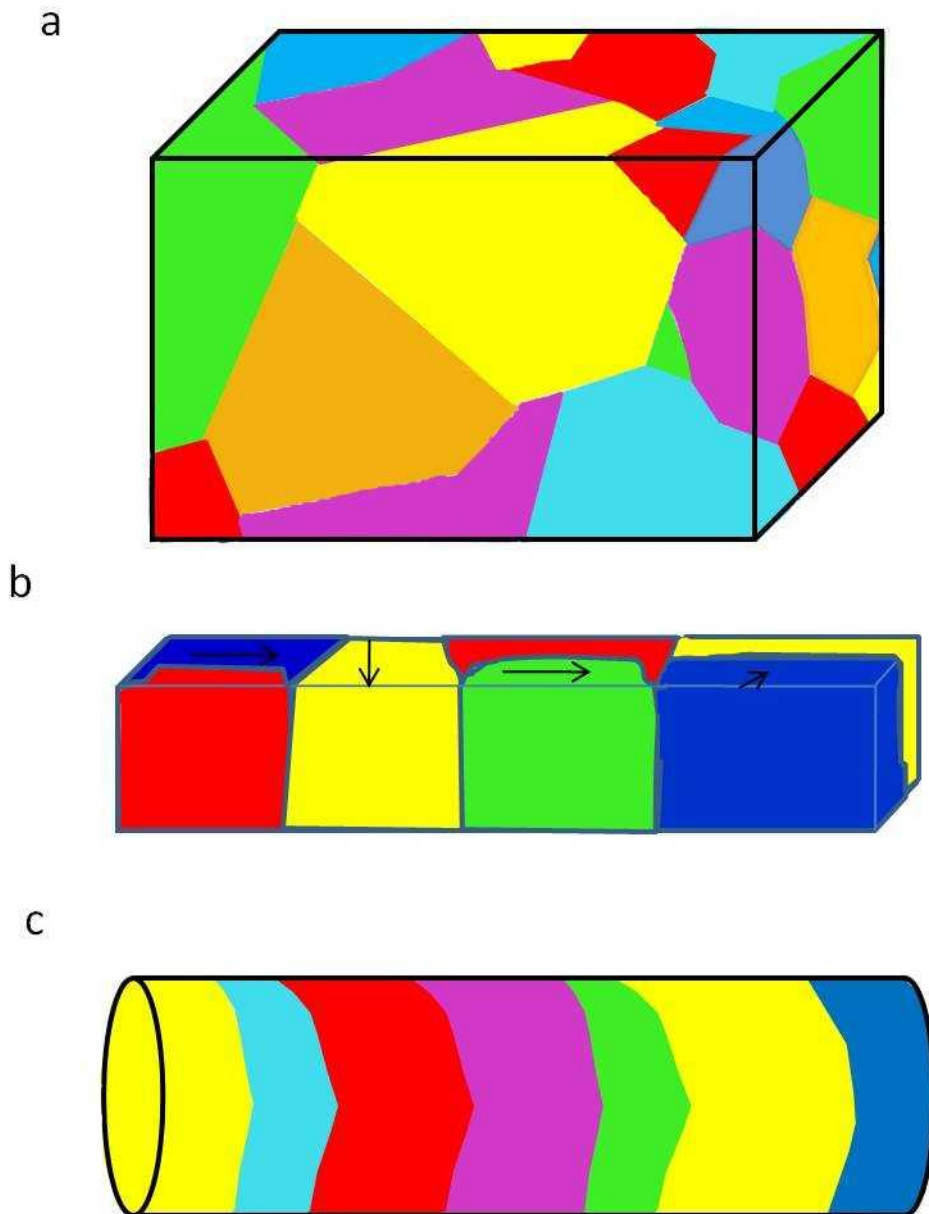
Figure 3.17 Grain Structures in Different Polycrystalline Magnetic Shape Memory Alloys. a) Bulk Course Grained Polycrystal having Three Dimensions of Constraint on Twin Boundary Motion B) Thin Films where Grains Span the Thickness of the Film having Two Dimensions of Constraint on Twin Boundary Motion and C) Fibers Showing One Dimension of Constraint on Twin Boundary Motion.

Recently textured platelet polycrystals (Figure 3.18) demonstrated 0.16%

MFIS.[38] The textured platelets grain boundary network where most grains span the

length of the sample. The textured platelets have smaller grains than the samples

reporting 0.3% strain. Because of the geometry of the grains the textured platelets can

show half of the strain reported for large grained textured polycrystals.   The above

combined data suggests that not only does the dimension of constraint affect strain but

grain boundary volume fraction is also crucial in enhancing MFIS [73].
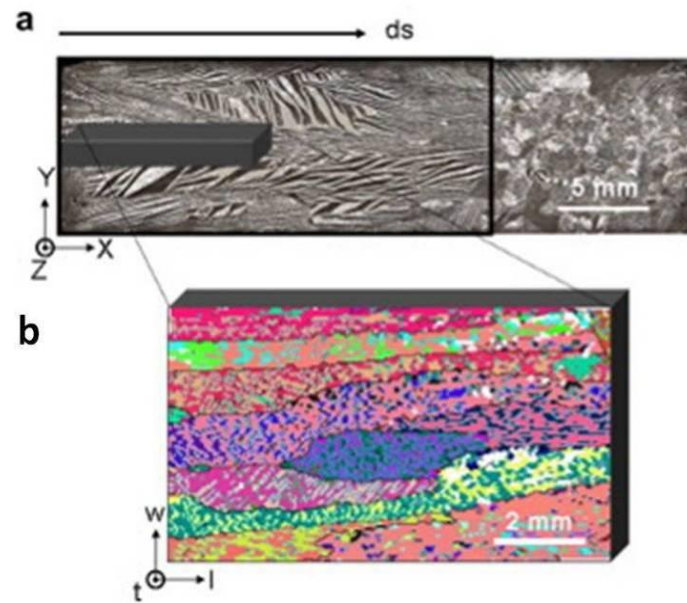
Figure 3.18 Micrographs of Platelet Geometry. A) Microstructure of an Entire Directionally Solidified (ds) Polycrystal Detailing Where the Platelet Sample was Cut. B) EBSD Map of Platelet Sample Showing Grain Structure and Texture. Reprinted with Kind Permission from [38].

3.6.3 Porosity to Enhance MFIS

Another method of reducing grain boundary volume fraction without introducing texture is to introduce porosity. Pores take up the grain boundaries as seen by comparing Figure 3.19 a and b. Introducing pores result in a porous network of bridging metal called struts which connect at points called nodes (Figure 3.19c). Further, after introduction of porosity the remaining struts are mostly single crystalline (Figure 3.19b) leaving the grain boundaries in the nodes thus reducing the constraint on twin boundary motion of the whole network.
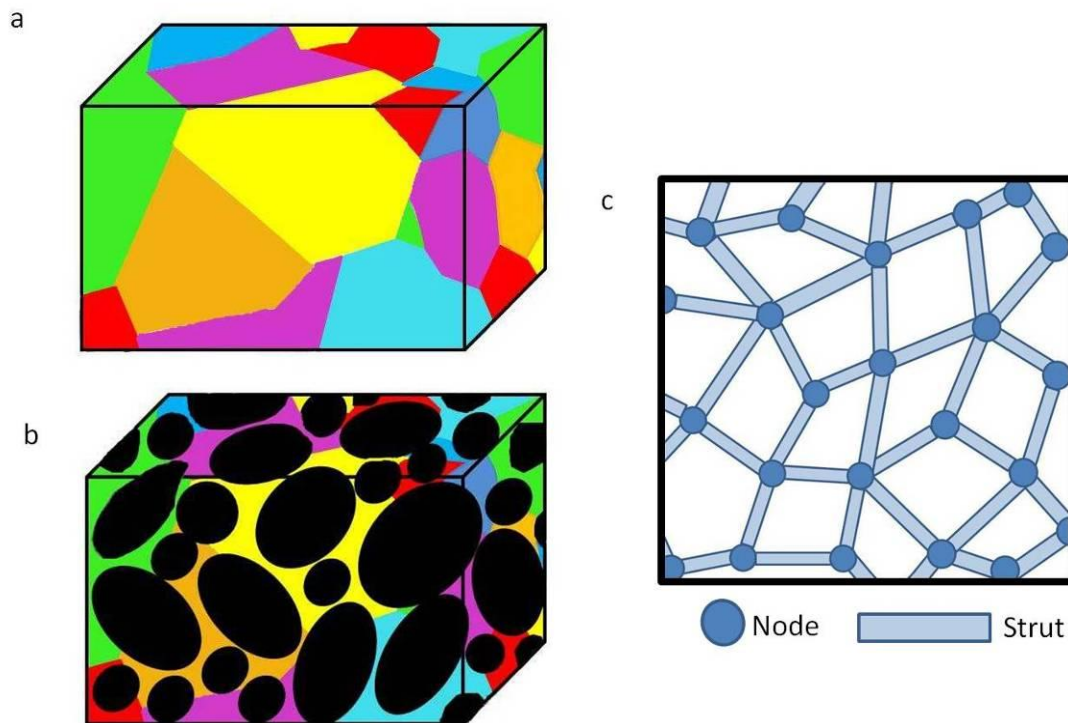
Figure 3.19 Adding Porosity Reduces Grain Boundary Volume and Results in a Network of Struts. A) Bulk Polycrystalline Material Before and B) After Addition of Porosity. After Addition of Porosity the Material Becomes a Network of Bridging Metal "Struts" And Nodes.

3.6.3.1   Foam Deformation Mechanisms:

The free space of the pores opens avenues for further mechanisms of deformation

besides twin boundary motion. A typical stress strain curve, in compression, for metal

foams (Figure 3.20 left) usually shows an initial elastic deformation region followed by a

plateau of plastic deformation, and upon additional stress the metal foam starts to

densify[74]. Densification can clearly be seen in shock testing where the foam cells have

collapsed to a low porosity behind the shock front (Figure 3.20 right)[75].
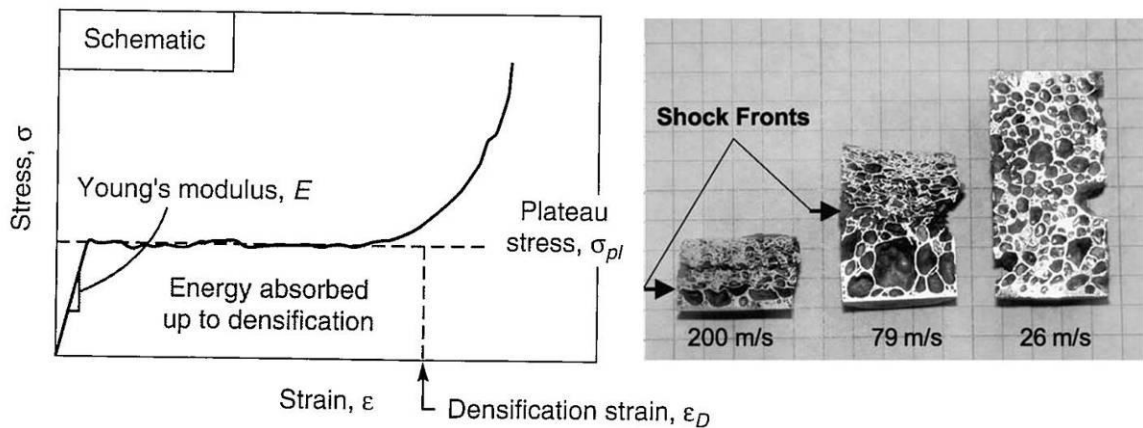
Figure 3.20 Metal Foam Deformation During Compression. Right) Typically Foam Deforms First by an Elastic Deformation Region Followed by a Plateau of Plastic Deformation, and Finally Densification Occurs Through Cell Wall Collapse. Left) Illustration of Densification Through Cell Wall Collapse During Taylor Cylinder-Hopkinson Bar Impact Testing in a Metal Foam. Reprinted with Kind Permission from [74, 75].

In an open cell metallic foam (Figure 3.21a) deformation modes such as: strut

bending (Figure 3.21b), buckling (Figure 3.21c), and hinging (Figure 3.21d) may occur.

In bending mode of deformation in an open cell metal the struts normal to any force will bend, typically this is an elastic process. Buckling mode occurs in the struts parallel to the force. Additionally, strut bending occurs in the struts normal to the force to balance the torque. Lastly when the struts parallel to the force are rigid the corners or nodes can act as hinging points allowing the struts normal to the force to tilt or rotate.
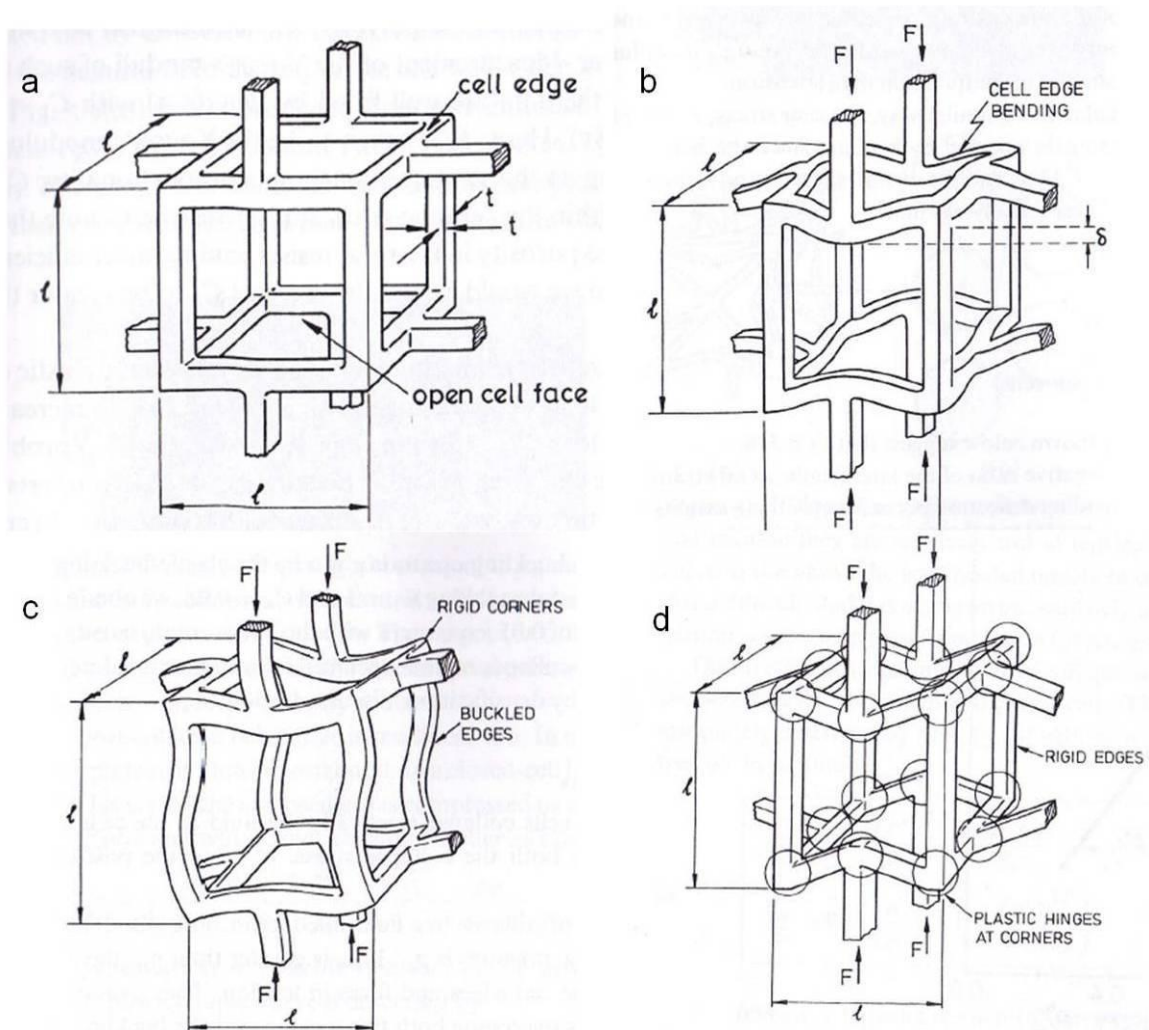
Figure 3.21 Deformation Mechanism in an Open Cell Metallic Foam. A) Open Cell Without Deformation. As Force is Applied B) Struts Normal to the Force Will Bend C) In Addition the Struts Parallel to the Force May Buckle C) If Struts are Rigid the Nodes May Act as a Hinging Point. Reprinted with Kind Permission from [75].

4   EXPERIMENTAL

4.1 Materials

4.1.1   Parent Ingot Casting

99.9% Nickel pellets (ESPI), 99.9% electrolytic Manganese (Alfa Aesar) and 99.999% Gallium (Alfa Aesor) pellets were mixed to give the nominal composition shown in Table 4.1 and was induction casted with a Reitel casting furnace into copper molds. This solid ingot was then used for foam fabrication.

4.1.2   Foam Fabrication

All Ni-Mn-Ga foam (NMGF) samples were made by Northwestern University in Evanston Illinois under the direction of Dr. David C Dunand. Foams were cast by either Dr. Xuxei Zhang or Peiqi Zheng. In a collaborative effort the NMG foam was characterized where processing was focused on by Northwestern University and performance and magnetic properties were characterized at Boise State University.

Two types of foam architectures were investigated: single pore with a mono-modal pore size distribution and dual pore with a bi-modal pore sizes distribution. Examples of the two architectures are shown in Figure 4.1. The topography of the SEM images and the optical micrographs demonstrate that the strut thickness is much greater in the mono-modal foam than in the bimodal foam.
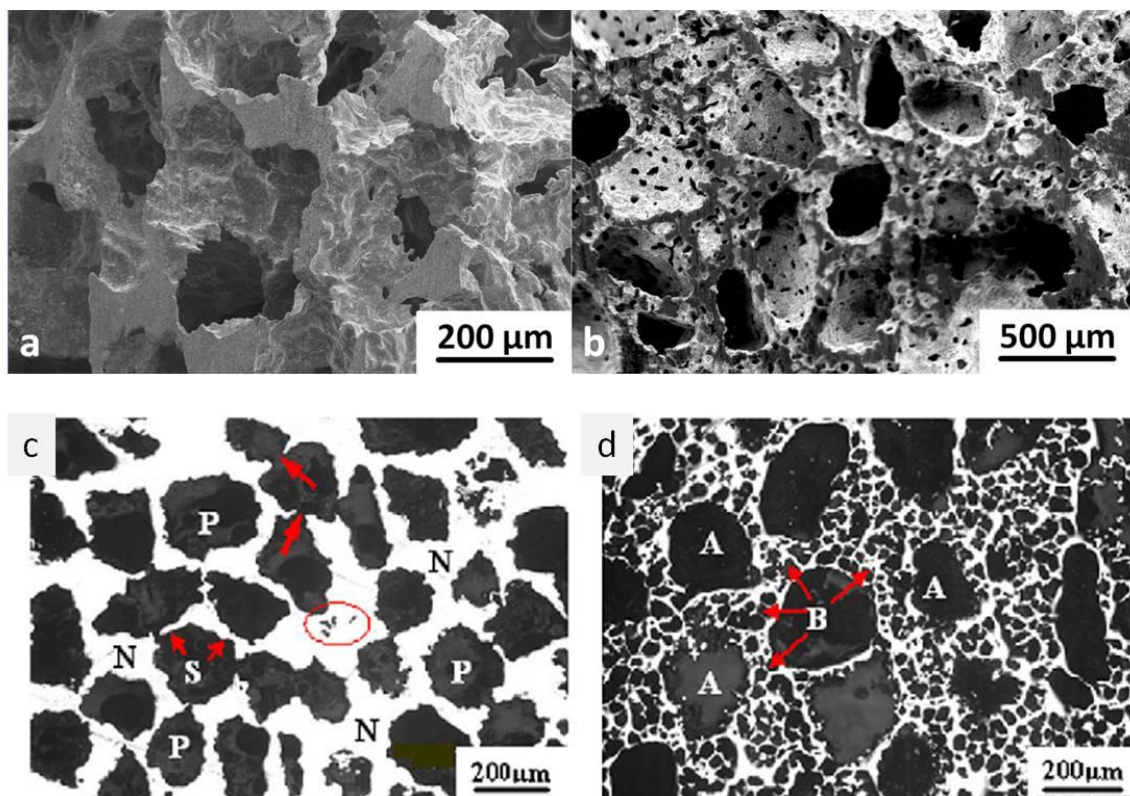
Figure 4.1 A) SEM Micrographs of Single Pore Foam with a Mono-Modal Distribution of Pores, and B) Dual Pore Foam with a Bimodoal Pore Distribution. Optical Micrographs of C) Single Pore Foam with Struts Labeled S, Nodes Labeled N and the Pores Labeled P.

Single pore foam was easier to prepare because the single pore size allowed for easier mixing of space holder. Dual pore foam was easier to etch because of thinner walls between pores. To create Ni-Mn-Ga foam molten metal was infiltrated through a pre-

form of ceramic powders. The ceramic powder was subsequently removed and therefore

acted as a space holder during casting to become future pores (Figure 4.2).
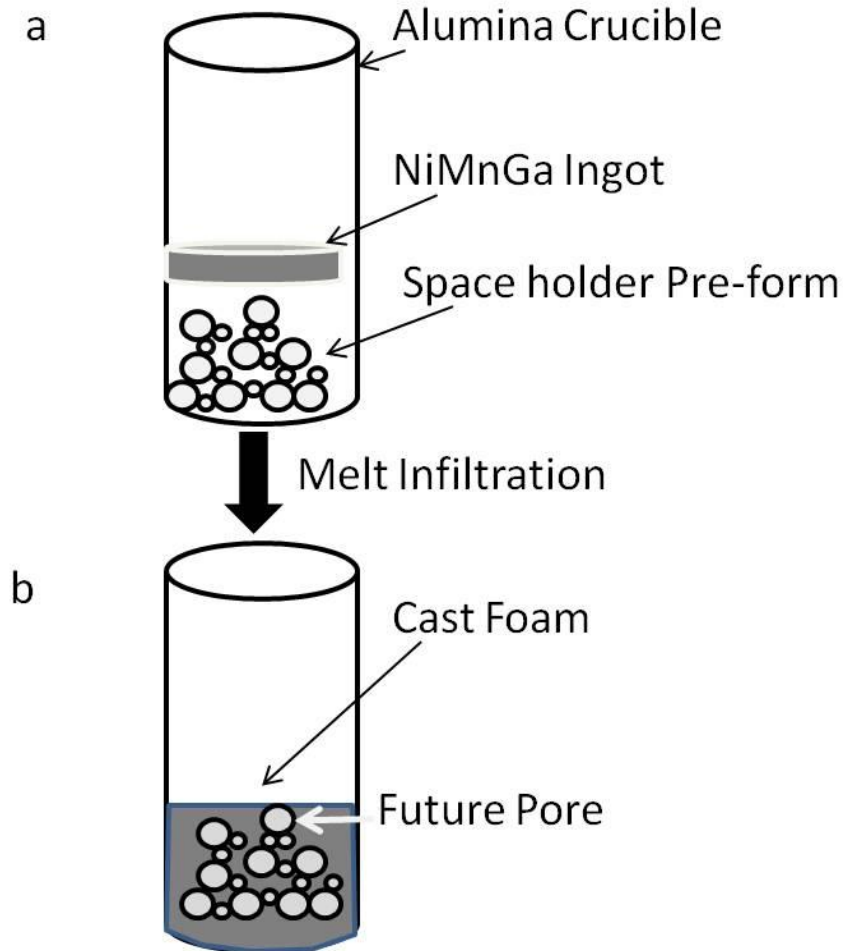
Figure 4.2 Illustration of the Replicate Casting Method for Manufacturing Metal Foams. In an Alumina Crucible A) a Polycrystalline Ingot is Placed on Top of a Partially Sintered Ceramic Perform (Circles) B) Ni-Mn-Ga Ingot is Melted and Fills the Space Around the Ceramic Space Holder. The Ceramic is Removed After Casting to Become the Pore.

Open-cell, Ni-Mn-Ga foams were created by the replication casting method

(Figure 4.2). Liquid metal was infiltrated into a pre-form of sodium aluminate ($NaAlO_2$)

space-holder powders. For bimodal foam the pre-forms were designed to give nominal porosity to be roughly 50%. With a ratio of 73:27 (by weight and volume) of large (500~600 μm) and small (75~90 μm) blend of $NaAlO_2$ powders were used to create the bimodal pore distribution. The blended powders were poured into an alumina crucible with an internal diameter of 9.53 mm and lightly sintered in air at 1500 ˚C for 3 h to create necks between powders, as to ensure no displacement of powders during melt infiltration. The parent ingot was placed on top of the sintered pre-form, which was then heated to 1200 ˚C at 7 ˚C/min under a vacuum of 3.5×10^{-6} torr. The temperature was maintained at 1200 ˚C for 24 mins and high-purity argon gas was introduced in the furnace at a pressure of 1.34 atm to push the molten alloy into the preform. At the same time the temperature was dropped at 7 ˚C/min. The foam was chemically homogenized (1000˚C/1h) in vacuum and then subjected to a stepwise heat-treatment to establish the $L2_1$ structure (725 ˚C /2h, 700˚C /10h, 500˚C /20h).

4.1.3   Samples

Samples were named according to two naming conventions. First foams were named by date followed by a letter, therefore if the names contain the same date the samples are from the same foam rod. Secondly Ni-Mn-Ga foam parent ingot number AR[1-100], then by foam cast number AR[1-100]_[a-f], and lastly a number indicating it position within the foam rod AR[1-100]_[A-f]_[1-100]. Table 4.1 shows a list of all samples, sample properties and the specific study in which the sample was used in.

Table 4.1 List of Samples Detailing the Porosity, Composition, Architecture and the Study the Sample was used in.

Sample Name	Porosity	Composition	Architecture	Study Sample was Used in
8-1 b	54.7%	$Ni_{50.6}Mn_{28}Ga_{21.4}$	Dual Pore	Training, Phase transformation
8-1_HCL	57.1%	$Ni_{50.6}Mn_{28}Ga_{21.4}$	Dual Pore	Training, Phase transformation
4-8 H2SO4	50.0%	$Ni_{52}Mn_{24.4}Ga_{23.6}$	Dual Pore	Training, Phase transformation
4-23_1	54.2%	$Ni_{50.6}Mn_{28}Ga_{21.4}$	Dual Pore	Training
4-23_2	51.0%	$Ni_{50.6}Mn_{28}Ga_{21.4}$	Dual Pore	Training, Phase transformation
4-23_3	53.08%	$Ni_{50.6}Mn_{28}Ga_{21.4}$	Dual Pore	Training, Phase transformation
AR0_A2	59.1%	$Ni_{50.6}Mn_{28}Ga_{21.4}$	Dual Pore	Training
AR0_B6	69.3%	$Ni_{50.6}Mn_{28}Ga_{21.4}$	Dual Pore	Training
AR0_D6	63.9%	$Ni_{50.6}Mn_{28}Ga_{21.4}$	Dual Pore	Phase transformation
AR20_C2	62.7%	$Ni_{52.3}Mn_{24.3}Ga_{21.4}$	Dual Pore	Training, Phase transformation, Pore Architecture
AR20_C3	60.4%	$Ni_{52.3}Mn_{24.3}Ga_{21.4}$	Dual Pore	Training
AR20_C11	58.8%	$Ni_{52.3}Mn_{24.3}Ga_{21.4}$	Dual Pore	Training, Phase transformation
AR20_C12	64.0%	$Ni_{52.3}Mn_{24.3}Ga_{21.4}$	Dual Pore	Training, Pore Distribution, Phase transformation
AR20_C13	62.4%	$Ni_{52.3}Mn_{24.3}Ga_{21.4}$	Dual Pore	Training, Phase transformation
AR26_E1	56.5%	$Ni_{52}Mn_{24.4}Ga_{23.6}$	Single Pore	Pore Architecture
AR49_F1-S1	66.6%	$Ni_{50.6}Mn_{28}Ga_{21.4}$	Dual Pore	Pore Distribution, Phase transformation
AR49_F2-S2	71.1%	$Ni_{50.6}Mn_{28}Ga_{21.4}$	Dual Pore	Pore Distribution, Phase transformation
AR49_F2-S3	67.0%	$Ni_{50.6}Mn_{28}Ga_{21.4}$	Dual Pore	Pore Distribution, Phase transformation
AR56_I2_S1	46-56%	$Ni_{52}Mn_{24.4}Ga_{23.6}$	Dual Pore	Porosity Study,
AR56_I2_S2	53-62%	$Ni_{52}Mn_{24.4}Ga_{23.6}$	Dual Pore	Porosity Study
AR59_G2-S1	70-73%	$Ni_{52}Mn_{24.4}Ga_{23.6}$	Dual Pore	Porosity Study
AR75_K6_S2	50.8%	$Ni_{55}Mn_{20}Ga_{25}$	Single Pore	Size effects, Phase transformation

4.1.4   Porosity

Parallelepiped samples with a dimension of approximately $6 \times 3 \times 2 \text{ mm}^3$ were prepared using a diamond saw. The shortest dimension of the sample is referred to as the x direction, the longest dimension on the sample is referred to as the z direction and the intermediate dimension is referred to as the y direction. Most of the $NaAlO_2$ powders were removed by immersion in 34% H_2SO_4 under sonication at the temperature 24 ˚C. The samples were secondly immersed in 10% HCl under sonication with a water temperature of 25 °C ±9 °C, for removal of the remaining $NaAlO_2$ space holder and porosity increase via strut thinning. Porosity is defined here as the volume ratio of the pores to the volume of the sample. Therefore the porosity (P) can be determined from measurements of mass of the sample (m_{foam}) and total volume sample without pores (V_{total})

$$P = \frac{V_{\text{pores}}}{V_{\text{total}}} = \frac{V_{\text{total}} - (m_{\text{foam}} \cdot \rho_{\text{Ni-Mn-Ga}})}{V_{\text{total}}}$$

(12)

Where $\rho_{Ni\text{-}Mn\text{-}Ga}$, depends on composition but ranges from 7.9 to 8.2 g/cm^3.

4.2 Methods

4.2.1   Vibrating Sample Magnometer

A vibrating sample magnometer (VSM) DSM Model 10, was used to characterize magnetic properties as well as magnetic transitions. A VSM works based on Faraday's law a changing magnet induction will induce a voltage. A VSM detects magnetization by

vibrating a sample within a coil, such that any dynamic magnetic changes induce a

voltage (Figure 4.3). The induced voltage is therefore proportional to the change in flux

density. Magnetization as a function of temperature, magnetic field strength and field

orientation can be recorded.

The instrument is calibrated with a Ni Standard. To minimize error, the Ni

Standard is saturated and centered within the pickup coil before measurements were

conducted. Magnetization of $2.0 \times 10^6 \, \mathrm{Am^2 \, kg^{-1}}$ is the limit of detection for the VSM. A

magnetic field, up to 2 T, may be produced by a water cooled electromagnet.
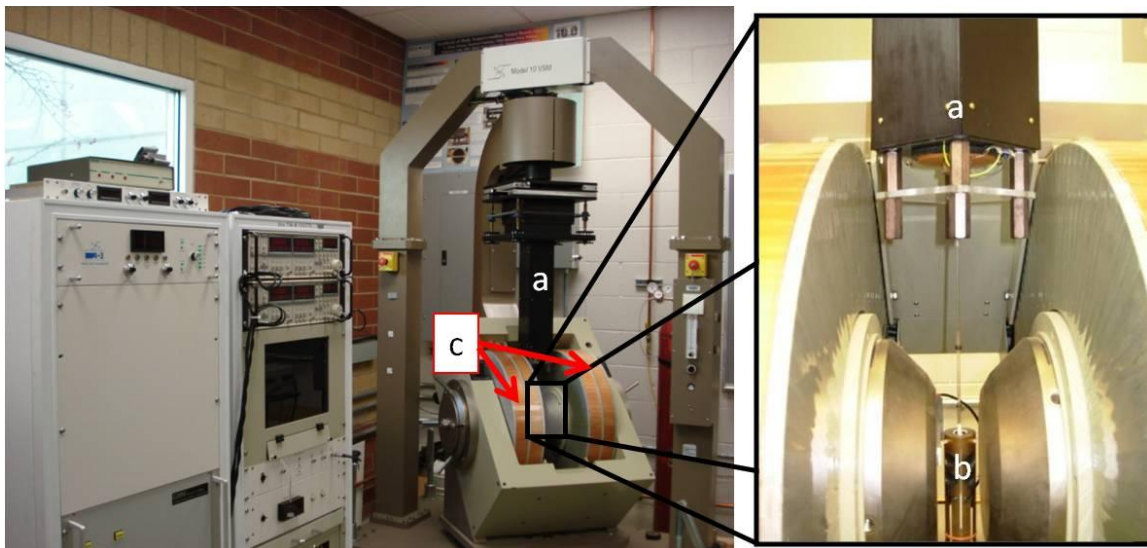
Figure 4.3 Vibrating Sample Magnometer(VSM). Left) is a Zoomed Out View of the VSM where a is the Vibration Unit and c is the Electromagnet Used to Produce the Magnetic Field. Right) is a Zoomed in View of the Sample Holder where (a) is the Vibration Unit and (b) is the Coil in which the Sample is Housed to Detect Magnetization.

Magnetization as a function of temperature was recorded by heating and cooling, at a rate of 8.5 °C/min with a 2 minute dwell time, in the presence of a small bias field usually between 0.025 T and 0.032 T. Magnetization changes as a function of temperature will give the Curie temperature and the martensite-austenite phase transformation.

Magnetization is also measured as a function of increasing field strength up to 2 T. In this study only initial magnetization up to saturation were measured and not the full magnetic hysteresis. If a magnetization is recorded as a function of field, with the magnetic field applied to multiple directions of the sample (successively), information can be obtained about the magneto crystalline anisotropy. With static field orientations the shape anisotropy was corrected for by correcting the applied field with the demagnetization factor as described in equation 7.

Demagnetization factors were found using the chart in Figure 4.4 where q is the ratio of the length, in which the field is applied, over the diameter. The shapes with square and ellipsoidal cross sections are shown in Figure 4.4 by the solid and dashed line respectively. However the samples tested in this study are rectangular so the equation for q was adapted such that the diameter is replaced with the area of the plane tested. For example the parallelepiped samples in this study have three different directions x y and z such that the z direction is the longest sample dimension, x is the shortest and y is the

intermediate length, when the field is applied parallel to the z direction *1/q* is given by

equation 13.

$$\frac{1}{q} = \frac{\sqrt{x^2 + y^2}}{z}$$

(13)
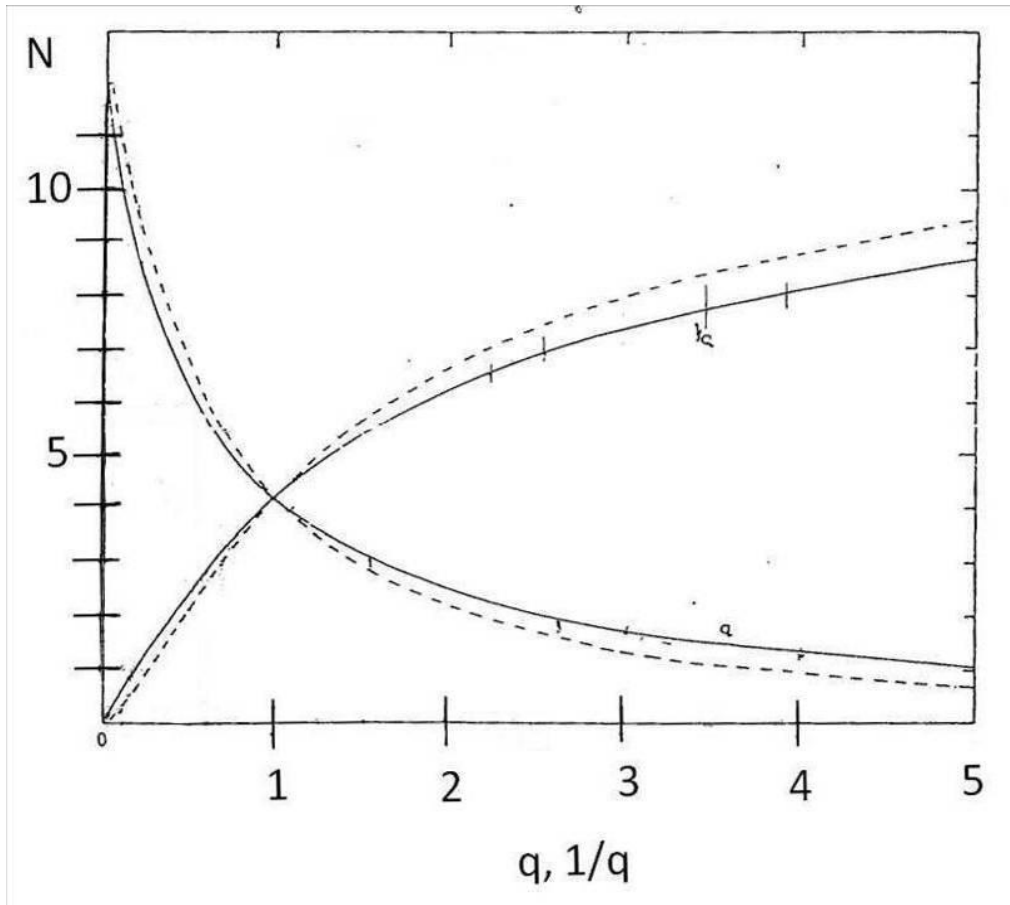
Figure 4.4 Demagnetization Factor *N* as a Function of *q* or *1/q* a Ration of Sample Dimensions. Solid Lines are Demagnetization Factor for Square Shape, and Dotted Lines are the Demagnetization Factor for Ellipsoid Shapes. Reprinted in [76] from the Work of Rhodes and Rowlands in 1954.

Easy and hard magnetization directions can be probed by rotation of a constant,

0.10 mT magnetic field, around the sample while magnetization is recorded (field

orientation dependent magnetization). As the field rotates the magnetization will change

due to the shape anisotropy and any magneto crystalline anisotropy. Shape anisotropy is

expected to show a relative change in magnetization during field rotation of about 10%

based on experiments for parallelepiped samples. For field orientation dependent

magnetization measurements shape anisotropy was not corrected for.

4.2.2   Magneto Mechanical Testing

Rotation of a magnetic field around a magnetic shape memory alloy will allow for

a direct observation of magnetic field induced strain. Due to twin boundary motion in Ni-

Mn-Ga when a single crystal is subjected to a rotating magnetic field, it will expand and

contract twice during one full field revolution (Figure 4.5).
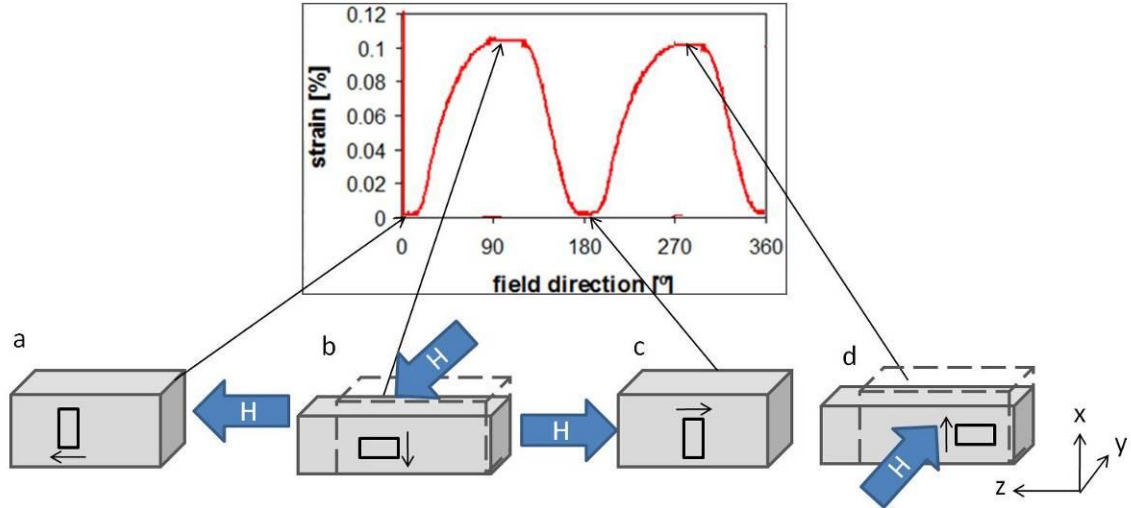
Figure 4.5 Magnetic Shape Memory Effect of A Single Crystal in a Rotating Magnetic Field. A) with A Magnetic Field Applied 0° from the Long Axis of the Sample (Blue Arrow) the Short Axis of Unit Cell (Arrow With Black Box) is Aligned Parallel to the Long Axis of the Sample (Gray) Resulting in Zero Strain. B) When the Field is Rotated About the X Axis to 90° Now the Long Axis of the Unit Cell is Aligned with the Long Axis of the Sample therefore Causing an Elongation as Compared to the Original Length(Dashed Box). C) As the Field Rotates to 180° The Sample Returns to the Original Shape Therefore Showing Zero Strain. D) When the Magnetic Field Rotates to 270° the Sample Again Elongates as Seen with the Magnetic Field 90° from the Sample. Therefore a Magnetic Shape Memory Alloy Will Expand and Contract Twice for Every One Revolution of a Magnetic Field.

In the lower symmetry martensite phase, the easy direction of magnetization, is coupled with the shorter crystallographic length, which is shown in Figure 4.5, marked by the arrow on the tetragonal cell. Within the unit cell the easy direction (i.e. short axis) will align the magnetic field. When the field is aligned with the long axis, or is at 0°(Figure 4.5 a,c) to the sample the strain will be at a minimum. When the field is at 90° to the sample the strain should be at a maximum as the long axis of the unit cell is aligned with the long axis of the sample. (Figure 4.5 b,d) . Thus, from 0-180° rotation of the magnetic field is one magneto-mechanical cycle (MMC) and is one cycle of expansion

and contraction. However in polycrystalline samples the expectation of magneto-mechanical behavior is not as straight forward. The maximum of strain can be seen at field angles deviating from 90° because the grains have different crystallographic orientation within the sample, and different relative sizes. Further since multiple grains can deform at different field angles broad peaks of maximum strain may be observed as well as multiple MFIS maxima.

4.2.2.1 Magneto-Mechanical Cycling

A magnetic field of $0.97T$ was rotated about x axis shown in Figure 4.6. In order the measure the MFIS accurately that sample (1) is held with glue by a stationary bracket (2) on one side and movable (sliding head, 3) bracket on the other side. Sliding head displacement is guided on the sides and on the top (not shown) in order to limit sample bending (Figure 4.6 b). The sliding head displacement was translated to an extensiometer (6) (Heidenhain, type MT1281) via a ceramic rod (5). All sample mounting parts were made from self lubricating Vespal ^{C} to limit friction that would hinder MFIS. The displacement (engineering strain) measured was only relative to the samples long (Z) axis. Measurements were taken at a rotational speed of 30 rpm to minimize error due to vibrations [77]. MFIS from magneto-mechanical cycling was measured at a constant temperature of 19 °C ± 2 °C.
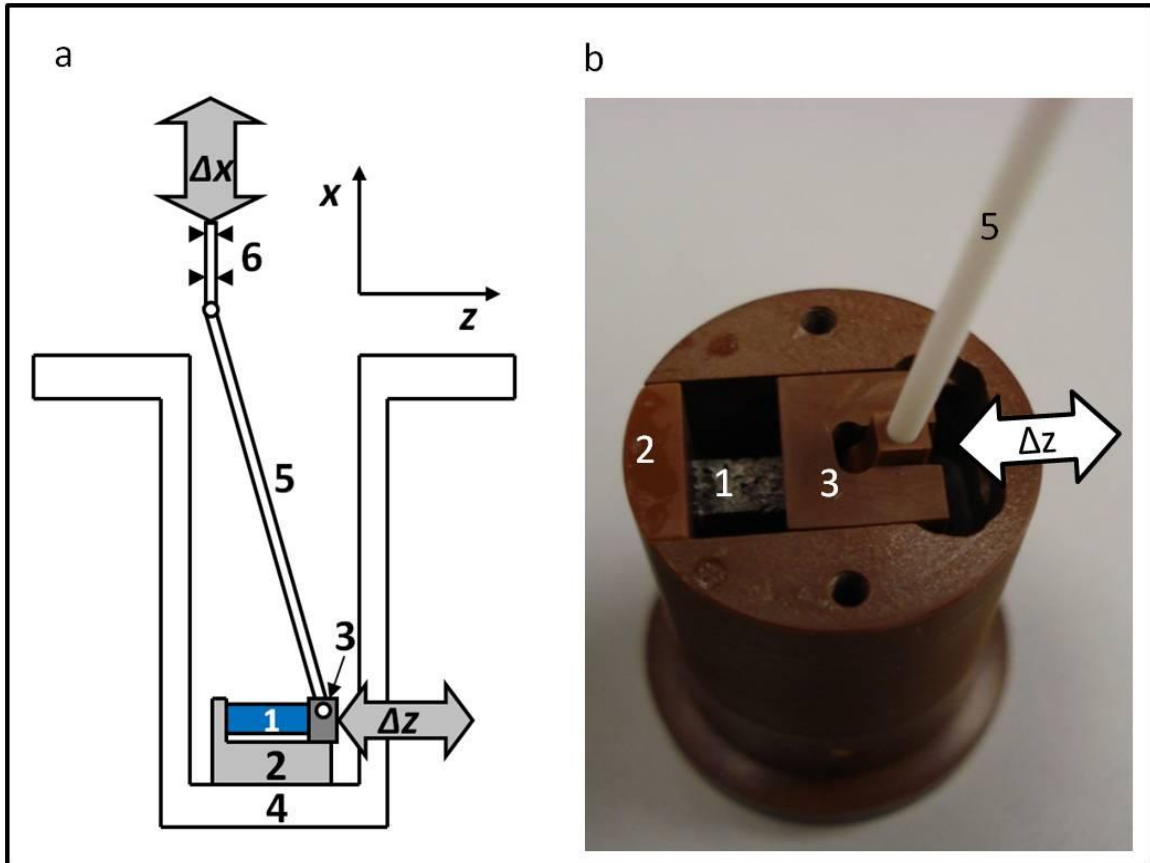
Figure 4.6 Measuring Magnetic Field Induced Strain. The Sample (1) is Held With Glue by a Stationary Bracket (2) On One Side and Movable (Sliding Head, 3) Bracket on the Other Side. Sliding Head Displacement *Δz* is Guided on the Sides B) and on Top with a Lid that is Not Shown Here. The Sliding Head Displacement is Translated to *Δx* Via a Ceramic Rod (5) to an Extensiometer (6) that Measures Displacement.

To determine experimental error, a measurement a low carbon steel sample was tested in the magneto-mechanical measuring device. Steel was chosen because it has a high magnetization and thus a large torque in a rotating field yet no magnetoplasticity. Such that the signal detected for magneto-mechanical cycling of steel should be zero. Therefore any error would be taken as the MFIS detection limit. Figure 4.7 is four averaged field revolutions of low carbon steel glued on both sides (as is the foam). Figure

4.7 shows no maximum or minimum as would be expected for sample holder bending.

Averaging the curves reduces signal noise. However Figure 4.7 may still show some

noise (~330°) since only four cycles were averaged. Therefore 0.002% is the limit of

detection for MFIS during field rotation which was based on the width of the signal

detected. Further NMG foam had a minimal magnetic attraction due to the

polycrystallinity therefore it is expected the error in measuring MFIS in foam is minimal.

In addition to low error in measuring MFIS in foam it is expected that the restriction of

twin boundary motion from the glue is limited due to porosity.
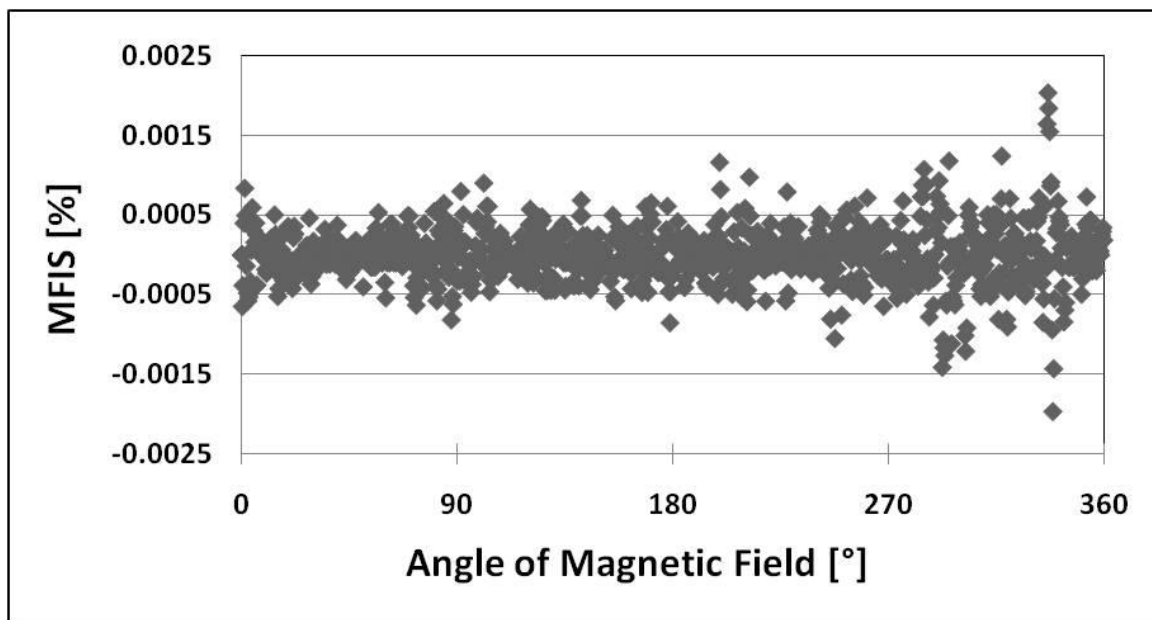
Figure 4.7 Calibration of Magneto-Mechanical Cycling With 1018 Steel. The Calibration Showed that there is No Detectable Error Introduced from the Sample Holder Bending.

4.2.2.2   Thermo Magneto-Mechanical Cycling

During field rotation the samples were heated and cooled through the martensite

phase transformation, which is called thermo magneto-mechanical cycling (TMC). TMC

allows for in situ observation of the martensitic phase transformation, thermo magneto-

mechanical training, and MFIS produced by a sample in a fully martensitic state which

may be below the operating temperature of the system. Heating and cooling of the sample

was achieved through introduction of hot or cold air into the sample chamber. The

sample temperature was measured via a thermocouple with direct contact to the sample.

The temperature was averaged over one revolution (cycle) of the magnetic field. The

maximum MFIS for one magnet revolution was plotted against the temperature for the

corresponding cycle. TMC allowed for MFIS as low as 0.01% to be accurately

measured. Room temperature cycling can measure strains as low as 0.002% so the added

error of the TMC is due to the vibrations of the forced air flow.

4.2.3   X- ray Diffraction

X-ray diffraction XRD was used to characterize the crystal structure of Ni-Mn-Ga

foams. X-ray waves interact with the periodic medium due the crystalline nature and

results in diffraction according to Bragg's law.

$$n\lambda = 2d \sin \theta$$
(14)

Where n is an integer multiple, λ is the wavelength, d is the lattice spacing and 2θ is the

angle between the incident wave and exigent diffracted wave. In essence when the lattice

spacing is an integer multiple of the wave length, diffraction will occur at a characteristic angle.

A Bruker D8 discover diffractometer with a Cu Kα source equipped with a Gobel mirror, and a monochromator with a 1.0 mm universal beam collimator and an area detector was used for all diffraction experiments in a parallel beam setup shown in Figure 4.8. NIST Corundum standards were used to characterize the peak position and width. If the peak position was within 0.04° in 2θ of the reference, the detector position was deemed acceptable according to ASTM standards. This gives accuracy of experimentally observed *d* spacings to the 0.004Å.
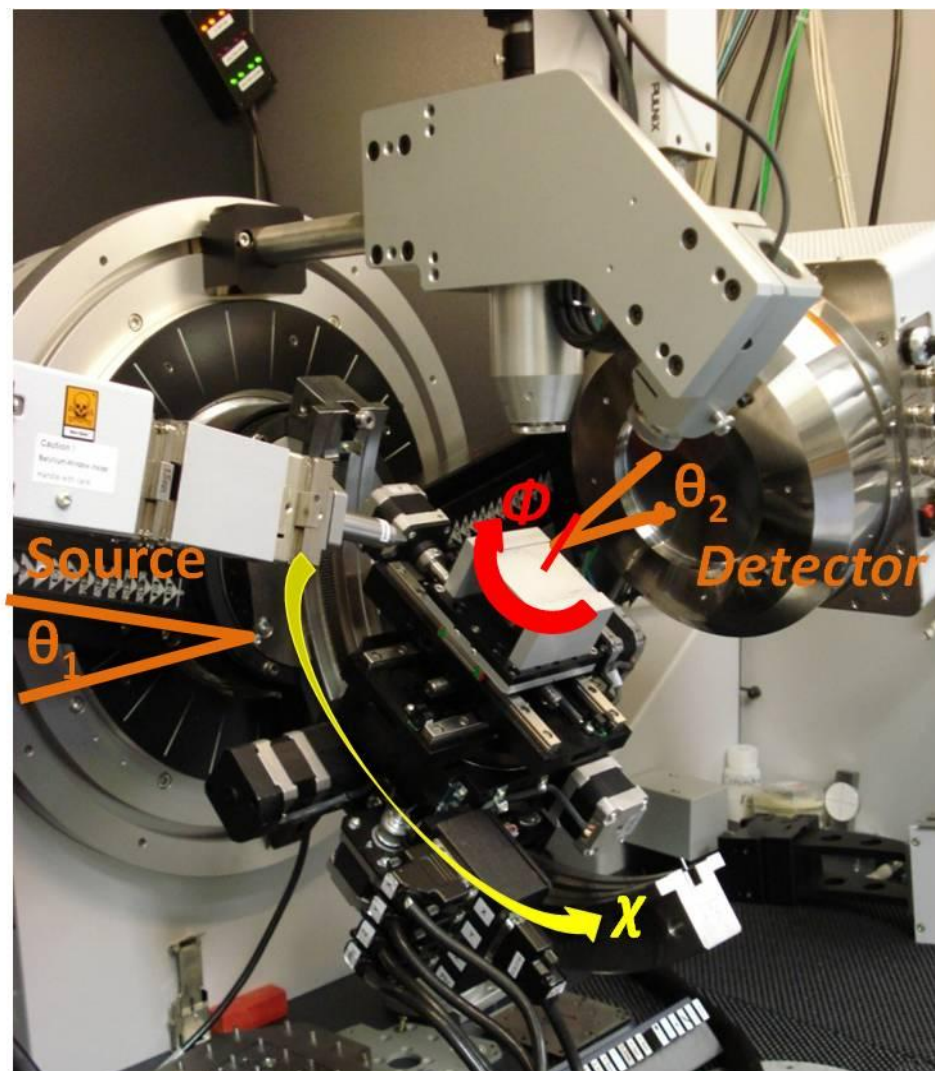
Figure 4.8 X-ray Diffractometer With Parrallel Beam Set Up. Θ$_1$ is the Angle of Inclination of the X-ray Source (Orange), and Similarly Θ$_2$ is the Angle of Inclination of the X-ray Area Detector. Phi Φ (red) is Rotation About the Sample Plane Normal. Chi χ (Yellow) is Rotation Marked with the Yellow Arrow.

4.2.3.1 Crystallographic Texture

Crystallographic texture is a distribution of crystallographic orientations

throughout a sample. Texture can either show crystallographic orientations of no

preference relative to the sample, which is referred to a random texture, or a preferred

orientation relative to the sample. Texture can be represented by the distribution of the normal direction of a crystallographic plane (called poles) which are mapped in a stereographic projection. These pole projections are commonly referred to as a polefigure. A polefigure, will therefore show the distribution of the poles within the volume of the sample that was investigated. For Ni-Mn-Ga foam, the grains were large enough that each grain orientation was distinguishable and easily identified. Therefore a texture measurement could show the number of grains at the surface. Texture was also employed to characterize the change in crystallographic orientation with thermo-magnetic training and to quantify the training effect.
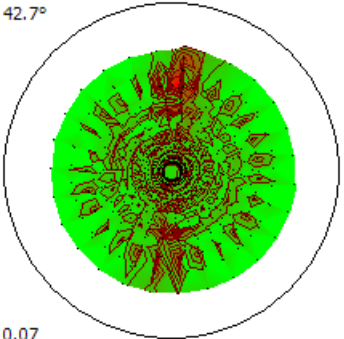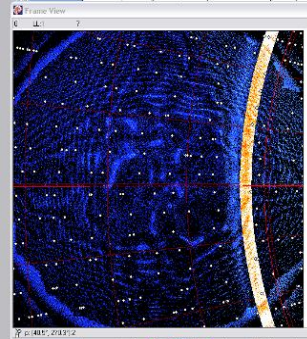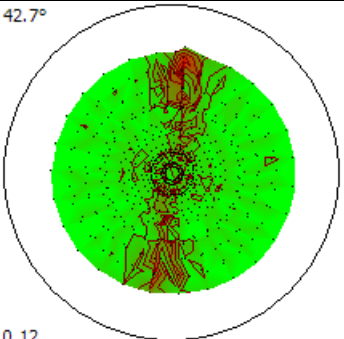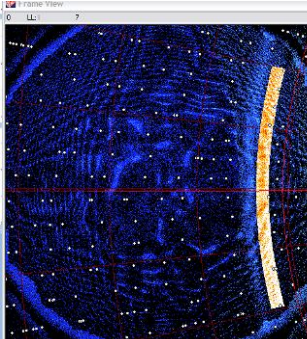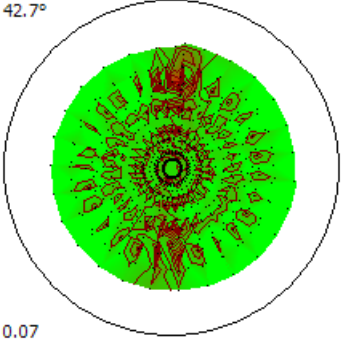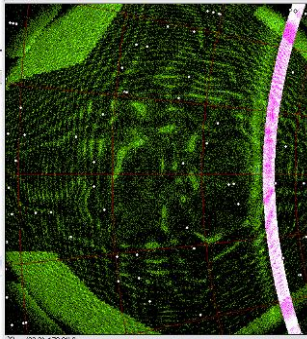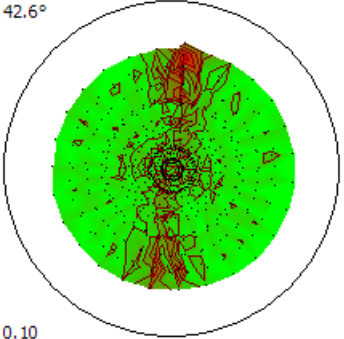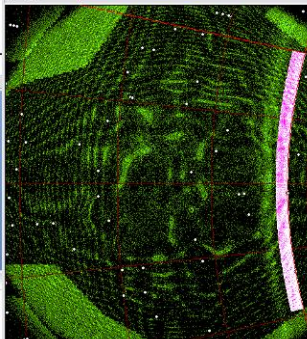
Texture was measured by taking diffraction patterns in discrete steps of Φ, and χ at a constant 2θ angle using an area detector which has a $30°$ 2θ range of detection. The table below shows the plan of Φ, χ and 2θ angles needed to construct a polefigure. Pole planning and texture evaluation was done with the software Multex V2. To construct a polefigure with Multex a 2θ - χ region is highlighted. The highlighted area is then integrated and the diffracted intensity is plotted over χ and Φ coordinates of the pole sphere. Therefore each pole is associated with a χ and Φ angle of the sample. To quantify texture in Multex, crystal orientations must be matched over the polefigure and refined such that all diffracted intensity is accounted for. Also a background grid may be used to remove background intensity from the area detector data.

Table 4.2 Sample Orientations Used to Measure Texture in Ni-Mn-Ga Polycrystals.

Run number	Θ_1[°]	Θ_2[°]	χ [°]	Steps in Φ [°]
1	27.0	27.0	75	13.5
2	27.0	27.0	60	10.3
3	27.0	27.0	45	13.8
4	27.0	27.0	30	10.9
5	27.0	27.0	15	12.0
6	27.0	27.0	0	10.3

A detailed investigation was done on the effect of the 2Θ -χ area used to construct the polefigure, as well as the background removal resolution on the resulting polefigure. Table 4.3 shows resulting polefigures by using different background removal resolutions and different 2Θ -χ regions. With a higher degree of background removal (5 ° resolution) the high background area around the perimeter of the detector is reduced. If the edges of the area detector with high background are included, a ring of intensity shows in the polefigure which would be falsely interpreted as fiber texture. The higher background removal resolution allows for a larger χ range to be included in the polefigure construction. The level of background removal should depend on diffracted intensity and the area of high background should not be included in the polefigure construction.

Table 4.3 Background and 2θ -χ Area Selection Effects of the Resulting Polefigure.

Resulting Polefigure		Chi Range Selected	Background Grid	Area Detector Data
42.7° — 0.78 / 1.48 / 2.19 / 2.90 / 3.60 / 4.31 — 0.07 ... 5.02		0-360	3 mesh 5° resolution	42.1-43.4
42.7° — 1.02 / 1.92 / 2.82 / 3.73 / 4.63 / 5.53 — 0.12 ... 6.43		160.5-199.5	3 mesh 5° resolution	42.1-43.4
42.7° — 0.95 / 1.84 / 2.72 / 3.61 / 4.50 / 5.38 — 0.07 ... 6.27		0-360	3 mesh 15° resolution	
42.6° — 0.91 / 1.72 / 2.54 / 3.35 / 4.16 / 4.98 — 0.10 ... 5.79		160-199	3 mesh 15° resolution	

4.2.4   Neutron Diffraction

Neutrons are non charged particles with both mass and spin[78]. Debrogile's

relationship describes all particles as having wavelike properties depending on the mass

and velocity of the particles[78]. The wavelike property of neutrons can be used for

characterization of materials via diffraction. Neutrons also interact very little with

materials, lending to a much larger penetration depth[79, 80]. The high penetration depth

allows for a very large volume of material to be probed. Neutrons scatter from the

nucleus and not the electrons orbiting of an atom. Nuclear scattering allows for

differentiation of atoms with similar electronic structure, and allows for more sensitivity

to lower Z atoms[79, 80].

One way of producing neutrons is spallation. Spallation occurs by protons being

accelerated into a heavy metal target, often tungsten or lead[80]. When the high energy

proton hits the nucleus of the target materials it decays producing 10 plus neutrons[80].

Neutrons produced from spallation have different velocities and therefore different

wavelengths, following DeBrogile's relationship[80]. To utilize neutrons from a

spallation source, neutrons (with varying wavelengths) are allowed to spread out over

time as the neutrons travel from the source to the sample which is deemed a time of flight

technique[80]. The time of flight technique delivers multiple wavelengths of neutrons,

which interact with the sample one wavelength at a time (Figure 4.9 b). This method

allows for multiple Bragg conditions to be fulfilled for one sample orientation, with a fixed detector position[79, 80].

Neutron diffraction texture was conducted at Los Alamos National lab with a Tungsten spallation source using the HiPPO (high intensity pressure preferred orientation) instrument beam line. The HiPPO as rings of detector panels: back scatter, 90°, 40°, 20° and 10° (Figure 4.9a). Each panel in the ring was integrated and added together to give a diffraction pattern.
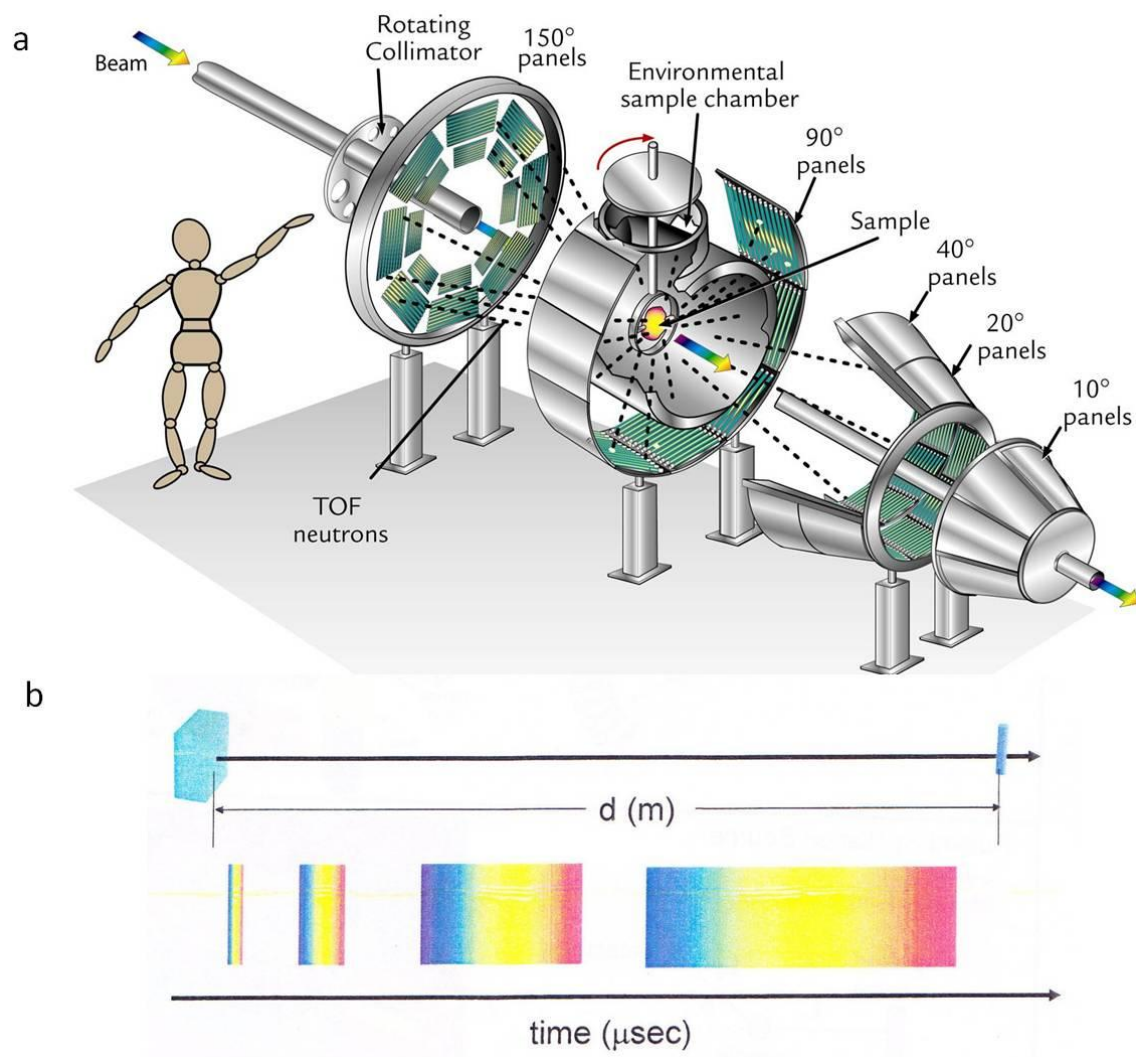
Figure 4.9 Hippo Neutron Diffraction Instrument. a) Geometry of the Detector Panels, Sample, and Beam. b) Time of Flight Technique. As the Pulse of Neutrons Travel from the Source to the Sample the Band Width of the Neutrons Spread Out Allowing for Discrete Wavelengths to Interact with the Sample. Reprinted with Kind Permission of Sven Vogel at Los Alamos Nation Lab.

4.2.5   Electron Dispersive Spectroscopy Compositional Data

Electron Dispersive Spectroscopy EDS is a chemical analysis technique that

works in conjunction with a scanning electron microscope SEM. High energy electrons

come in contact with the surface knocking electrons off atoms resulting in an unfilled electron orbital. An electron from a higher energy shell will give off energy in the form of an x-ray photon and fill the unoccupied state of lower energy. Since all atoms have discrete energy levels the X-ray photon energy is characteristic of the source atoms. The EDS technique can identify atoms (with $Z > 12$) within the interaction volume of the electron beam.

The Chemical compositions were determined by a Hitachi S3400N-II scanning electron microscope (SEM) and Leo 1430 VP SEM equipped with an integrated Oxford EDS system. Copper calibrations were done prior to use, working distance was kept at 15 mm, spot size was 400 ± 50 μm, and accelerating voltage was 15 keV $\pm$ 4 keV. Spot size and accelerating voltage were adjusted to give a dead time of 17% $\pm$ 3%. If sample compositions were compared, all samples were tested with the same beam conditions.

4.3   Studies

NMG foams have many variables that could affect MFIS, among them are: composition, magnetic ordering, crystal structure, crystallographic texture, grain size, magnetic anisotropy, pore architecture, pore distribution and porosity. This thesis focused on specific studies on how the transformation temperature, pore architecture, training, porosity, anisotropy, and pore distribution affected the performance and maximum MFIS. These studies are outlined below.

4.3.1   <u>Martensite Phase Transformation Effects on MFIS</u>

Transformation temperatures were obtained with temperature dependent magnetization experiments and the range of MFIS was obtained by magneto-mechanical cycling. To study if there was a correlation between martensite phase transformation temperature and MFIS the range of MFIS was plotted against the martensite finish temperatures. The samples included in this study are listed Table 4.1 and includes single pore and dual pore foam. Foam was fabricated as described in section 4.1.1-4.1.2 with space holders and strut thinning performed as described in section 4.1.4. Porosities resulting from the etching and space holder removal are also given in Table 4.1. Compositions were not characterized for each sample in this study.

4.3.2   <u>Training</u>

Three forms of training were investigated: magneto-mechanical, thermo-magnetic, and thermo magneto-mechanical training. Samples were fabricated and processed as discussed in sections 4.1.1-4.1.4. The samples used in this study are given in Table 4.1 with nominal compositions and porosity listed. No chemical composition characterizations were done for the individual samples of this study.

Magneto-mechanical training is the elimination of unfavorable twinning systems through magnetic field induced twin boundary motion. Magneto-mechanical training will therefore show an increase in MFIS with magneto-mechanical cycling. Magneto-mechanical training was evaluated based the rate of increase in MFIS during cycling.

Thermo-magnetic training allows for martensite variant selection and may reduce the number of twinning systems present in a specimen thus changing the magneto-mechanical behavior. First magneto-mechanical cycling was conducted to obtain the maximum MFIS and the field orientation dependent MFIS. Next thermo-magnetic training was accomplished by heating the specimen in the VSM past the Curie temperature followed by cooling with an applied magnetic field of 2T. Heating and cooling rates are specified in section 4.2.1. After thermo-magnetic training, magneto-mechanical cycling was conducted to obtain the maximum MFIS and the field orientation dependent MFIS. To evaluate the effect of the thermo-magnetic training on magneto-mechanical properties, magneto-mechanical behavior (i.e. maximum MFIS and angle of strain peak(s)) was compared before and after training.

Thermo magneto-mechanical training was accomplished by in-situ heating and cooling during magneto-mechanical cycling. This form of training will not only reduce twining systems by martensite variant selection but select twinning systems that are highly mobile. Heating and cooling (a thermal cycle) was repeated multiple times without un-mounting the sample. To evaluate the effectiveness of the thermo magneto-mechanical training, the maximum strain for each thermal cycle was compared.

4.3.3 Pore Architecture

Two pore architectures were studied: single pore with mono-modal size distribution and dual pore with a bi-modal size distribution. The two foams AR26_E1 and

AR20_C2 were fabricated and processed as discussed in sections 4.1.1-4.1.4. The nominal compositions and porosity are given in Table 4.1. No chemical composition characterizations were done for the individual samples of this study. Twin morphology, strut size was observed with optical microscopy at Northwestern University. MFIS as a function of magneto-mechanical cycle were compared for two foams AR26_E1 and AR20_C2 in the initial and thermo-magnetically trained state. No training was done for AR26_E1.

4.3.4   Porosity Study

To investigate how the level of porosity impacted the magneto-mechanical properties, foams were systematically studied as porosity was increased. Dual pore samples (AR56_I2_S2, AR56_I2_S1, and AR59_G2_S2) were manufactured as described in section 4.1.2. To evaluate the phase transformation temperatures, temperature dependent magnetization experiments were preformed as described in section 4.2.1. Compositions were evaluated by EDS described in section 4.2.4. Magneto crystalline anisotropy was evaluated by field dependent magnetization measurements with the field parallel to the easy and hard axis of magnetization. To quantify only magneto crystalline anisotropy, shape anisotropy was removed as described in section 4.2.1. The area between the *M-H* curves with the field parallel to the easy and hard axis of magnetization was integrated to give the magneto crystalline anisotropy energy.

For one porosity increase step, the sample was first thermo magneto-mechanically cycled (TMC), then etched to increase porosity (described in section 4.1.4), after which the porosity was evaluated as described by equation 12 (section 4.1.4). Porosity steps were repeated until the sample could no longer be tested. TMC was done because the samples in the porosity study were not martensitic at room temperature and therefore needed to be cooled to show MFIS. The maximum strain for each TMC experiment was plotted against porosity to evaluate the porosity MFIS relationship. Porosity strain correlations were only made per sample which therefore limited extraneous variables from impacting the correlation.

4.3.5 Pore Distribution Study

Dual pore samples AR49_F2_S1, AR49_F2_S2, and AR49_F2_S3 were manufactured as described in section 4.1.2. Three samples AR49_F2_S1, AR49_F2_S2, and AR49_F2_S3 were used for the pore distribution study. To evaluate the phase transformation temperatures temperature dependent magnetization experiments were preformed as described in section 4.2.1. Compositions were evaluated by EDS for the foam and the parent ingot (described in section 4.2.4), and were found to be within experimental error of each other (data not shown). Magneto crystalline anisotropy was first evaluated by field orientation dependent magnetization as described in section 4.2.1. The field orientation dependent magnetization measurements give the angle of easy and hard axis of magnetization for the polycrystalline sample. In addition the relative change in magnetization with field rotation is an indication of magnetic anisotropy where

magnetization changes during rotation of 10% and less are due to shape anisotropy. Secondly magneto crystalline anisotropy was evaluated by field dependent magnetization measurements with the field parallel to the easy and hard axis of magnetization for samples AR49_F2_S1, AR49_F2_S2.

Xray tomography was utilized to characterize the spatial distribution of large and small pores within the sample. The pore distribution was characterized with x-ray microcomputer tomography by Dr. Markus Chmielus. The x-ray radiation was generated by a microfocus tube (Hamamatsu, L8121-03) with a spot size of 7 µm and detected by a flat panel detector (Hamamatsu, C7942SK-05). The scanner was set to an acceleration voltage of 100 keV and a current of 95 µA. The out coming beam was filtered by a 1 mm thick Aluminum plate. The magnification ratio was preset to 7.1 with an effective pixel size of 7.1 µm for the sample. The reconstruction of the data set of 1000 projections was performed using OCTOPUS 8.3 software[81].

Each sample was thermo magneto-mechanically cycled to study the magneto-mechanical properties as well as training effectiveness. The trends in pore distribution homogeneity and anisotropy were compared with the MFIS between samples to conclude any impact of the pore distribution on MFIS.

4.3.6   <u>Size Effects</u>

Single pore foam AR75_K2_S2 were manufactured as described in section 4.1.2 and only space holders were removed as described in section 4.1.4. Porosity and nominal composition are listed in Table 4.1. The foam was consecutively cut in half along the *x-z* plane followed by magneto-mechanical cycling. The magneto mechanical behavior was compared before and after cutting to probe for a sample size affect on the MFIS.

5   RESULTS

5.1 Martensitic Phase Transformational Effects on MFIS

Sample AR0_D6 showed transformation behavior in which the austenite finish temperature was above the Curie temperature. For AR0_D6 the A_s is at 62 °C and the M_f is at 60 °C and A_f and M_s are indeterminate (Figure 5.1 top). The corresponding MFIS for the sample was 0.0015%. These results posed a question of whether the transformation temperature and MFIS were correlated. Below is a semi-log MFIS versus the martensite finish temperature for numerous samples. The error bars in Figure 5.2 indicate the range in MFIS demonstrated by a particular sample.
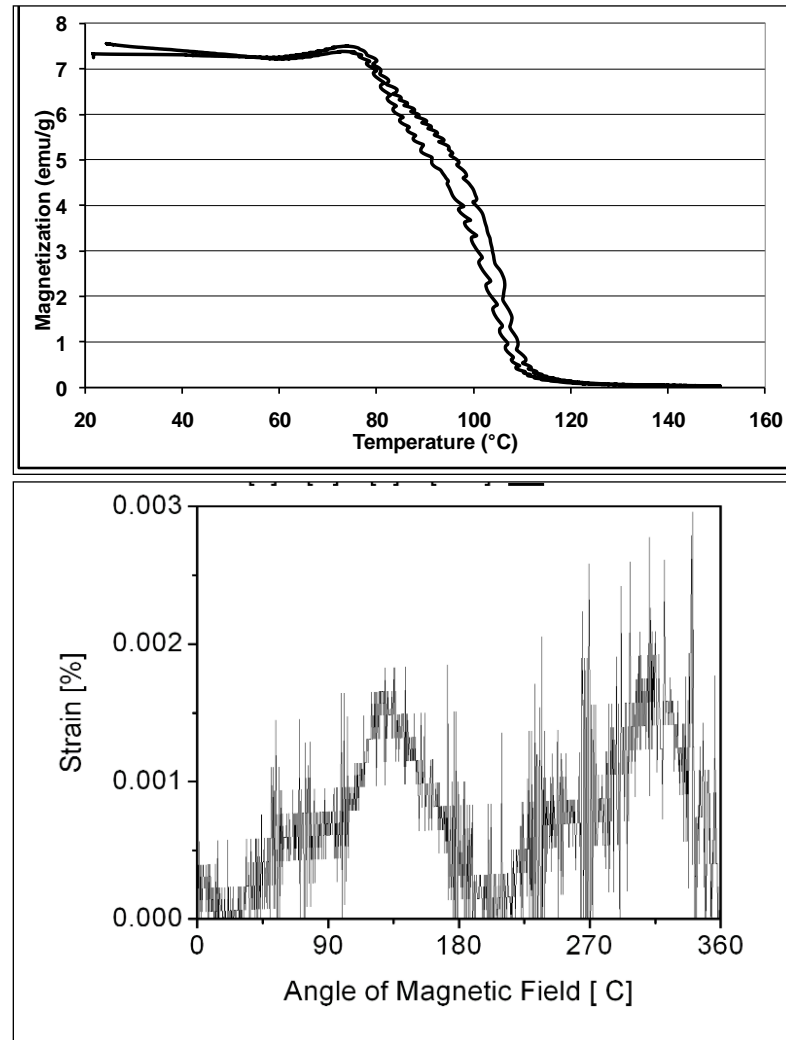
Figure 5.1 Top) Temperature Dependent Magnetization for AR0_D6, Showing the
M_f **at 60 °C and the** A_s **at 62 °C. Bottom) Magneto-Mechanical Cycling of AR0_D6**
where the Maximum MFIS is 0.0015%.
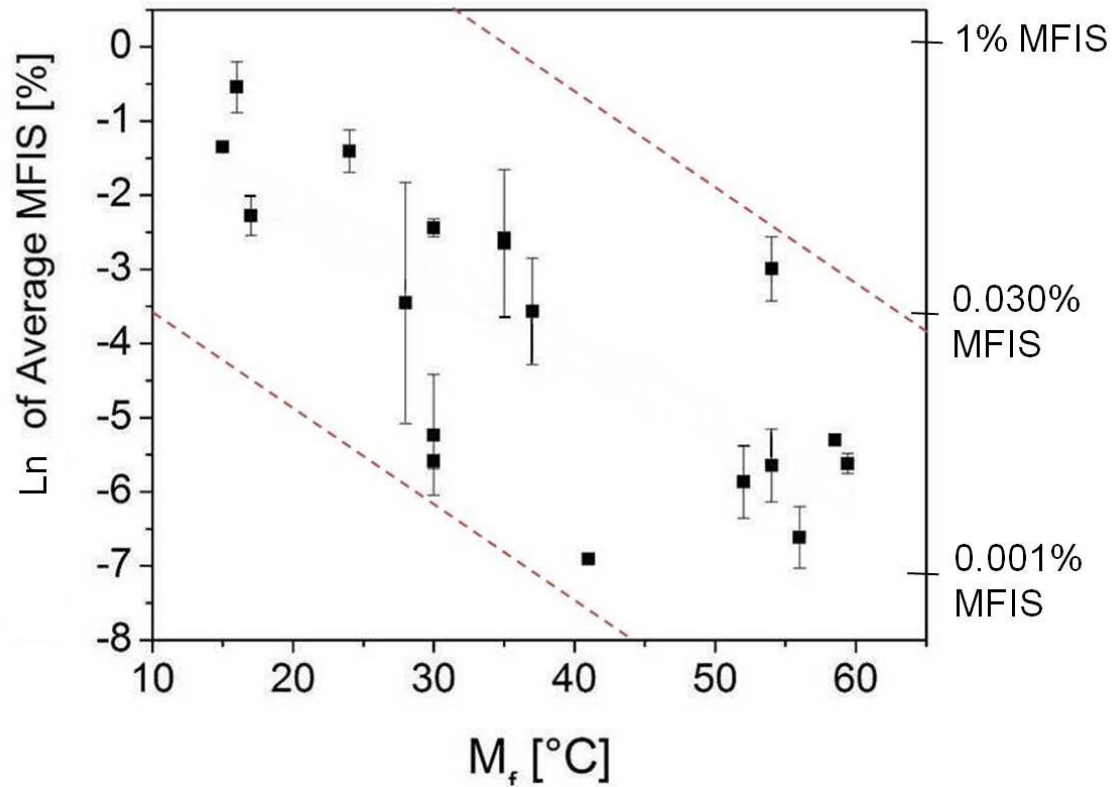
Figure 5.2 Semi-Log Plot of the Average MFIS at Room Temperature Plotted Against the *M_f*. The Error Bars Indicate the Range in MFIS Demonstrated by a Particular Sample. The Red Dashed Lines are a Guide for the Eye that Indicates a Linear Band of Increasing MFIS with Decreasing *M_f*.

5.2 Training Effects on MFIS

5.2.1   Magneto-Mechanical Training

Magneto-mechanical training is marked by increased strain with magneto-mechanical cycling. Of 15 samples that were magneto-mechanically tested, only three samples showed a magneto-mechanical training effect: 7-31, 4-8 H2SO4 and AR20_C11 (see appendix) . Figure 5.3 shows the changes in strain with magneto-mechanical cycling

for 8 samples. The MFIS of sample 7-31, marked with full black circles, increased from

0.725% to 0.800% over 10^5 MMC and then dropped to 0.060%. Samples 8-1_HCL, 4-

23_1, 4-23_2, and 4-23_3 showed consistent strain over the whole range of MMC tested.

Samples 8-1a, 4-8_H2SO4, and 8-1b showed large discontinuities in strain, resulting in a

positive or negative change.
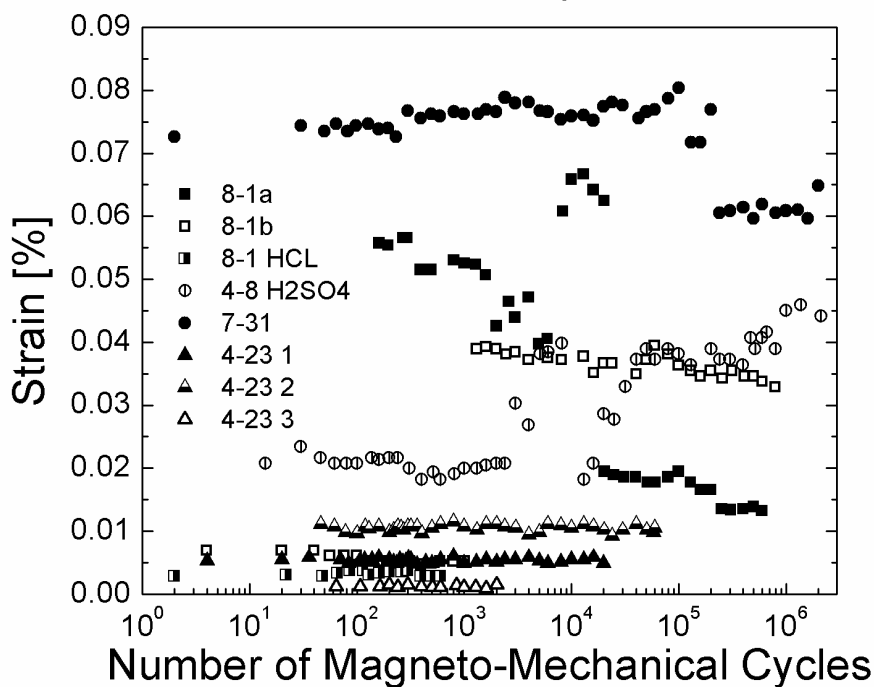
Figure 5.3 Change in MFIS with Magneto-Mechanical Cycling. 8-1a (Black Square) 8-1b (Empty Squares), 8-1HCl (Half Full Squares) are from the Same Foam Rod. 4-8 H2SO4 (Empty Circle), and 7-31 (Black Circles) Singularly Represent a Seperate Foam Rod. 4-23_1 (Black Triangle), 4-23_2 (Half Empty Triangle) and 4-23_3 (Empty Triangles) are from the Same Foam Rod.

5.2.2   Thermo-Magnetic Training

Thermo-magnetic training was applied to 10 samples with varying results. In some cases training increased the MFIS significantly. For sample 4-23_3 the MFIS changed from 0.002% to 0.070% a 34 fold increase in MFIS (Figure 5.4). Both trained and untrained states showed a large maxima when the field is at 110°, 290° from the long axis of the sample. The trained state showed an additional but smaller peak at 0 and 180° with a MFIS of 0.010%.
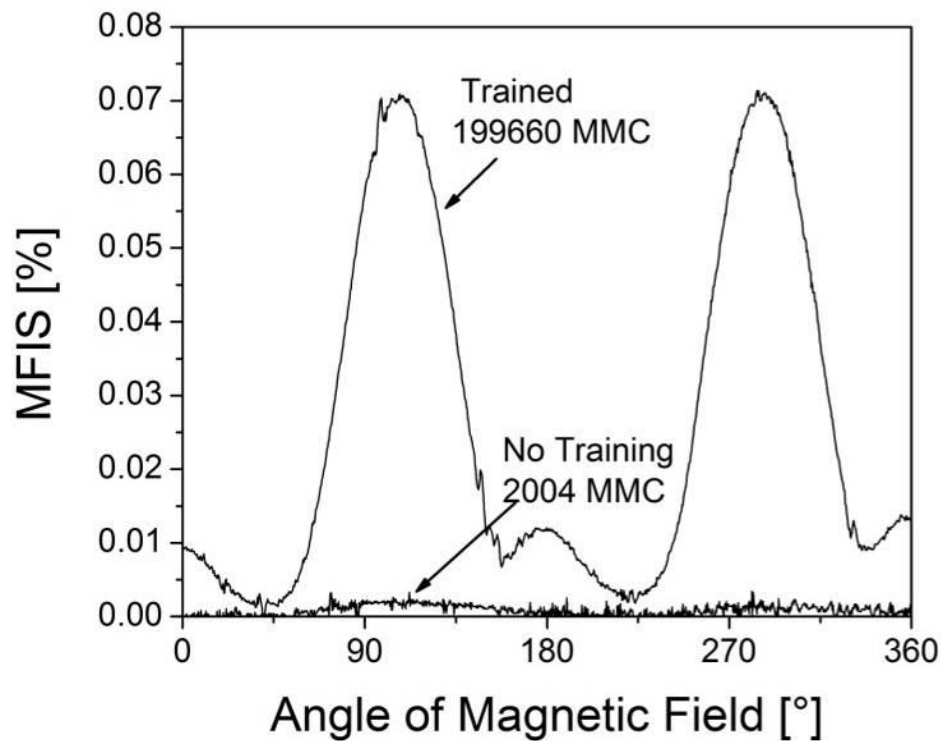
Figure 5.4 Magneto-Mechanical Behavior for Sample 4-23_3 Before and After Thermo-Magnetic Training. After Training a 34 Fold Increase MFIS Occurred. In Addition to the Strain Increase Training Initiated a New Strain Peak at 0 and 180°.

Another sample AR20_C2 showed a threefold increase in MFIS with training from 0.090% to 0.275% strain (Figure 5.5a). The thermo-magnetically trained dual pore foam was then heated above the Curie temperature and cooled without magnetic field to neutralize the training effect. As expected, the MFIS decreased (open triangles Figure 5.5 a), to a value of ~0.027%, which shows a slight decrease beginning at ~1300 MMC to ~0.014% followed by a stable level of MFIS from 0.027 to 0.020% up to ~200,000 MMC. The foam was then trained a second time, without significant increase in MFIS (Figure 5.5a black triangles). Without another neutralization treatment, the sample was trained a third time, leading to a small strain increase to ~0.04% (Figure 5.5 a open circles), remaining near constant over ~151,000 MMC. Figure 5.5 b shows the MFIS magnitude as a function of the magnetic field orientation for a full field rotation for the initial state, after first training, after first neutralization, after second training and after third training. The annealed foam (labeled "Initial" in Fig. 5.5 b) shows a broad strain peak (0.1% MFIS) between -20 ° and 130 ° (and a corresponding peak between 160 ° and 310°) with an asymmetric shape, indicating the presence of multiple sub-peaks (and thus multiple variants). After the first magneto-mechanical training, a single peak (0.28% MFIS) with near-symmetrical shape centered at 90/270 ° is visible, indicating a more homogeneous activation of twinning systems. Neutralization and subsequent trainings did not significantly alter the peak shape and position.
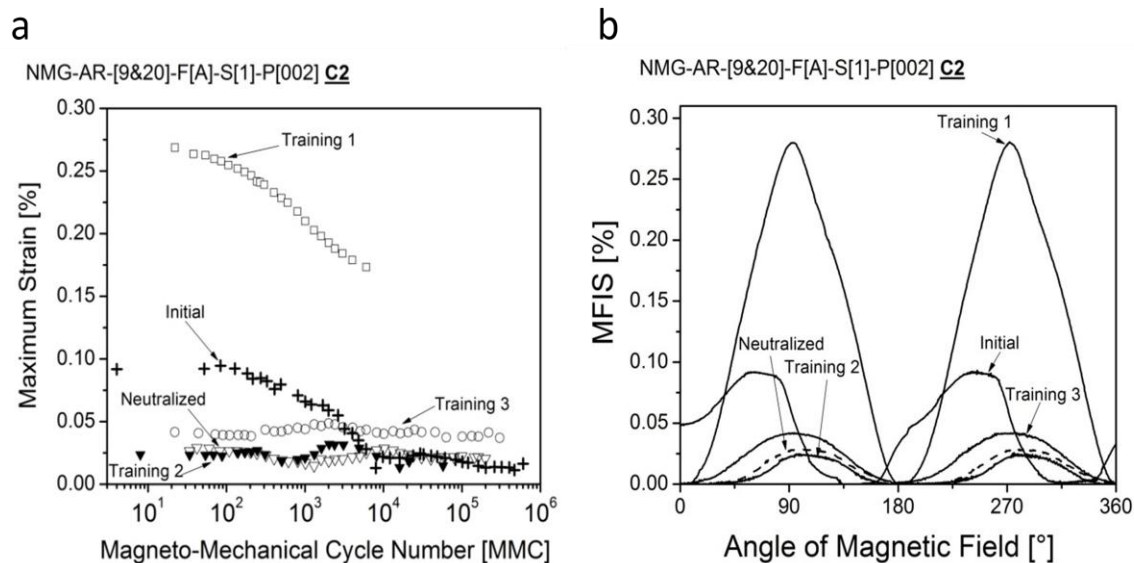
Figure 5.5Change in Magneto-Mechanical Behavior for AR20_C2 at Multiple Trained States. a) MFIS as a Function of Magneto Mechanical Cycle in the Initial State(Crosses), after Thermo-Magnetic Training (Open Circles), with Training Neutralized (Empty Triangles) Followed by a Second (Full Triangles) and Third Thermo-Magnetic Training (Empty Circles). b) MFIS as a Function of Magnetic Field Angle for the Trained States Listed in (a) where the Neutralized State is Represented with a Dashed Curve.

Not all training treatments resulted in an increase in MFIS. For sample AR3_A2 the initial state had 2 peaks per MMC, at 50 and 145 ° with MFIS of 0.095 and 0.130% respectively (Figure 5.6 dashed line). After thermo-magnetic training the MFIS decreased to 0.013 and 0.008% for the maxima at 50 and 145 ° respectively (Figure. 5.6 solid line).
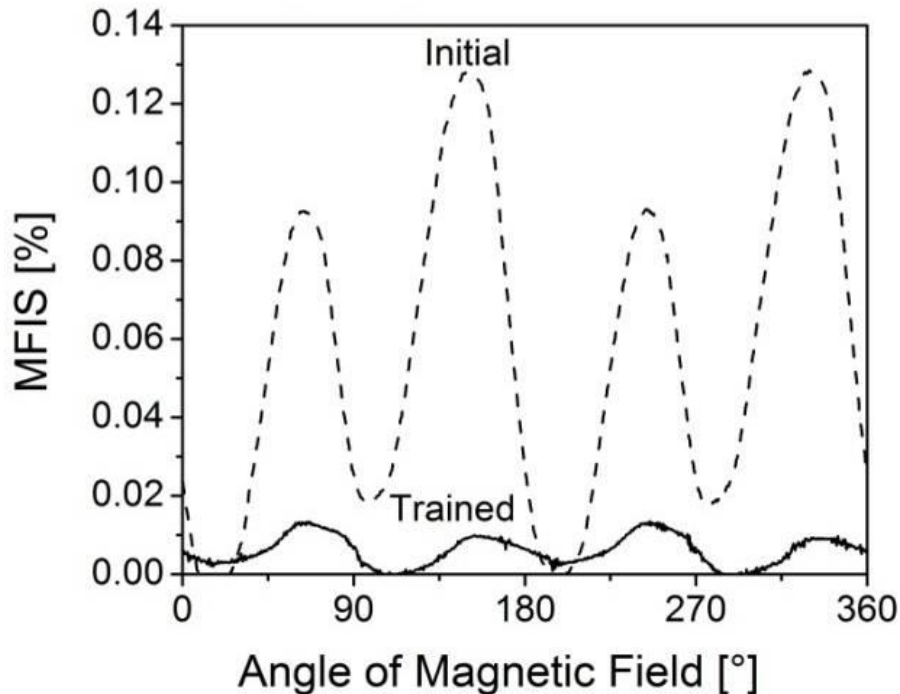
Figure 5.6 Negative Change in Magnetic Field Induced Strain with Thermo-Magnetic Training for Sample NMGF_AR3_A2. The Initial State (Dashed Line) Shows a Higher MFIS than after Thermo-Magnetic Training (Solid Line).

To evaluate the effectiveness of thermo-magnetic training the initial MFIS (black diamond) and the relative change in MFIS (red squares) were plotted on a primary and secondary axis versus the porosity of different samples (Figure 5.7a). The highest initial MFIS were found in the region between 57 and 64% porosity, giving MFIS from 0.095 to 0.500%. After training the samples with the lower initial MFIS showed some of the largest relative change in MFIS, from 2 to 34 fold increases (Figure 5.7b). A 5 fold increase in MFIS was the average relative change in MFIS after thermo-magnetic training.
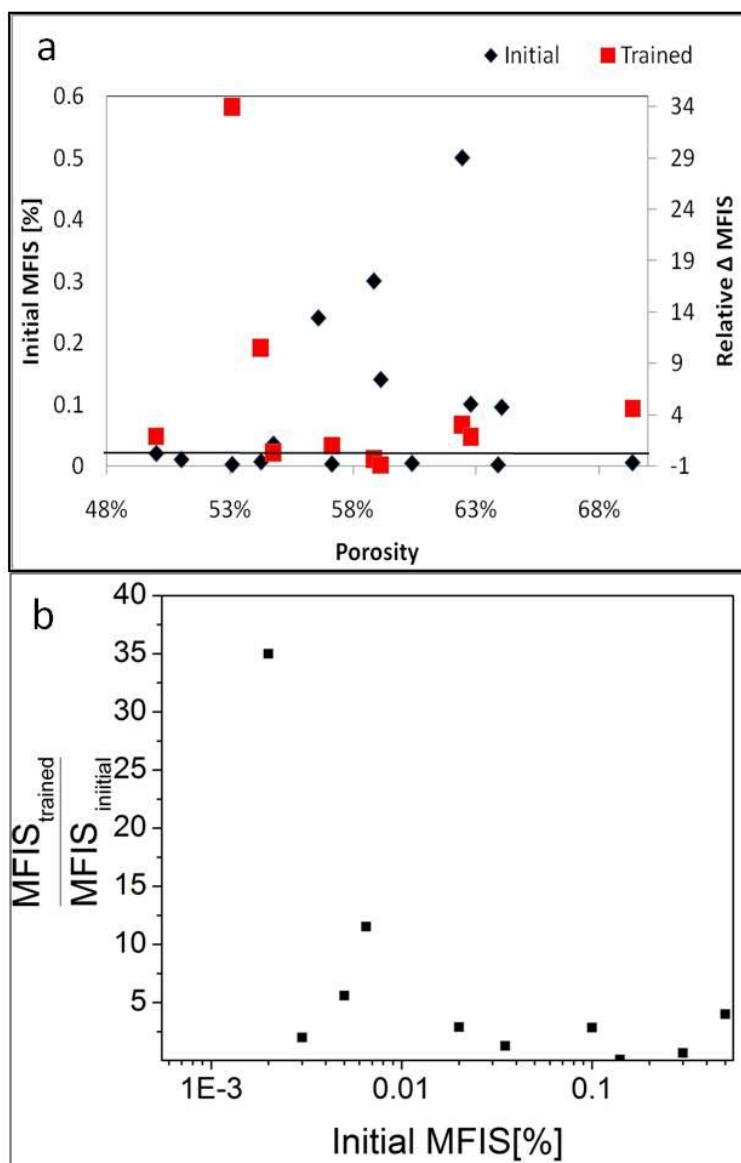
Figure 5.7 Effectiveness of Training for Multiple Samples for a Range of Porosities. a) Initial MFIS (Black) is Plotted on the Primary Axis for Samples of Varying Porosity. The Relative Change in MFIS (Red) is Plotted on the Secondary (Right) Axis for the Samples Represented Initially (Black). The Solid Line Represents a Relative Change of MFIS. b) The Ratio of MFIS after Training to Initial MFIS is Plotted Against the Initial MFIS.

Often training would increase the MFIS, as seen previously, but would also result

maxima shift to ~0 and 180 °. Figure 5.8 shows the change in magneto-mechanical

behavior with thermo-magnetic training for 4-23_1. Initially two peaks per MMC were found at 47 ° and 131 ° with a MFIS of 0.007%. After training the maxima shifted to 69 and 178 ° with MFIS of 0.035% and 0.075% respectively. The maximum shift was seen in 50% of the low porosity ($<$ 54%) samples (see appendix for each sample represented in Figure5.7).
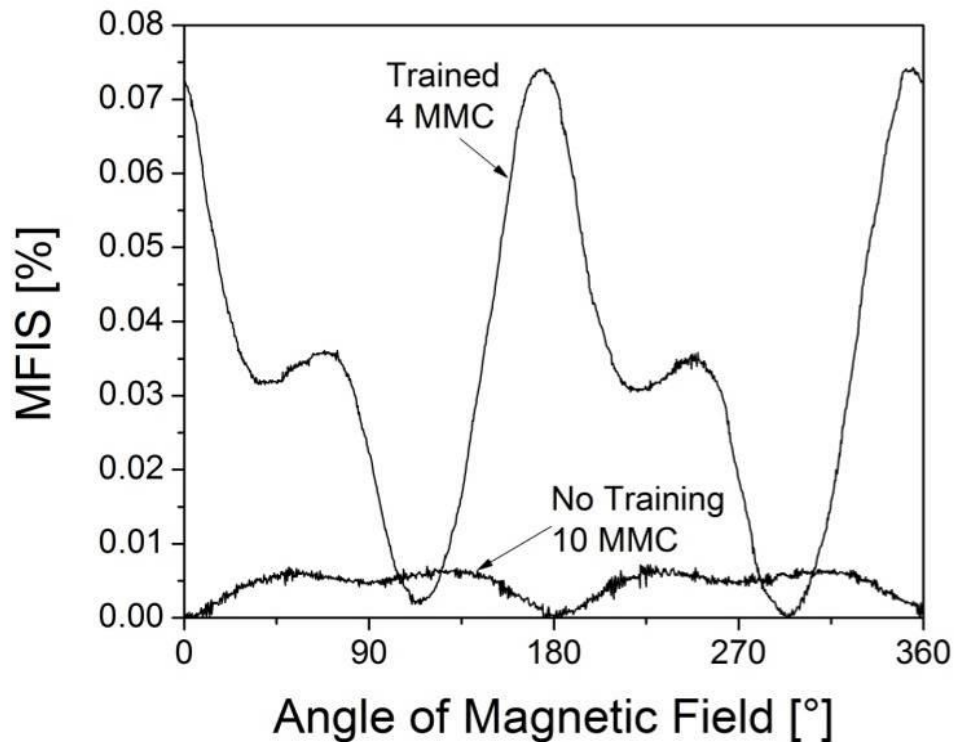
Figure 5.8 Change in Magnetic Field Induced Strain with Thermo-Magnetic Training for Sample 4-23_1. The Trained State Shows a Higher MFIS as well as Strain Maxima Shifts to Angles Not Expected, for Twin Boundary Motion.

The dual peak phenomenon was sometimes induced upon training as observed for AR0_B6 in Figure5.9 (also see 8-1b, 4-23_3, 8-1a in appendix). Initial testing showed one peak per MMC at 75 ° at a MFIS of 0.005%. After thermo-magnetic training for

1MMC the sample displayed two peaks in MFIS. For AR0_B6 one peak was found at 45

° with a MFIS of 0.017% and a second at 130 ° with a MFIS of 0.027%.
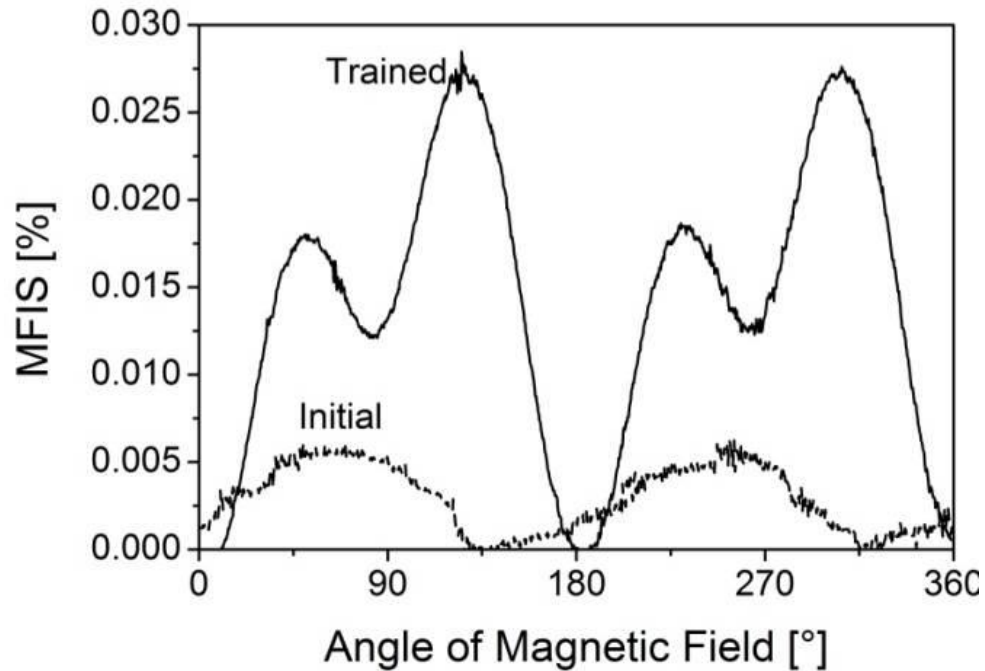
Figure 5.9 Change in Magnetic Field Induced Strain with Thermo-Magnetic Training for Sample AR0_B6. The Thermo-Magnetically Trained State shows a Higher MFIS as well as Two Strain Peaks.

5.2.3   Thermo Magneto-Mechanical Training

In the martensite phase, the foam AR20 C13 exhibited an initial MFIS of 2.1%

shown in Figure 5.9. The MFIS increased over the next 2,000 MMC to 3.4%, stabilizing

at this value up to 15,000 MMC, which decreased to 2.0% up to 75,000 MMC and

remaining stable at this value up to 161,000 MMC (black squares). The foam was then

removed from the sample holder for visual inspection and remounted after its integrity

was confirmed. The subsequent MFIS was below 0.5% (red circles), probably because of

misoriented twins introduced by handling during unmounting and remounting. The foam

was then thermo-magnetically trained. The training returned the high MFIS value that

remained in the range 1.5-1.9% for a further 90,000 MMC (blue triangles).
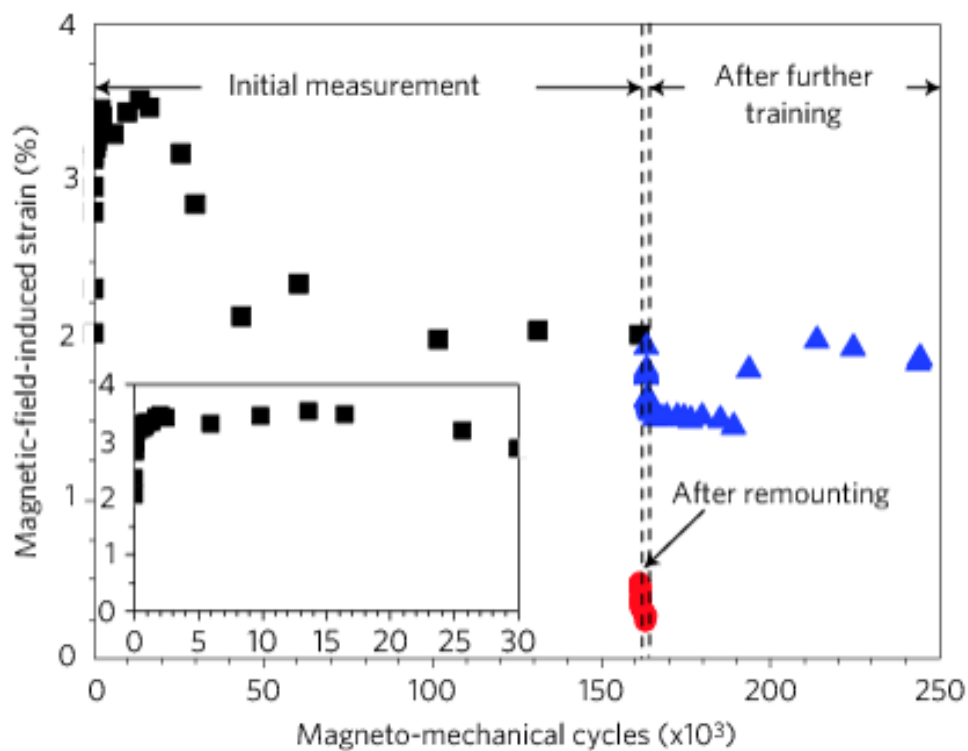
Figure 5.10 MFIS as a Function of Magneto Mechanical Cycle for Sample AR20_C13 in the Initial State (Black Squares), after Remounting (Red Circles), and after Thermo-Magnetic Training (Blue Triangles).[82]

To compare thermo-magnetic with thermo magneto-mechanical training the foam

was thermally cycled between the martensite and austenite states, with the MFIS

measured in situ in a rotating magnetic field. As shown in Figure 5.11, during the first

heating through the phase transformation, the MFIS remains constant at 1.4% in the

martensite phase before dropping rapidly to a near-zero value, over a temperature range

of 35-41°C corresponding to the martensite-austenite transformation. On subsequent

cooling, the MFIS increased sharply between 22 and 23 °C, very close to the M_f

temperature, to a value of 2.2%. At the end of this first Heating/Cooling (H/C cycle), the

temperature rapidly dropped to below -100 °C. As a result, on heating back to room

temperature, the MFIS was strongly reduced to 0.2%. At the end of the second

temperature cycle, however, the MFIS recovered its original value of 2.5%. The MFIS

further increased in the third and fourth temperature cycles, reaching a value of 8.7% at

the end of the fourth cycle.
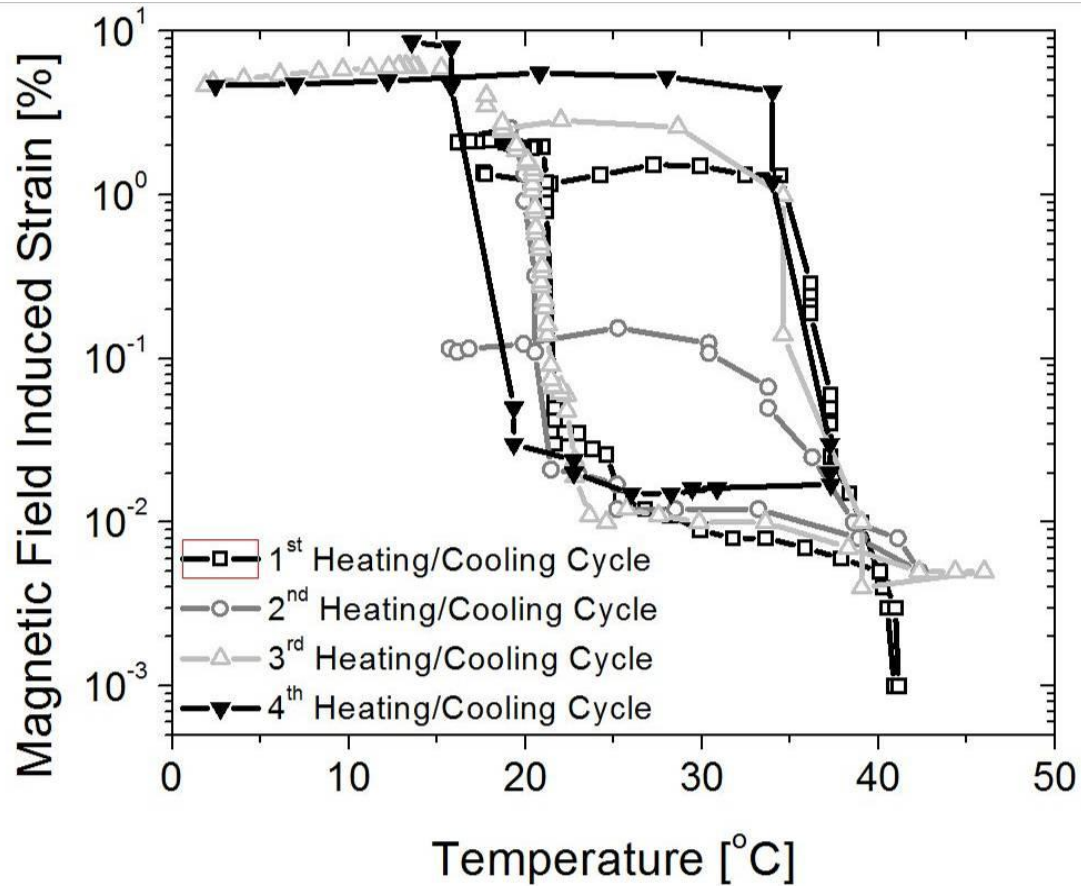
Figure 5.11 Semi Log Plot of Temperature Dependent Magnetic Field Induced Strain from Thermo Magneto-Mechanical Cycling of AR20_C13. The Sample was Heated then Cooled for Four Heating/Cooling (H/C) Cycles where H/C 1 is Marked with Open Black Squares, H/C 2 with Open Circles, H/C 3 with Open Triangles, and H/C 4 with Black Closed Triangles.

5.2.4 Quantifying Training

Texture measurements with X-rays and neutrons were conducted in order to investigate the training phenomenon and quantify the training effect. Texture could be used to observe the shift in volume fractions between different martensite variants, and therefore probe the effectiveness of training. Figure 5.12 shows the polefigures from the pseudo tetragonal 004 planes before and after thermo-magnetic training. It was optically

confirmed that the same area was tested before and after training to ensure the pole

figures were comparable. The polefigures shows 5 Φ and χ orientations of diffracted

intensity (red areas). The different areas of red probably correlate to different grains.

After training there is a noticeable intensity change between 004 poles meaning certain

grains have a higher volume fraction of 004 poles, after training
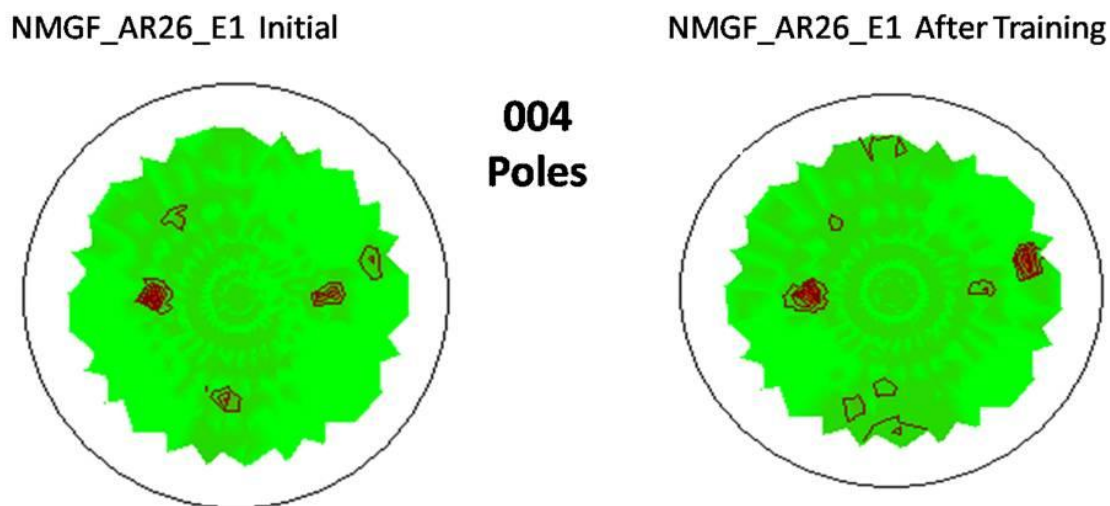
Figure 5.12 Spatial Change in 004 Poles of the 10M Pseudo Tetragonal Cell with Thermo-Magnetic Training for Sample AR26_E1. Red Areas are χ and Φ Orientations of Diffracted Intensity of the (004) Plane. Left is Stereographic Projection of 004 Pole from the YZ Plane of the Sample. Right is the Stereographic Projection of 004 Pole after Thermo-Magnetic Training. Both Pole Figures are from the Same Sample Area.

Neutron diffraction, in which neutrons can permeate the entire sample, shows this

same intensity shift before and after thermo-magnetic training. The pattern was indexed

with the monoclinic 10M cell. The training effect is shown by the change in relative peak

intensities. For example after training the 0,2,0 peak reduces to 25% of the 1,0,5 peak, as well as the decrease of the 2,1,5 and 1,1,10 peaks to near 0 intensity (Figure 5.13).

Run# 4238; Peter NiMnGa foam 1T0deg −30deg 0C   150−ALL
Bank no. = 1 Two−theta =   144.45   Observed Profile

Before Training

105

202

200,
0010

020

103

1110

2010 215   12-3

Norm count/musec.

D-spacing, A

Run# 4253; Peter NiMnGa foam 1T0Hdeg+20deg 0C   150−ALL
Bank no. = 1 Two−theta =   144.45   Observed Profile

After Training

Cu
contaminant

0210

Norm count/musec.

D-spacing, A
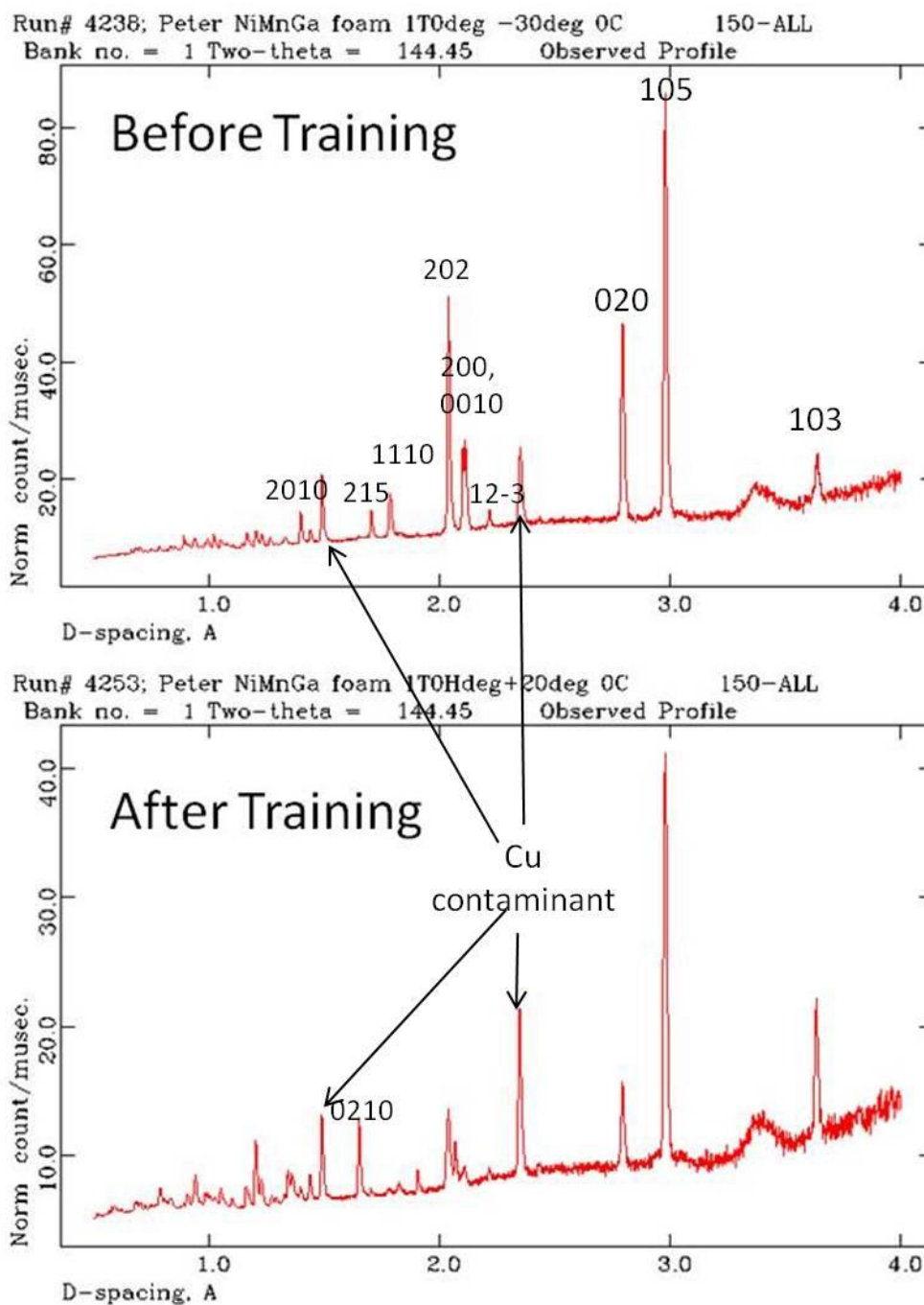
Figure 5.13 Neutron Back Scattered Diffraction Before and After Thermo-Magnetic Training. Patterns from Four Sample Orientations were Added and Integrated. The 10M Monoclinc Cell was Used to Index the Diffraction Pattern.

5.3 Pore Architecture Effect on MFIS

Figure 5.14 shows the twin microstructure within one single pore foam (Figure 5.14a) and dual pore foam (Figure 5.14 b) strut. In the single pore foam struts are much larger and show multiple twin arrangements most of which do not fully span the struts. Though the grain boundaries were not etched, the twin terminating in certain areas indicated grain boundaries may exist in the struts of the single pore foam. The dual pore foam have much smaller struts due to the addition of small pores and twins fully span the width of the dual pore foam strut (Figure 5.14b).
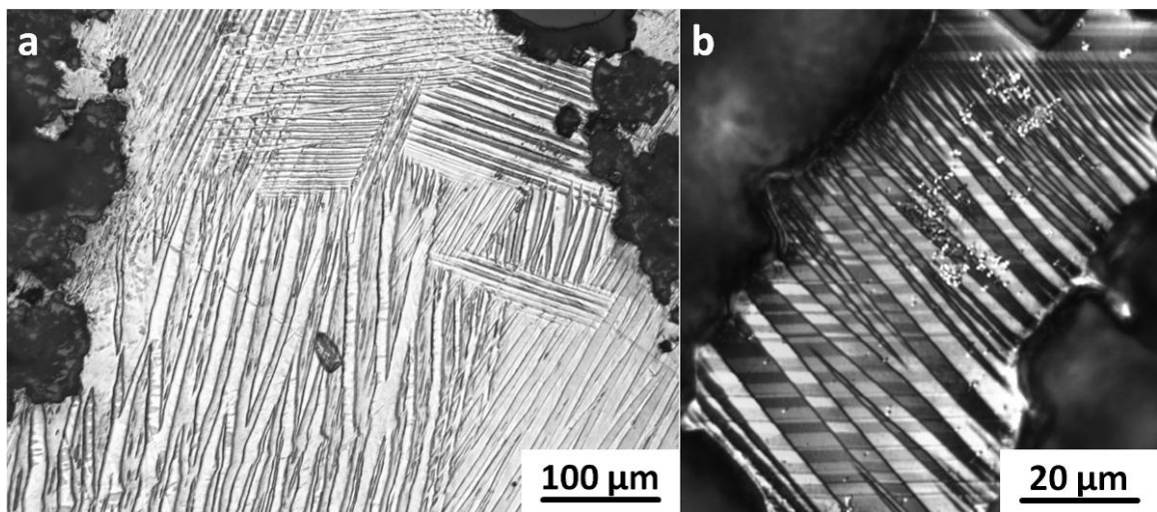
Figure 5.14 Optical Micrographs of Twin Microstructures in a) Single Pore Foam and b) Dual Pore Foam. Thanks to Y. Boonyongmaneerat and X.X. Zhang for Images. [83-85]

Figure 5.15a is a plot of MFIS vs. magneto-mechanical cycles (MMC), of the single-pore foam AR26_E1 after annealing. The MFIS decreases from 0.24% at cycle 78% to 0.18% at cycle 506, then remained stable at 0.18–0.19% until cycle 20,378. Figure 5.15b shows plots of MFIS vs. magnetic field orientation for cycles 68 and 20,378

for the same single-pore foam. In the first MMC (0–180°), two strain peaks appear at 60 and 115 °, with respective MFISs of 0.20% and 0.24% for 68 MMC. In the second MMC (181–360 °), the same peaks occur at 240 and 300 °, as expected. As shown in Figure 5.15b, the heights of these peaks are reduced to 0.16% and 0.18% for cycle 20,378. The peak shapes after 20,378 MMC are unchanged, except for a small shoulder at 105 ° within the second ~135/315 ° peak.
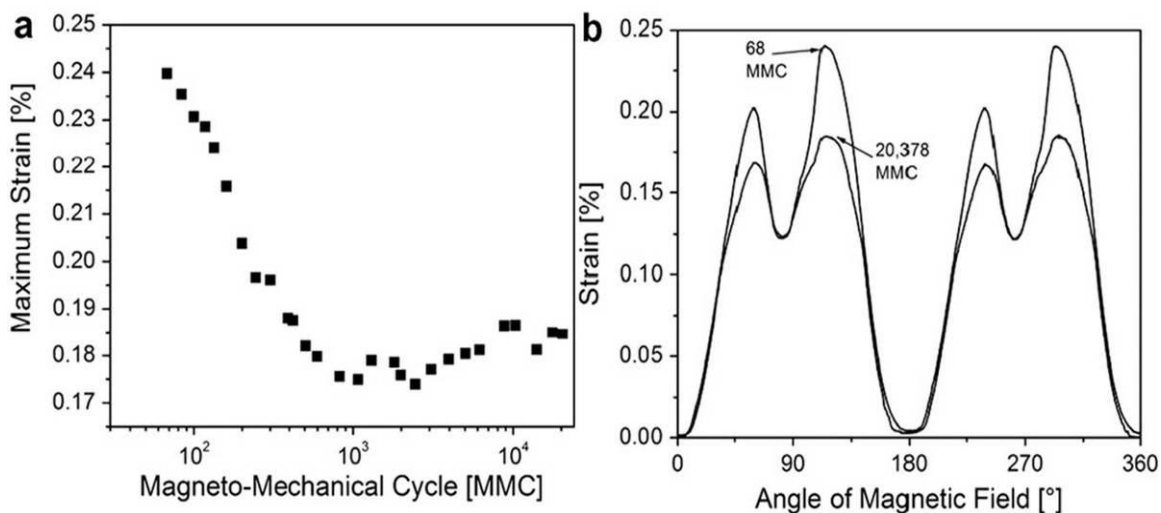
Figure 5.15 Magneto-Mechanical Behavior of Single Pore Foam AR26_E1. a) Magneto-Mechanical Cycle Dependent MFIS. b) Magnetic Field Orientation Dependent MFIS for MMC 68 and 20,378.

Figure 5.16 depicts the MFIS of the dual-pore foam AR20_C2 and is equivalent to Figure 5.15a for the single pore foam. The magnetic field orientation dependent MFIS for AR20_C2 is discussed in section 5.2.2. Direct comparison is however hampered by the different porosities. Figure 5.16 shows plots of MFIS vs. MMC number before (open

squares) and after thermo-magnetic training (black squares). When tested in the initial

annealed state, the foam shows a strain of 0.10%, decaying to 0.014% after 60,000 MMC

and remaining at this value for up to ~300,000 MMC. After subsequent thermo-magnetic

training, the foam showed a notable increase in MFIS to 0.28% for MMC 4, again

decaying to 0.17% after 6000 MMC.
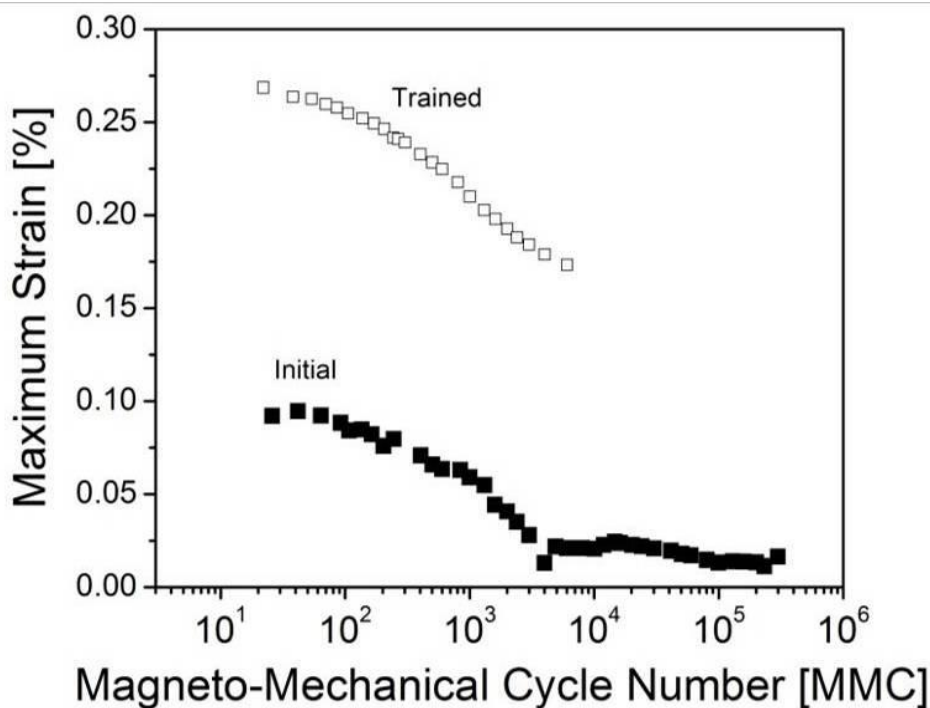
Figure 5.16 Magneto-Mechanical Cycle Dependent MFIS of Dual Pore Foam AR20_C2 Before (Black Squares) and After (Open Squares) Thermo-Magnetic Training.

In the semi-logarithmic plots of Figure 5.15a and Figure 5.16 the rate of MFIS

decrease is roughly linear up to ~500 and 6000 MMC in single pore and dual pore foams,

respectively. The rate of strain decrease between 100 and 6000 MMC is ~0.040 and

0.050 % MFIS/MMC for the dual-pore foam in both annealed and trained states, respectively. This is lower than the value of ~0.069 %MFIS/MMC for the single-pore foam.

5.4 Porosity Effect on MFIS

A porosity study was conducted to confirm the hypothesis that porosity was the reason for enhanced MFIS of Polycrystals. Three dual pore samples AR56_I2_S2, AR56_I2_S1, AR59_G2_S1 were systematically tested for MFIS followed by a porosity increase for multiple etching steps. This systematic study allowed for observation of the effect of porosity on MFIS without convolution of variables.

Phase transformations of all three samples are listed in Table 5.1. The three sample show transformations that are within 5 °C of each other. This table also shows the martensite finish is below room temperature and the samples therefore needed to be cooled below room temperature to be fully martensitic.

Table 5.1 Phase Transformation Temperatures of Ni-Mn-Ga Foams Tested in the Porosity Study.

	M_s [°C]	M_f [°C]	A_s [°C]	A_f [°C]	*Curie* [°C]
I2_S1	27	14	22	37	99
I2_S2	24	22	20	33	90
G2_S1	26	12	22	35	95

Table 5.2 lists the compositions of the three samples in the porosity study. Deviations from the parent ingot target composition, with the measured compositions are within experimental error of each other. The composition was checked for each etching step of one sample, to ensure there was no preferred dissolution of one element. EDS confirmed that they chemical composition remained constant with each etching step. Therefore, no chemical compositional changes occurred through the course of etching and TMC.

Table 5.2 Compositions of Foam Samples Compared to the Parent Ingot Target Composition.

Sample	Ni at%	Mn at%	Ga at%
Nominal Parent Ingot Composition	52.0	24.3	23.7
I2-S1	51.7±2.6	24.5±1.3	23.7±2.8
I2-S2	51.6±1.8	24.9±0.8	23.4±1.8
G2-S1	50.7±1.8	24.8±1.1	24.4±0.6

Anisotropy was measured for the foam sample to address the presence of crystallographic texture. Table 3 shows the anisotropy of the three samples which are corrected for shape anisotropy. The anisotropy energies of I2-S1 and G2-S1 was a little less than 40 kJ/m^3, which is about 20% of the magneto crystalline anisotropy energy of a single crystal [50]. The anisotropy energy of sample I2-S2 was 10.5 kJ/m^3, which is only about 5% of the magneto crystalline anisotropy energy of a single crystal. The amount of anisotropy can be used to infer the degree of preferred orientation throughout the grains, though a crystallographic texture analysis is not presented here.

Table 5.3 Magneto Crystalline Anisotropy Energy of Ni-Mn-Ga Foams used in the Porosity Study.

Sample	Anisotropy (kJ/m^3)
I2-S1	39.1
I2-S2	10.5
G2-S1	37.1

Figure 5.17 shows the maximum MFIS as a function of porosity. The maximum strain was obtained from thermo magneto-mechanical cycling and plotted against the porosity. G2-S1 showed a ten-fold increase in MFIS from 0.12% to 1.26% with an increase in porosity from 71% to 72.3% respectively (Figure 5.17 red circles). The MFIS for I2-S1 showed a MFIS of 0.26% at a porosity of 48.5 which increased to 0.27% when the porosity was increased to 52.3%. The MFIS further increased to 0.29% when the porosity was increased to 56.8% (Figure 5.17 blue triangles). I2-S1 did not display a clear martensite-austenite phase transformation hysteresis and training affect therefore to fully represent the maximum MFIS, multiple cooling curves were averaged and the error bars on Figure 5.17 represent the standard deviation of the averaged maximum MFIS. I2-S2 initially showed a MFIS of 0.09% at a porosity of 54%, after etching to a 56.4% porosity the MFIS increased to 0.36%. Further etching of I2-S2 to a porosity of 58.2% showed a strain of 0.35% a small decrease, but after etching even further to 60.3% porosity the MFIS again increased to 0.613% (Figure 5.17 black squares). The lowest porosity shown in Figure 5.17 is the considered the initial porosity, and was the first time the MFIS was measured for this sample.
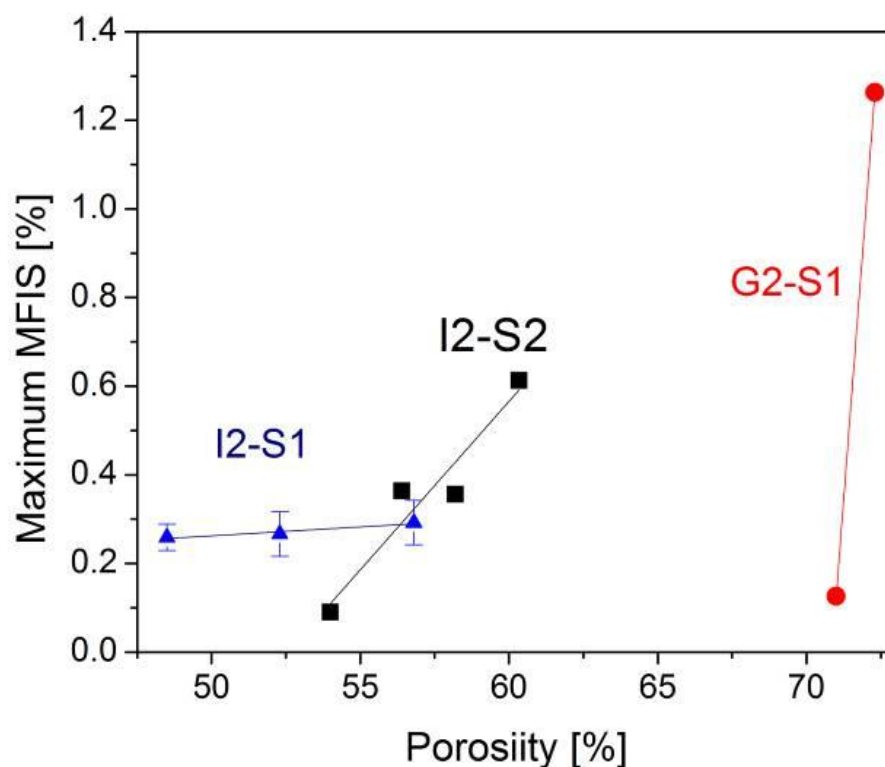
Figure 5.17 The Effect of Porosity Increase on the Maximum Level of MFIS for Ni-Mn-Ga Foams: I2-S1 (Triangle), I2-S2(Squares), G2-S1(Circles). The Error Bars on I2_S1 Indicated the Standard Deviations from Averaging the Maximum MFIS from Multiple Thermal Cycles. Each Sample Showed and Increasing MFIS with Increasing Porosity.

Figure 5.18 a and b show the result of TMC for G2-S1 before and after etching. Figure 5.18 a, is the initial TMC for G2_S1. The maximum MFIS is 0.12% and decreases to 0.01% when heated to 50 °C. No clear martensitic phase transformation is observed in the temperature regime probed. With an increase of only 1.3% porosity the MFIS increased 10 fold to 1.25%. After the porosity increased the martensitic phase transformation hysteresis was clearly visible, (Figure 5.18 b) where arrows mark the

direction of the temperature change. The MFIS decreased upon heating as the martensite to austenite transformation happened from 27 to 36 °C. Upon cooling the phase transformation from austenite to martensite occurred from 22 to 11 °C. For the first heating and cooling cycle (H/C) (Figure 5.18 black squares) the MFIS was 0.58% at -10 °C and decreased to 0.27% at 27 °C when the martensite to austenite transformation occurred. The MFIS was near 0% up to 22 °C when the reverse transformation occurred, after which the MFIS followed the same path of strain increase up to 0.58% upon cooling. Subsequent heating cooling cycles (H/C 2-4) showed a very flat region of MFIS while heating (from -10 to 30 °C). However on cooling the MFIS increased past the intersection of the heating curve up to a maximum MFIS at ~10 °C followed by a decay in MFIS. For example H/C 2 showed a MFIS of 0.45% from -5 °C to 30 °C until the martensite to austenite transformation, and upon cooling the MFIS was near zero down to 22 °C when the MFIS increased to 0.84% at 10 °C followed by a decrease in MFIS to 0.55% at -10 °C. For H/C 2-4 in the martensitic state the MFIS vs temperature paths are not the same for both heating and cooling as seen for H/C 1. Repeated TMC resulted in an increase of MFIS from one H/C cycle to the next. The maximum MFIS was 0.62% for H/C 1 and reached 1.25% for H/C 4. After the second etching step the sample could no longer be tested because the sample developed a large cavity making handling difficult. SEM micrographs were taken after the last magneto-mechanical testing (Figure 5.18 c). The micrograph shows severe cracking accompanied by the displacement of crack surfaces.
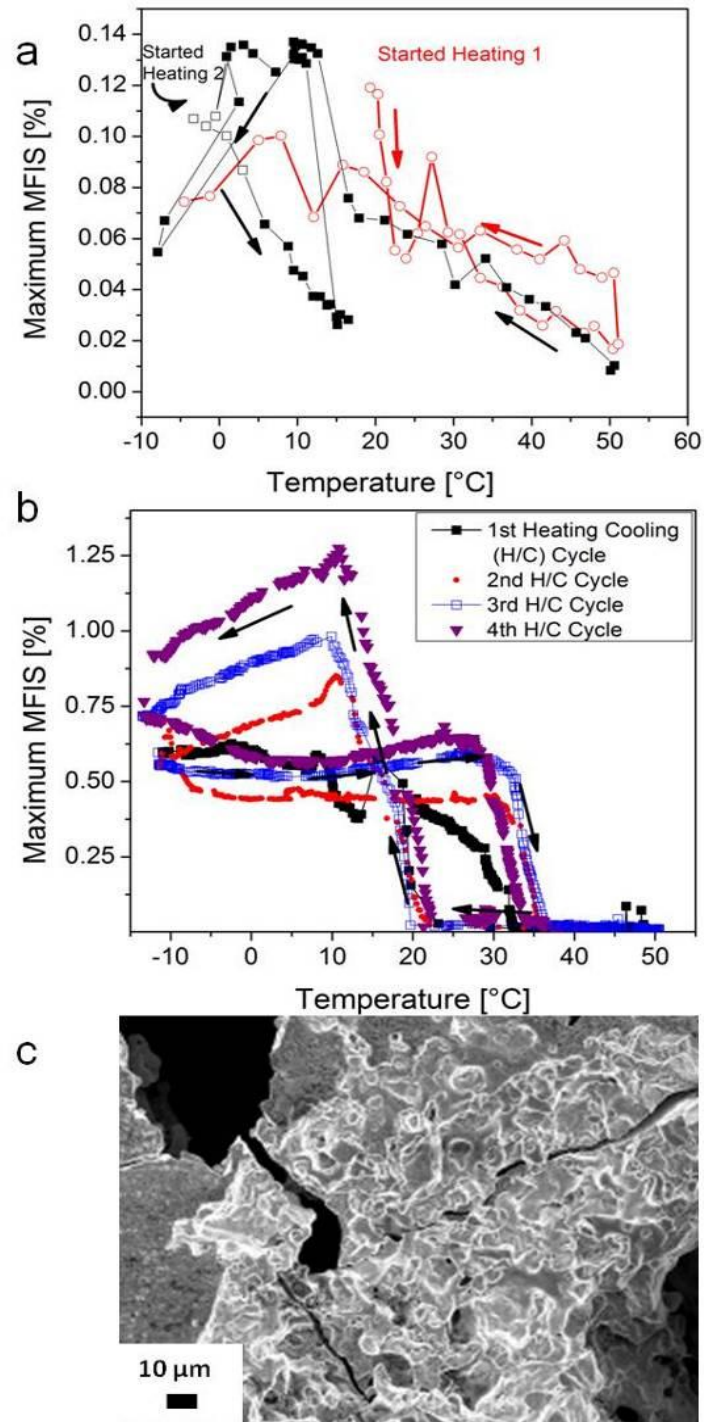
Figure 5.18 Maximum Magnetic Field Induced Strain vs Temperature for G2-S1 at a)71.0%Porosity b)72.3% Porosity, and c) SEM Micrographs of G2-S1 at 72.3% Porosity after TMC Showing Extensive Cracking. For a and b the Multiple Curves Represent Successive Heating Cooling (H/C) Cycles.

I2-S2 also showed an increase in MFIS over multiple etching steps. Figure 5.19 shows one TMC for three different porosities. The maximum MFIS increased with each porosity increase. For a porosity of 54.4% (Figure 5.19 black squares) the MFIS increased upon heating to 0.08% at 13 °C until the martensite to austenite transition from 13°C to 40 °C. Subsequent cooling of I2-S2 at 54.8% porosity showed near zero MFIS down to about 4 °C when the austenite to martensite transformation occurred. At a porosity of 56.6% (Figure 5.19 red circles) while heated the MFIS gradually increased from 0.25% at -15 °C to 0.35% at 27 °C, after which the martensite to austenite transformation occurred. Interestingly the MFIS (red circles), drops to near zero from 27 to 29 °C follow by a sharp increase in MFIS to 0.24% at 30.5 °C ensued by a drop in MFIS over the next 3 degrees. The spike in MFIS was also seen upon cooling at 18 °C when the MFIS suddenly increased to 0.16% followed by an subsequent decrease in MFIS. Upon further cooling the MFIS increased to 0.25% at -20 °C. At a porosity of 60.3% (Figure 5.19 blue triangles), the MFIS vs temperature behavior was similar to that seen in Figure 5.18b , while heated, the MFIS was consistently at 0.40% up to 22 °C when the martensite to austenite transformation occurred. Similar to the TMC for 56.6% porosity a sharp peak in MFIS occurred at 33 °C fallowed by zero MFIS at 35 °C. When I2_S2, was cooled the MFIS was near zero until 16 °C when the austenite to martensite transformation occurred, which was followed by at peak and decay in MFIS at 11 °C. Upon further cooling the MFIS increased past the intersection of the heating curve at 3 °C at which IS_S2 was fully martensitic and displayed a MFIS of 0.61%.
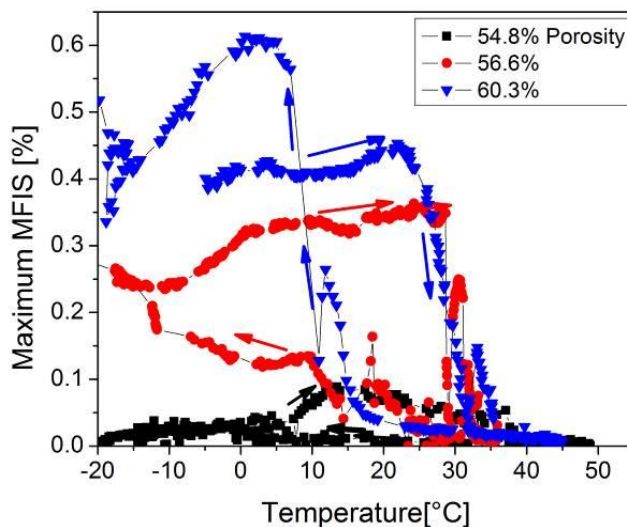
Figure 5.19 One Thermal Cycle of Maximum Magnetic Field Induced Strain vs Temperature Curve for I2-S2 at Different Porosities. Full Squares are the 2nd H/C Cycle for 54.8% Porosity, Full Circles are the 2nd H/C Cycle for 56.6% Porosity and the Triangles are 3rd H/C Cycle for I2-S2 at 60.3% Porosity. Arrows Indicate Direction of Temperature Increase.

5.5 Pore Distribution Effects on MFIS

Three samples AR49_F2_S1, AR49_F2_S2, AR49_F2_S3 from the same foam rod, with compositions within experimental error of each other and very similar phase transformation were tested for MFIS by thermo magneto-mechanically cycling (TMC), anisotropy and pore distribution. Pore distribution was analyzed by X-ray Tomography at HBZ in Berlin Germany by Dr. Markus Chmielus.

Temperature dependent magnetization measurements were conducted in which the martensitic phase transformation and Curie temperature were found. Table 5.4 shows that the phase transformation of the three sample were very close, within ± 3 °C of each other. The Curie temperatures of the three samples were within ± 5 °C of each other.

Table 5.4 Phase Transformation Temperatures of F2_S1, F2_S2, and F2_S3 Samples that were Used in the Pore Distribution Study.

Sample	A_s [°C]	A_f [°C]	M_s [°C]	M_f [°C]	Curie [°C]
AR49_F2_S1	26	31	25	17	91
AR49_F2_S2	25	31	24	16	100
AR49_F2_S3	23	36	24	15	105

Upon initial magneto-mechanical cycling of the dual pore foams, AR49_F2_S1, AR9_F2_S2, and AR49_F2_S3 showed a maximum MFIS of 0.124%, 0.750%, and 0.270% respectively. AR49_F2_S1 showed an initial MFIS of 0.124% that tapered off to 0.084% over 10^5 MMC (Figure 5.20a). AR49_F2_S2 showed an initial MFIS of 0.605% that declined to 0.495% at 10^5 MMC (Figure 5.20b). AR49_F2_S2 was then left in the testing apparatus overnight. Testing AR49_F2_S2 the next day revealed an increase in MFIS to 0.625% which increased further upon cycling to 0.750% at 115,000 MMC. AR49_F2_S3 showed an initial MFIS of 0.251%, which increased to 0.270 at 10^4 MMC. After 10^4 MMC the MFIS decreased to 0.252% at 120,000 MMC (Figure 5.20c).
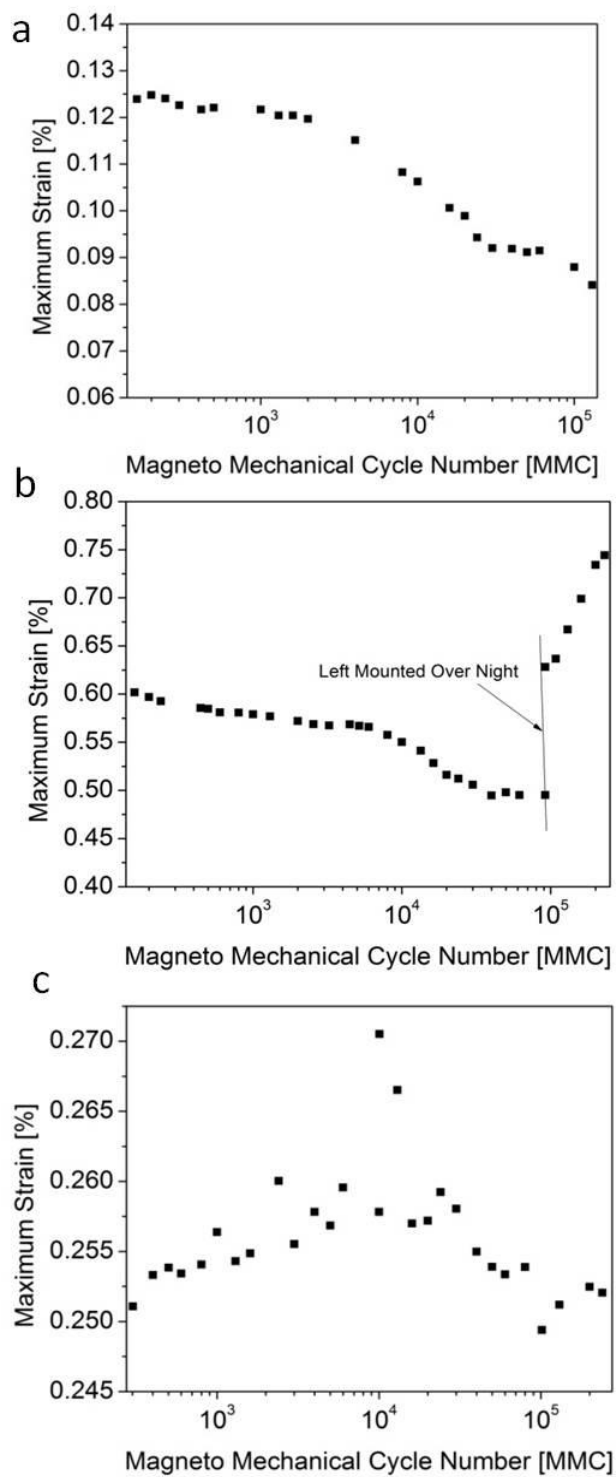
Figure 5.20 Magneto-Mechanical Cycle Dependent MFIS for a)AR49_F2_S1 b) AR49_F2_S2 and c) AR49_F2_S3 at a Constant Operating Temperature.

Since the M_f was below room temperature TMC was conducted to test for MFIS in a fully martensitic state. For AR49_F2_S1 (Figure 5.21) initially the MFIS started at 0.17% and upon heating the MFIS gradually decreased to 0.13% at 27 °C after which the MFIS sharply decreased to 0.07% at 30 °C the MFIS continued to decrease to 0.02% at 45 °C. The MFIS continued to gradually rise to 0.07% at 25 °C after which the MFIS increased sharply to 0.25% at 18 °C which was followed by a sharp decrease in MFIS. Each H/C cycle exhibited similar behaviors in MFIS indicating very little thermo magneto-mechanical training occurred during TMC.
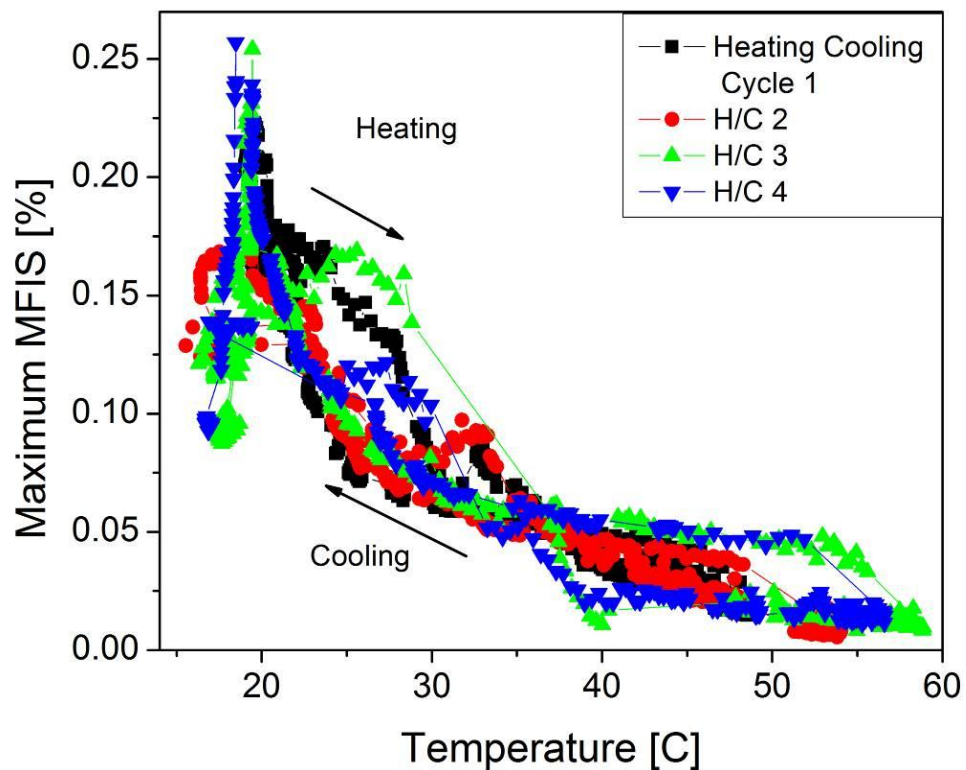
Figure 5.21 Temperature Dependent Magnetic Field Induced Strain from Thermo Magneto-Mechanical Cycling of AR49_F2_S1. The Sample was Heated then Cooled for Four Heating/Cooling (H/C) Cycles where H/C 1 is Marked with Black Squares, H/C 2 with Red Circles, H/C 3 with Green Triangles, and H/C 4 with Blue Triangles.

For AR49_F2_S2 very different MFIS resulted from TMC as compared to TMC

for AR49_F2_S1 (Figure 5.22). For H/C 1 (black squares) the MFIS started at 1.1% and

was constant up to where the martensite to austenite transformation occurred from 27 °C

to 34 °C. On cooling the MFIS was minimal until the austenite to martensite

transformation from 25 °C to 16 °C. The MFIS increased past the heating curve to 1.32%

at 15 °C which is the start of the MFIS of H/C 2 (red squares). For H/C 2 and 3 the phase

transformation behavior was similar to the first only with a distinct spike in MFIS during

austenite to martensite phase transformation at about 32 °C. On H/C 3 the MFIS

increases slightly to 1.5% before the martensite to austenite phase transformation at 27

°C.
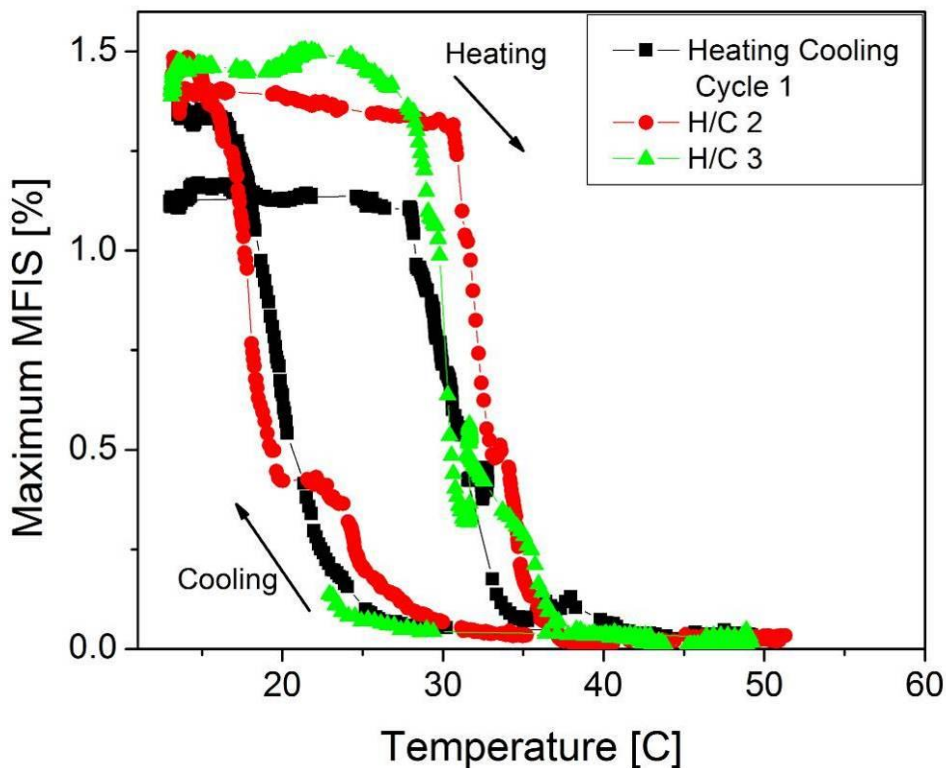
Figure 5.22 Temperature Dependent Magnetic Field Induced Strain from Thermo Magneto-Mechanical Cycling of AR49_F2_S2. The Sample was Heated then Cooled for Three Heating/Cooling (H/C) Cycles where H/C 1 is Marked with Black Squares, H/C 2 with Red Circles, and H/C 3 with Green Triangles.

During TMC of AR49_F2_S3 the sample was first cooled then heated (Figure 5.23). On the first cooling (black squares), the MFIS starts at 0.70% at 15 °C which decreased to 0.35% at 5 °C. Upon heating the MFIS displays a constant MFIS of 0.36% up to 20 °C where there was a marked increase in MFIS. Upon heating, the martensite to austenite transformation occurred from 27 to 31°C resulting in a decrease in MFIS. At 30 °C the MFIS gradually increased to 0.15% down to 20 °C. A peak of 0.5% and decay of MFIS to 0.35% occurred at 17 °C. Further cooling showed a 0.35% MFIS which was

stable down to -5 °C. C/H 3, (green triangles) showed a similar transformation behavior to C/H 2.
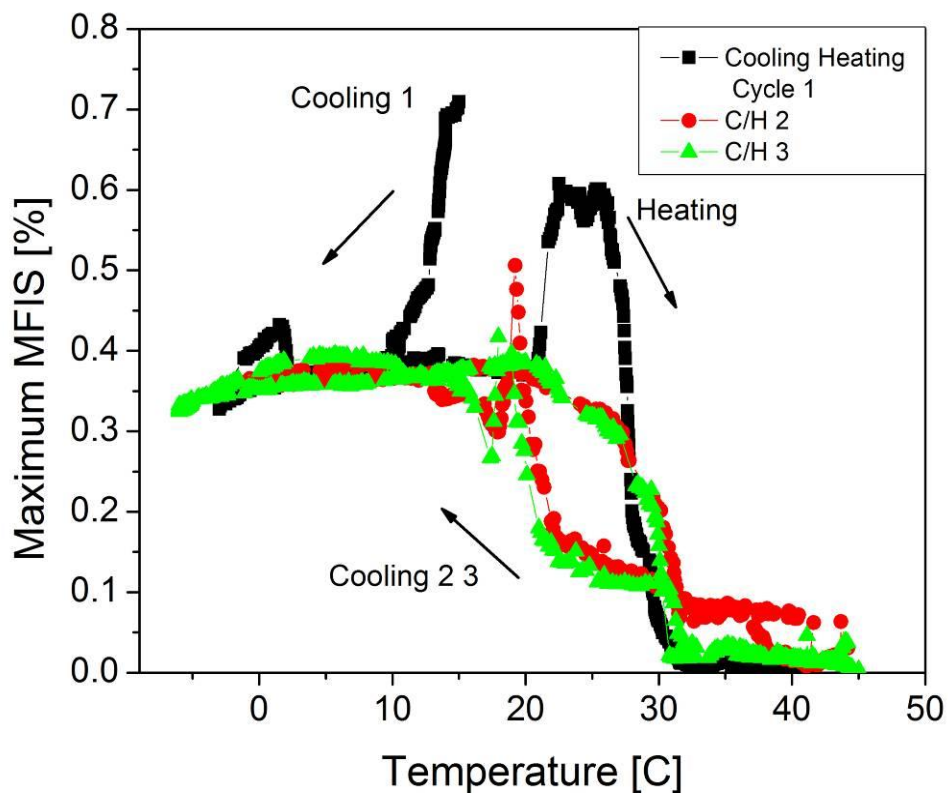
Figure 5.23 Temperature Dependent Magnetic Field Induced Strain from Thermo Magneto-Mechanical Cycling of AR49_F2_S3. The Sample was Heated then Cooled for Three Cooling/Heating (C/H) Cycles where C/H 1 is Marked with Black Squares, C/H 2 with Red Circles, and C/H 3 with Green Triangles.

Field orientation dependent and field strength dependent magnetization measurements were done to test for magneto crystalline anisotropy. The field orientation dependent magnetization measurements revealed the magnetic field angles that resulted in a minimum and maximum of magnetization. The relative change in magnetization during the field rotation is an indicator of the degree of anisotropy. Figure 5.24 shows the

resulting field orientation magnetization measurements of AR49_F2_S1(black), F2_S2

(red), and F2_S3(blue). AR49_F2_S1, AR49_F2_S2 and AR49_F2_S3 showed a 19.7%,

68%, and17% relative change in magnetization respectively during the field rotation.
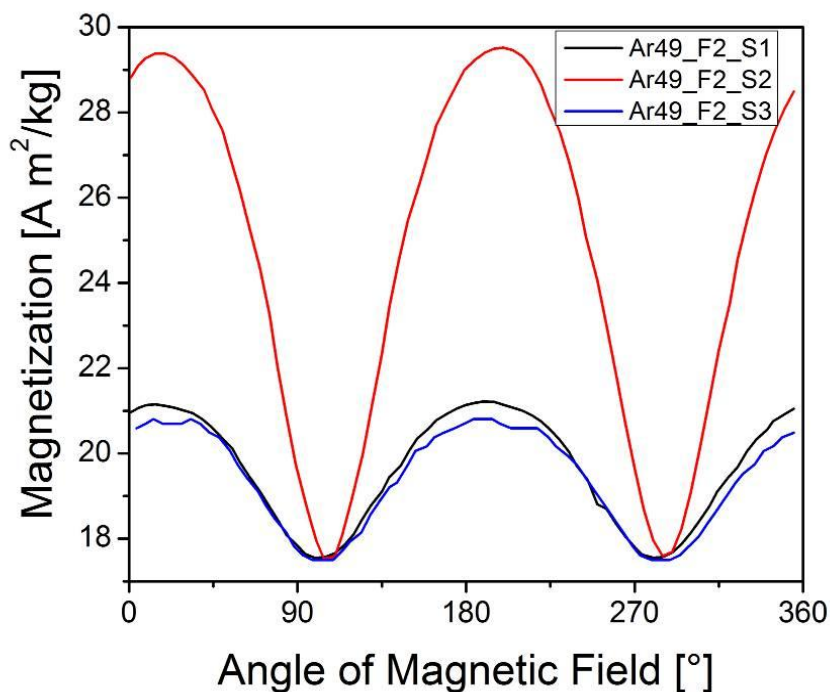
**Figure 5.24 Magnetic Field Orientation Dependent Magnetization for (a)
AR49_F2_S1, (black curve), AR49_F2_S2 (red), and AR49_F2_S3 (blue) Using a
Magnetic Field of 100mT Rotated Around the *x* Axis of the Sample.**

Field dependent magnetization measurements were done at the angles that gave

minimum and maximum magnetizations. Once corrected for shape anisotropy the curves

taken at the hard (minimum magnetization) and easy (maximum magnetization) direction

of magnetization (102 ° and 12 ° respectively) almost perfectly overlap for AR49_F2_S1

indicating that the magneto crystalline anisotropy was very small (Figure 5.25a).

Conversely for AR49_F2_S2, after correction for shape anisotropy, there exists a large

area between the easy direction (18 °) and hard direction (108 °) of magnetization

indicating magneto crystalline anisotropy is large (Figure 5.25b). Since AR49_F2_S3

showed the smallest change in magnetization during the low field anisotropy

measurements no saturation magnetization measurements were done, as similar results to

AR49_F2_S1 were expected.
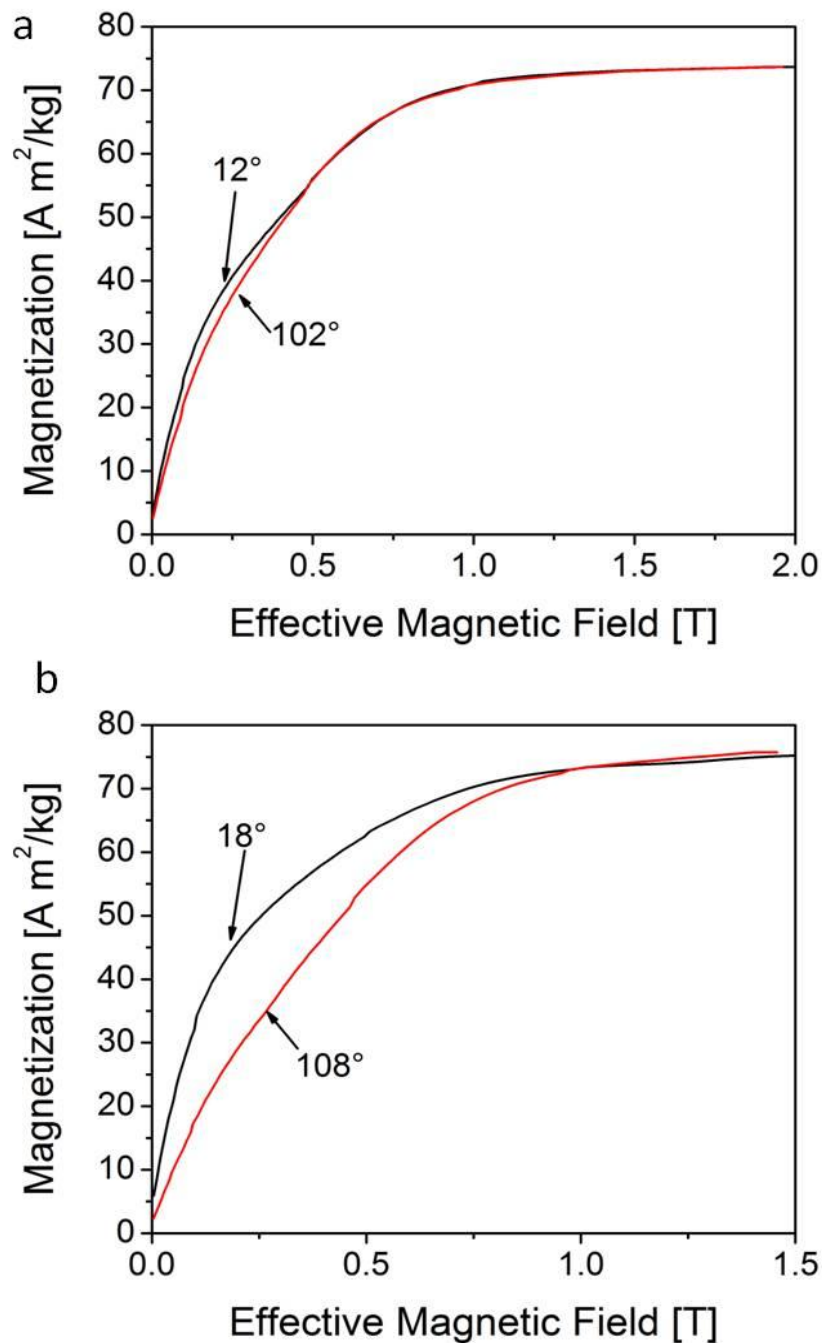
Figure 5.25 Magnetic Field Dependent Magnetization at the Easy and Hard Directions of Magnetization of the *y-z* Sample Plane, Found from Angle Dependent Magnetization Measurements. a) AR49_F2_S1 where Field was Applied 12 ° (Black) and 102 ° (Red) from the Long Axis of the Sample. b) AR49_F2_S2 where Field was Applied 18 ° (Black) and 108 ° (Red) from the Long Axis of the Sample.

X-ray tomography was done to see the distribution of small and large pores. Snapshots of pore distribution in the *yz* sample plane were taken at four depths (top, 1/3, 2/3 and the bottom) along the samples *x* direction. In AR49_F2_S1 (Figure 5.26) shows small pores are almost absent in the lower half of the sample. Also there are fewer large pores at the top of the sample as compared to the bottom. AR49_F2_S2 (Figure 5.27) shows the most even distribution of pores of the three samples. AR49_F2_S3 shows about the same area without small pores as AR49_F2_S1, again mostly in the lower half of the sample (Figure 5.28). However AR49_F2_S3 has a higher quantity of large pores in the top half of the sample than AR49_F2_S1.
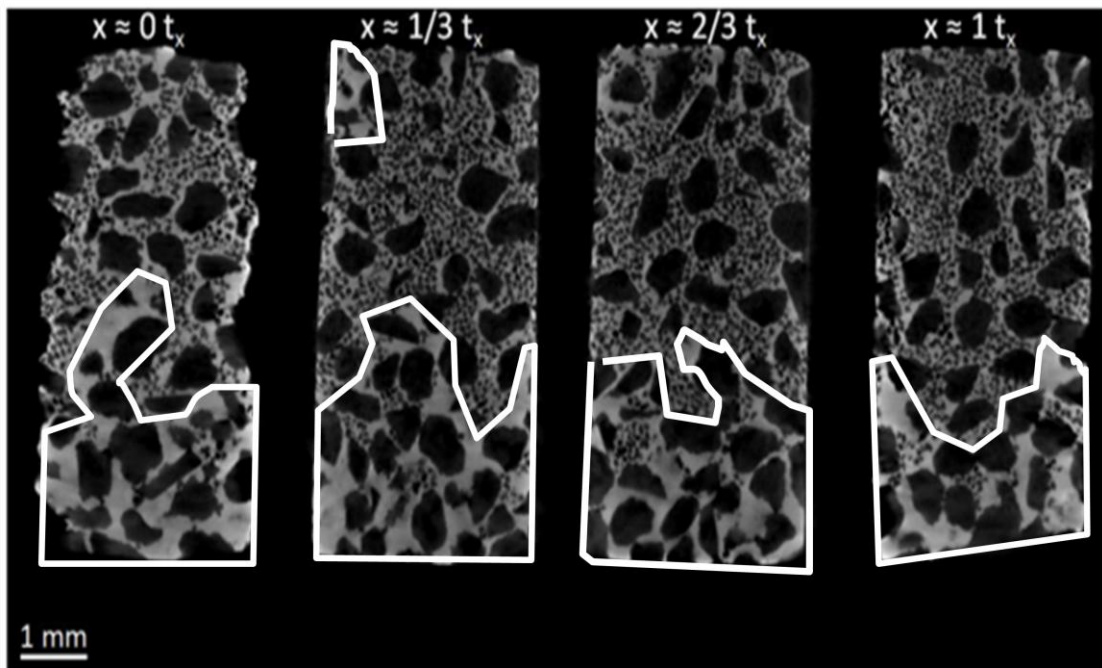
Figure 5.26 X-ray Tomography Showing Small and Large Pore Distributions of AR49_F2_S1. Pore Distributions are Show for the *yz* Sample Plane at Different Depths Along the Sample *x* Direction (t_x). Large Areas Absent of Small Pores are Outlined in White. Thanks to Dr. Chmielus for the Image.
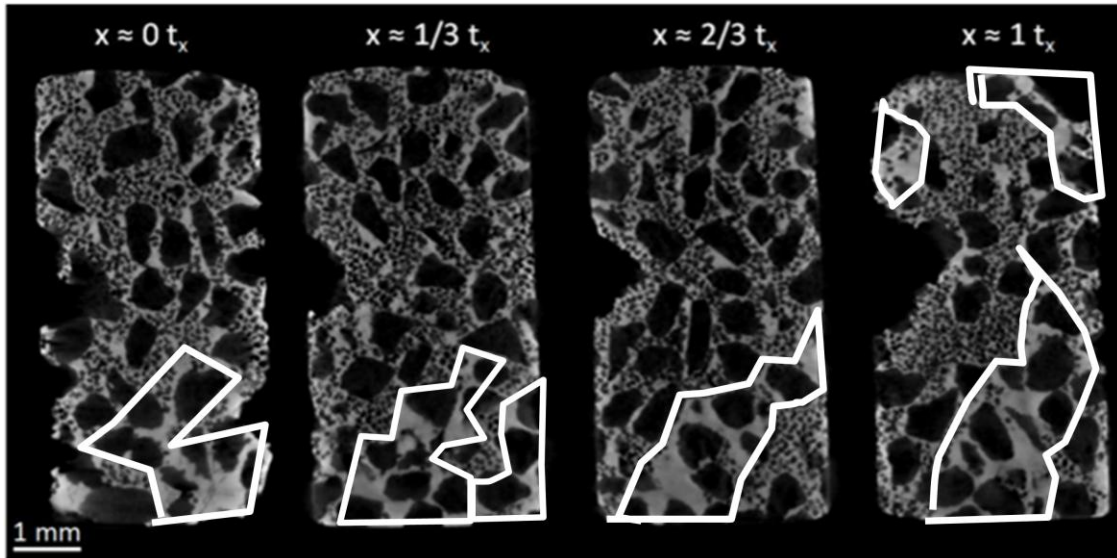
Figure 5.27 X-ray tomography showing small and large pore distributions of AR49_F2_S2. Pore distributions are show for the *yz* sample plane at different depths along the sample *x* direction (t_x). Large areas absent of small pores are outlined in white. Thanks to Dr. Chmielus for the image
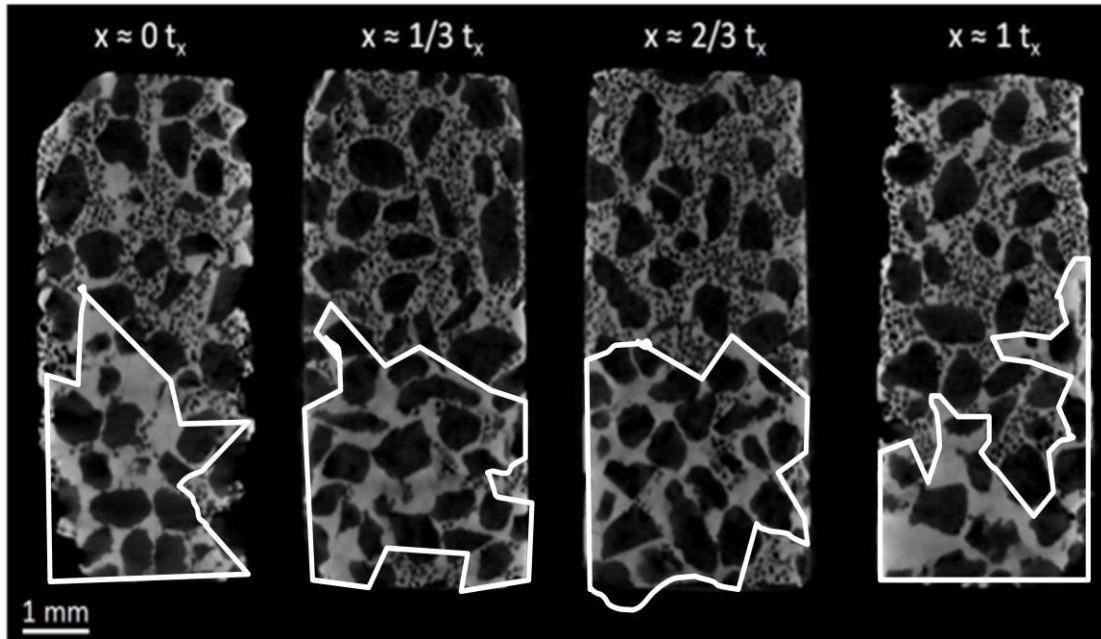
Figure 5.28 X-ray Tomography Showing Small and Large pore Distributions of AR49_F2_S3. Pore Distributions are Show for the *yz* Sample Plane at Different Depths Along the Sample *x* Direction (*t_x*). Large Areas Absent of Small Pores are Outlined in White. Thanks to Dr. Chmielus for the Image.

5.6 Size Effects on MFIS

A single pore sample AR75_K6_S2 (Figure 5.29 a) was magneto mechanically

cycled then cut in half to create two new smaller samples AR75_K6_S2_A (Figure 5.20

b) and AR75_K6_S2_B (Figure 5.29 c). Each of the smaller samples was magneto-

mechanically cycled and the field orientation dependent MFIS was compared for all three

samples shown in Figure 5.29 (a-c). In the initial large state the sample showed two strain

maximum of 0.007% at 44 and 126° for the first MMC. After cutting, AR75_K6_S2_A

showed a 0.013% increase in MFIS to 0.02% and one main strain peak at 44 ° with an

additional shoulder at field angles above 90 °. AR75_K6_S2_B showed one main strain

peak of 0.007% at 126 ° with an additional shoulder at field angles below 90 °.
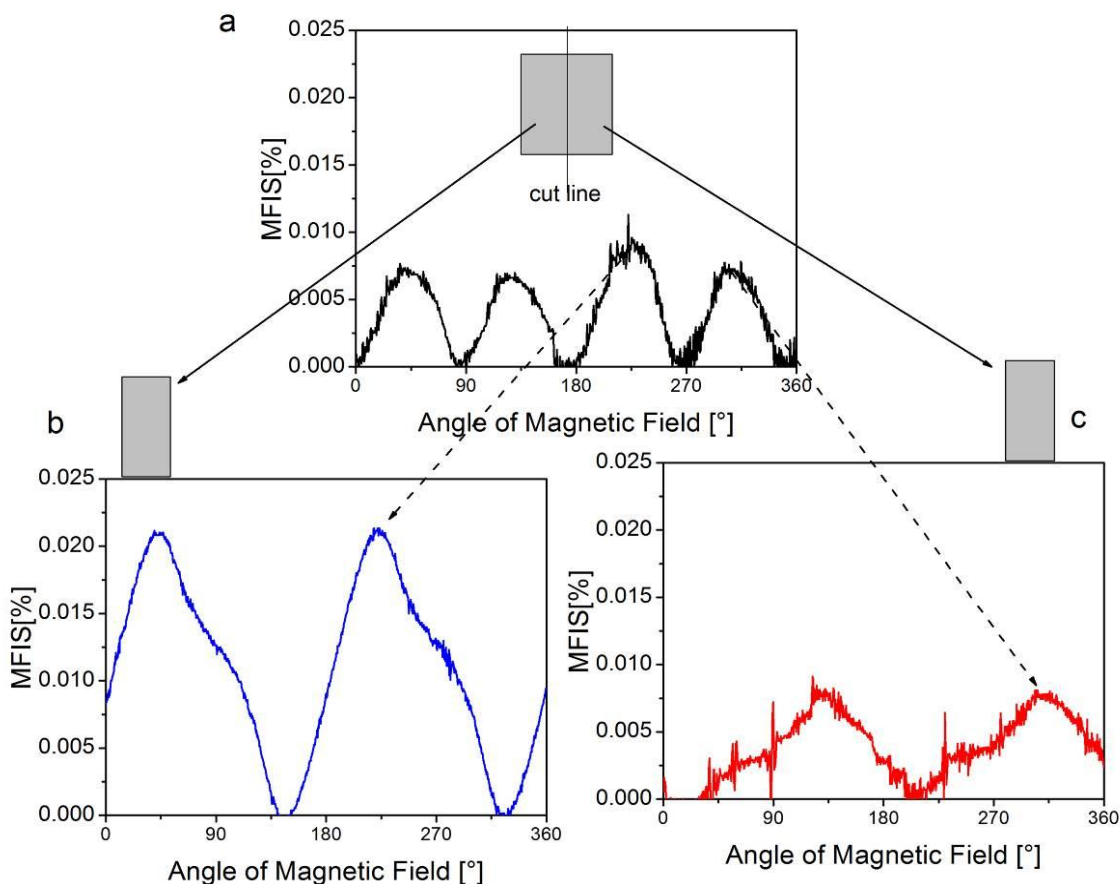
Figure 5.29 Size Effect Study on MFIS in Single Pore AR75_K6_S2. a) is the Initial Magneto-Mechanical Behavior for the Initial Size of the Sample (Grey Box). The Sample was then Cut in Half and Tested Separately (Solid Arrows) as AR75_K6_S2_A (b Blue) and AR75_K6_S2_B(c Red). Each Strain Peak Observed in the Initial Sample was Distributed to the Substituent Samples Shown by the Dotted Curve.

6   DISCUSSION

In the martensitic phase transformational effects on MFIS study, the samples investigated represent a host a variables such as composition, porosity, pore architecture, and pore distribution. Composition strongly effects the martensite transformation temperature [86]. Cherneko et al. found for Ni-Mn-Ga alloys that have the martensitic phase transformation temperature higher than the Curie temperature, during the onset of ferromagnetic ordering the material stiffened [55]. Therefore for AR20_D6(Figure 5.1) since the Curie temperature and austenite finish overlap the martensite would be stiffer causing twin boundary mobility to decrease [55]. Cherneko also found when the martensitic phase transformation temperature is below the Curie temperature, the elastic modulus decreases, as the transformation is approached. Therefore the material becomes more compliant at temperatures around the phase transformation[55]. If the metal is more compliant, twin boundary mobility increases thus enhancing the MFIS. This temperature dependence of twin boundary mobility has been demonstrated recently by Gaitzsch et al. [33] for textured polycrystals, where increasing the testing temperature to within 15K of the martensitic phase transformation, increased the MFIS by 0.7% [33, 55]. Thus higher MFIS may be achieved in samples with M_f temperatures that are close to the testing temperature of ~17 °C. This explains the tendency that samples with M_f close to ~17 °C show a higher MFIS as demonstrated in Figure 5.2.

From Figure 5.17 a relationship between porosity and MFIS was found,

independently, for three samples in the porosity study. G2_S1 showed a ten-fold increase

with a porosity increase of only 1.3%, which is a dramatic effect. Figure 6.1a shows a

porous frame work that can be thought of as a system of bridging metal called struts and

where struts connect called nodes. If strain is measured in the horizontal direction (arrow)

and a few struts are constrained such that no deformation can occur in them, these struts

can be thought of as "hard links" marked with a dashed line. If the hard links make up a

hard chain in the direction of the strain, the hard chain will inhibit the MFIS throughout

the whole network. The nodes or grain boundaries constrain a volume near the node,

since the twin boundary cannot move past the point of where the twin boundary interacts

with any constraint (illustrated in Figure 6.1b).[87, 88]. Etching will reduce the fraction

of constrained (or hard) volume (blue area in Figure 6.1b) and increase the volume of

unconstrained (or soft) material (dotted white line Figure 6.1b) within one strut.

Therefore if the strut cross section is reduced the twinning system can take up a larger

volume fraction in the strut. The unconstrained volume fraction (v_{free}) is:

$$v_{free} = 1 - \frac{w}{l}\tan(\alpha)$$

(16)

where w is the strut width l is the strut length and α is the angle between the twin

boundary and node. If a significant amount of hard links are broken or etched enough

such that connectivity of the hard chain is no longer maintained the deformation of the

whole network can deform to a much higher degree. In this way very little porosity

increase could be needed to achieve the effect of removing hard links in the bimodal

foam.
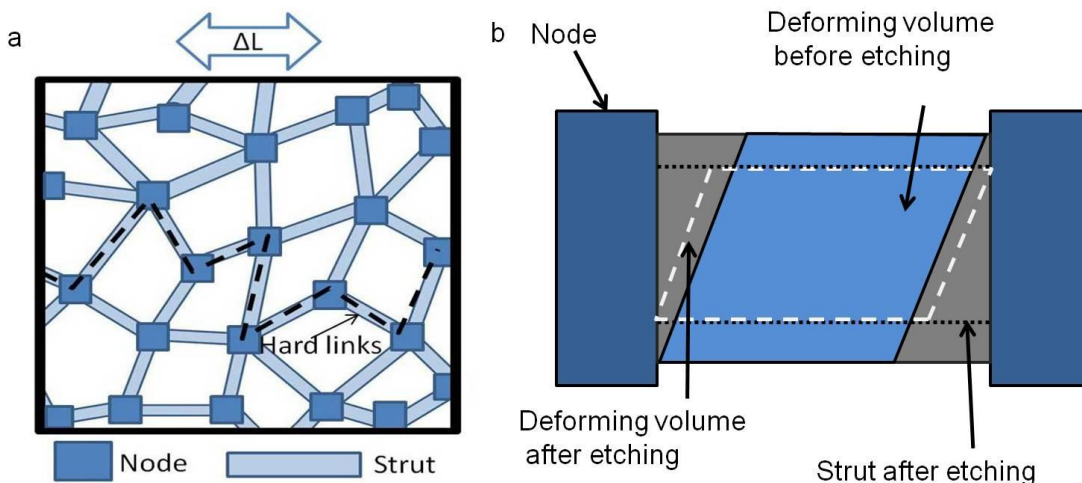
Figure 6.1 a) Porous Network of Struts and Nodes with Hard Link (Black Dashed Line) Strung Together in a Hard Chain. If the Strain (ΔL) is Measured in the Direction Marked by the Arrow, the Hard Chain will Not Allow Deformation to Occur. b) Representation of One Strut Node Complex where Dark Blue Squares are nodes. The Gray Area is the Strut before Etching. If the Struts are Assumed to be Single Crystalline with 45° Twin Boundaries the Corresponding Deformation Area is Shown in Blue. When the Strut is Etched or Thinned the Strut Width Decreases to the Dotted Line. For the Thinned Strut the Volume of Deformation Becomes the Area Outlined with the White Dashed Line.

This hard link concept may explain why G2_S1(porosity study) had such a

dramatic increase in MFIS with very little porosity increase. In Figure 5.18 G2-S1

initially showed no martensitic phase transformation hysteresis but a slow decline in

MFIS which might be expected due to the dependency of twin boundary motion on

temperature [89]. Severe cracking, (Figure 5.18 c) as discovered after TMC, is indirect

evidence that space holders were present during the initial testing. The crack ledges are

also displaced implying that the material deformed after being initially cracked,

suggesting the space holder was only present during the first TMC. During TMC the hard

ceramic restricted the deformation in the Ni-Mn-Ga metal, which was accommodated by

cracking within the metal. If the residual space holders were present during the first

testing, enough three dimension constraint could be imposed such that the sample did not

deform and therefore no martensitic phase transformation could be observed. During the

first etching the space holder was probably removed completely allowing the material to

be able to deform. The cracks along with the etching, thus broke the hard links and lead

to the dramatic increase in MFIS.

The porosity study showed that the width of the strut effects whether a strut is

hard or soft. Therefore pore architecture must be a large factor in determining

performance properties of the foam. Micrographs of the twin structures show that struts

in single pore foam are much thicker than struts in the dual pore foam (Figure 5.14).

Single pore struts show many twin variants and possibly grain boundaries, in contrast to

dual pore foam which show twins that span the thickness of the strut. Even though the

MFIS demonstrated between the mono-modal foam and the bimodal foam in the pore

architecture study (Figures 5.15 and 5.16 respectively) were similar, the strain reduction

rate with magneto-mechanical cycling was higher in the single pore foam as compared to

the dual pore foam. The high strain reduction rate of the single pore foam can be

attributed to a higher degree of twinning incompatibilies present in the thicker struts [7,

8, 17, 19, 67, 68, 87]. Twin boundary motion is easier in dual pore foam, due to a

reduction of the number of twin–twin interactions which lead to the creation of cracks[8,

68]. Also, because of strut and node size differences, cracks originating in the small dual pore foam struts do not propagate as far as those originating in the larger nodes and struts of the single pore foam. Incompatible twinning interactions and grain boundaries make thick struts "hard links". The single pore foam could have varying degrees of hard links depending of the twin microstructure within the strut which may be why the single pore foam can still display MFIS twice as large as previous single pore foam results[39] and on the same order of magnitude as the magnetostrictive material Terfenol D[23]. Dual pore foams have demonstrated up to 8.7% MFIS making the dual pore foam the best architecture investigated.

For all three samples tested in the porosity study the MFIS increased with increasing porosity though the strength of the effect varied considerably (Figure 5.17). Samples tested in the porosity study had compositions within experimental error of each other (Table 5.2), demonstrating that composition was not a factor affecting the rate of MFIS increase with porosity increase. The different rate of MFIS increase with porosity increase could be due to crystallographic texture and/or pore distribution. The samples in the porosity study display varying degrees of magneto crystalline anisotropy energy (Table 5.3) from 20% to 5% of a single crystal of Ni-Mn-Ga. The varying magneto crystalline anisotropy energy therefore demonstrates different levels of crystallographic textures. It is well know that texture in polycrystalline materials can enhance MFIS [32, 33, 36-38, 90]. Further, equation 16 shows the free deformation volume is dependent on

the twin orientation within the struts (α). The twin orientation within the strut dictates the rate of free volume increase with strut thinning.

In the pore distribution study it was found that samples with homogenously distributed large and small pores showed much higher MFIS than samples in which pore segregation dominated the architecture. F2_S2 the sample with the most uniform pore distribution out of the Ar49 foams(Figure 5.27) and also showed the highest magnetic anisotropy indicating(Figure 5.24) a higher degree of texture than the other two samples. F2_S2 also showed a notable increase in MFIS with thermo magneto-mechanical cycling (i.e. a training effect),(Figure 5.22) . In Figure 5.26, Figure 5.27, Figure 5.28 the areas outlined in white, are struts that are not filled with small pores. The struts enclosed in the white area, therefore show much thicker struts. Both F2_S1 and F2_S3 (Figures 5.26 and 5.28) showed almost half of the sample was devoid of smaller pores. However F2_S3 shows a higher amount of large pores evenly distributed, where F2_S1 has large sections filled mostly with small pores. During TMC, F2_S3 showed a MFIS of 0.37% that was stable for a wide temperature range(Figure 5.23) where F2_S1 showed 0.25% for a very narrow temperature window (Figure 5.21). Both F2_S1 and F2_S3 show little anisotropy (Figure 5.24) and little training effect. In the bimodal foam the struts that are missing the small pores are much larger and are similar to the struts see in the mono-modal foam. The large struts in the bimodal foam likely have incompatible twin-twin interaction as well as a higher chance of containing grain boundaries. In essence the large struts that are devoid of small pores are most likely hard links and the pore distribution dictates the population

and position of the hard links. The presence of texture seems to correlate to the trainability as the foam with the highest anisotropy shows the highest training effect and vice versa. However anisotropy isn't the only factor in MFIS as F2_S3 showed 3% lower anisotropy than F2_S1 but ~0.1% higher MFIS, indicating that the pore distribution plays a significant role in controlling MFIS.

The porosity distribution may also have a large impact on how effective etching relieves constraints and could be another reason for different MFIS vs porosity slopes. The distribution of thick struts not only would give the absolute population of hard links but the spatial arrangement of hard links. Hard links that are close to one another would form a chain which can be "broken" by etching or cracking as discussed above. On the other hand if a hard link is isolated it probably contributes less to the entire constraint on the strut network.

Training may be another method for reducing the number of hard links in the network of struts. There were three types of training investigated in this study: magneto mechanical, thermo-magnetic, and thermo magneto-mechanical training. Magneto mechanical training occurs from moving twin boundaries eliminating unfavorable twin variants.[7, 17, 19] Magneto mechanical training was only seen in a small percentage of foam(Figure 5.3). The lack of magneto mechanical training in MSM dual pore foam could be due to the limited volume of the struts such that there is less interacting twinning systems, which was discussed above in regards to the pore architecture study.

During thermo-magnetic training the applied field reduces the energy for martensite to form such that the direction of easy magnetization is aligned with the applied field. In thermo-magnetic training the number of twinning systems are reduced which results in a reduction of incompatible, intersecting twins [7, 17, 19]. Thermo-magnetic training resulted in a wide variety of effects and presented here are only a few possible explanations for the phenomenon observed. Detailed studies on microstructural evolution are needed to further substantiate the ideas presented below.

In most cases thermo-magnetic training showed an increase in MFIS (Figure5.7). A great example of the twin variant selection during thermo-magnetic training is for sample C2 (Figure 5.5). During initial testing the sample C2 showed a broad strain peak probably because there were multiple twin variants contributing to the deformation (Figure 5.5). After training the peak narrowed dramatically and the maximum MFIS now occurs at 90 °, as expected for twin boundary motion in a single crystal. The change is magneto mechanical behavior indicates some twinning systems were eliminated during the training. Subsequently the training was removed and as expected the MFIS drops below the initial MFIS. After neutralization C2 was trained a second and third time with very little increase in MFIS. The small increase in MFIS upon the 3rd training suggests that training could an additive effect. The lack of training response for the 2nd and 3rd trainings could be due to damage accumulation from magneto mechanical cycling.

The occurrence of two strain peaks per MMC (rather than a single peak expected from a single crystal) are not unusual and may reflect the polycrystalline nature of the foam (Figure 5.15, 5.29 and 5.9). Grains of different orientations in the foam nodes and struts, elongate and contract in different directions thus contributing differently to the average foam strain which is measured only in the z direction. Different foam deformation modes such as bending or hinging could also accommodate different directional strains from neighboring grains. The two strain peaks probably correspond to two dominant twin variants, possibly in different grains, expanding and contracting at specific magnetic field angles. One possible explanation for the dual peak phenomenon to be initiated, after thermo-magnetic training, is that prior to training, the twinning incompatibilities from multiple variants limit MFIS so much that each variant deforming was not distinguishable. Reduction of number of twin variants, by training, may be such that two dominant variants remain, each variant now able to freely deform thus distinguishable and results in two strain peaks per MMC.

In the size effect study when one, single pore foam was sectioned the two peaks per MMC, which were initially present, are split up between the sections of the sample (Figure 5.29). As the sample was sectioned the numbers of grains contributing to MFIS were distributed between the samples thereby distributing the strain peaks accordingly. The splitting of the MFIS peaks between the halved samples supports the claim that polycrystallinity is responsible for the dual peak phenomenon. Interestingly as

neighboring grains were removed the MFIS increased, further corroborating the claim that grain boundaries are responsible for reduced MFIS.

The multiple mechanisms of deformation within foam may allow deformation to be transmitted through "hard regions" in which twinning is not possible. Such a mechanism would not be available in bulk materials. In an open cell porous material of a MSMA not all struts can deform in the same direction. Thus, if a strut or groups of struts deform by twin boundary motion the surrounding area of struts can "allow" for the twin induced deformation by strut bending or buckling. Secondly any twin boundary motion in the nodes may initiate hinging. Hinging could result in very large strains at the ends of the strut with very little displacement at the hinge point. All of the deformation modes described essentially allows each grain and each strut to deform via twin boundary motion to the highest degree.

In the samples that showed strains less than 0.1% half of the cases thermo-magnetic training would result in a maximum strain shift to an angle that is not associated with twin boundary motion(~0 and 180°) for a single crystal (Figure5.8). For usual twin boundary motion 0 and 180 degrees would correspond to a minimum as the short lattice parameter of the crystal would be aligned with the long axis of the sample. Chopra et al. reported twin microstructures for bent and unbent single crystal martensites[91]. If the bent microstructure (Figure 6.2 a,b) was placed into a magnetic field aligned with the long axis parallel to the magnetic field the twin boundaries would move resulting is the

3D microstructure detailed in Figure 6.2 d. Due to variant coarsening the twin boundary

on the corners would be disappear. In single crystals the lack of twin boundaries on the

corners and edges often result in a kinked shape [87]. This kinking may occur in the

struts of the foam and therefore result in a positive strain at a field angle of 0 °. The strut

dimensional change from kinking would be very small and is probably why this effect

was only seen in low MFIS, low porosity samples. The kinking effect could also be

initiated in non bent or normal microstructures, after twin boundary motion, but would

occur at 90 °. The kink formation may initiate other forms of deformation such as hinging

where the struts bend or hinged about a fixed point such as a node as described above.
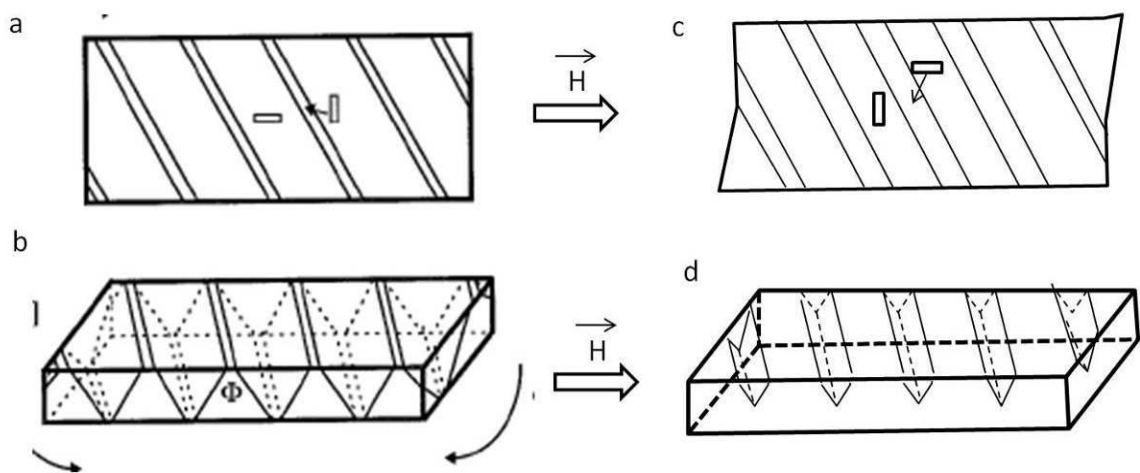
Figure 6.2 Bent Martensite Microstructures as Seen from Top (a) and Three Dimensionally (b) where Squares Indicate the Unit Cell Orientation. If the Bent Microstructure has a Magnetic Field Applied Parallel to the Long Axis as Shown by the Arrow, the Resulting Microstructures where c is the Top View and d is Three Dimensional Would be Found. Adapted and Reprinted with Kind Permission from [91].

Thermo magneto-mechanical training is performed by heating and cooling through the martensitic phase transformation in the presence of a rotating field. Not only is one twinning system preferred during the martensite formation by the application of a magnetic field but additionally the rotating field selects twining systems that are also mobile in the plane of the rotating field. For one sample AR20_C13 both thermo magneto-mechanical (Figure 5.11) and thermo-magnetic training (Figure 5.10) effectiveness's were compared. Thermo-magnetic training resulted in an increase in MFIS of 1.5%. When the same sample was thermo magneto-mechanically trained with over 4 H/C cycles the MFIS increased by a total of 7%. However trainings could have an additive effect as seen for C2 and thus the comparison of training methods may be hampered. Nonetheless this study shows that TMC could be one of the most effective means of training MSMA.

In the porosity study, G2-S1 also showed a clear training effect from TMC demonstrated by an increase in maximum MFIS with each H/C cycle. In Figure 5.18 b the first H/C cycle follows the same MFIS vs temperature path while in the martensite phase for both heating and cooling curves. However after the first H/C cycle the heating and cooling curves do not follow the same path. In the first H/C cycle the foam is most likely self accommodated which would explain the slowly decreasing MFIS until the phase transformation. Incompatible twinning systems interfere with each other as rotation of the magnetic field proceeds [7, 17, 68, 77]. After the first H/C cycle the foam is now in a trained state, showing constant MFIS until the martensite to austenite transformation.

Once trained it is possible that during cooling with a rotating field certain twinning

systems become inactive and remain inactive even upon heating [7, 17, 68, 77].

Figure 5.19 shows one H/C cycle for TMC for multiple porosities of I2_S2. The

maximum level of MFIS from lower porosity to higher porosity increased as well as the

martensitic phase transformation hysteresis changes. Both the change in the MFIS and

the change in the martensitic phase transformation hysteresis could be explained by

removal of the hard links. At the lower porosities 54.8% and 56.6% the martensitic phase

transformation hysteresis occur over a wide temperature range and active cooling only

gradually increases MFIS. In fact the highest strain of the thermal cycle occurs during

heating at the lower porosities. This is in stark contrast to I2_S2 at 60.3% porosity, there

is a sharp increase in MFIS upon cooling and the martensitic phase transformation

hysteresis narrows. The presence of the hard links could act as three dimensional

constraints for the whole foam network and require more undercooling for the martenistic

phase transformation to be complete. Overall in light of the hard link concept, the

variations between the thermo magneto-mechanical training and hysteresis of various

foams probably reflect the effects of various distributions of hard links due to

combinations of grain orientations and sizes and grain boundary location.

Each sample experienced failure after the final etching step of the porosity study.

Ni alloys are easily passivated by a chemiadsorbed layer of either sulfur or oxygen; since

Ni-Mn-Ga is 50% Ni the same could be true for the alloy as well [92-94]. Local

breakdown of the passive layer in the deformation area, may be appreciable during magnetic field induced deformation. The regions of breakdown in the chemiadsorbed layer may be etched at a much higher rate that the surrounding area. Therefore the combination of etching and deformation experiments contributed to low etching cycle lifetime of these samples.

X-ray texture measurements (Figure 5.12) showed that there are 5 or more grains that were detected over the probed area of ~12 mm^2 meaning grains are in the mm size range. If grains are millimeter sized there could be 10 or more grains in the volume of the sample and therefore still be considered polycrystalline. X-ray texture and neutron diffraction experiments show detectable intensity shifts demonstrating the texture could be used to see the volume fraction changes that occur during training. Texture has to potential to quantify the training effects but need more work to be able to successfully use the results.

7   CONCLUSIONS

Variables that affect the performance of polycrystalline Ni-Mn-Ga foam were identified and investigated. Variables investigated include martensitic phase transformation temperature, pore architecture, pore distribution, porosity, training, and magnetic anisotropy/texture. A concept of a network of strut with hard links was developed to correlate these variables with the effect on MFIS. A hard link is a strut that is unable to deform, and further the presence of the hard link reduces the ability for the whole strut network to deform. A slight correlation between MFIS and M_f was found. The metal is more compliant when the temperature starts to approach the martensitic phase transformation and contains fewer hard links. The smaller struts in the bimodal foam have less twin interaction that create cracking and therefore sustain less damage accumulation. Dual pore foam has far less hard links than the single pore foam, due to twin incompatibility reduction in the thinner struts. However in dual pore foams homogenous pore distributions are crucial in lowering the population of hard links. Further the pore distribution drives the hard link distribution. The different hard link distributions could explain the variety of properties found in foam samples with identical (within experimental error) compositions. Systematically increasing porosity in foams with constant composition, grain size, and texture, shows that the addition of porosity to

polycrystalline Ni-Mn-Ga is responsible for the enhanced MFIS confirming the original hypothesis. Various forms of training were used to soften hard links. Magneto-mechanical training was only observed for a small percentage of samples probably due to the porosity screening the twin interactions. Thermo-magnetic training gave various results such as dramatic 34 fold increases, negative training effects, dual peak initiation, and peak maxima shifting. Thermo magneto-mechanical training showed the highest increase in MFIS and may the most efficient form of training.

With the variables that affect MFIS in Ni-Mn-Ga foam identified, it is possible to fabricate NMG foam with consistent microstructure and therefore consistent MFIS over a large number of cycles. By adjusting the foam microstructure and architecture MFIS may be tailored to the specific actuation application.

8   FUTURE WORK

In the future, foams may be manufactured with a powder metallurgy method and a salt space holder. In the powder metallurgy process, Ni-Mn-Ga powder is mixed with salt and hot pressed at temperatures less than the melting temperature. The method should allow for more grain size control by powder fabrication, easy dissolution of space holder (no acid needed), and limitation of Manganese and Gallium evaporation because materials are processed at a lower temperature than the replicate casting method. The powder will also be magnetically aligned prior to pressing to produce a texture and theoretical enhance the MFIS.

Further work is required to quantify textures of the foam samples. Once texture is quantifiable, variant selection through training could be investigated. Texture may also be employed for observing the effect of hot pressing on the preferred orientation of the sintered powders. Neutron diffraction texture during field rotation and at constant temperatures will be further analyzed to investigate the other deformation mechanism in cast foam, primarily hinging.

Optical observations of the twin boundaries moving in a rotating magnetic field with polarized light should be conducted to elucidate the magneto mechanical behavior

presented in the training section (section 5.2). An optical device for the above purpose is

built and implementation of the device in currently being developed

9   REFERENCES

[1]   F. Heusler, "uber magnetische Manganlegrierungen," 1903.

[2]   J. W. Buehler, "WOL Oral History Supplement, NITINOL Re-Examination," in
        <*http://www.wolaa.org/files/Nitinol_Oral_History.pdf>*. vol. 8: WOLAA LEAF,
        2006.

[3]   J. Enkovaara, A. Ayuela, A. T. Zayak, P. Entel, L. Nordström, M. Dube, J.
        Jalkanen, J. Impola, and R. M. Nieminen, "Magnetically driven shape memory
        alloys," *Materials Science and Engineering A,* vol. 378, pp. 52-60, 2004.

[4]   O. Söderberg, Y. Ge, A. Sozinov, S. P. Hannula, and V. A. Lindroos, "Recent
        breakthrough development of the magnetic shape memory effect in Ni–Mn–Ga
        alloys " *Smart. Mater. Struct.,* vol. 14, 2005.

[5]   C. M. Wayman, *MRS Bulletin,* vol. 18, 1993.

[6]   *Shape Memory Materials*. Cambridge: Cambridge University Press, 1998.

[7]   P. Müllner, V. A. Chernenko, M. Wollgarten, and G. Kostorz, "Large cyclic
        deformation of a Ni-Mn-Ga shape memory alloy induced by magnetic fields. ," *J.
        Appl. Phys.,* vol. 92, 2002.

[8]   P. Müllner, D. Mukherji, M. Aguirre, R. Erni, and G. Kostorz, "Micromechanics
        of magnetic-field-induced twin-boundary motion in Ni-Mn-Ga magnetic shape-
        memory alloys," in *Solid-to-Solid Phase Transformations in Inorganic Materials*.
        vol. 2, J. M. Howe, D. E. Laughlin, J. K. Lee, U. Dahmen, and W. A. Soffa, Eds.:
        TMS, 2005, pp. 171-185.

[9]   R. C. O'Handley, S. J. Murray, M. Marioni, H. Nembach, and S. M. Allen,
        "Phenomenology of giant magnetic-field-induced strain in ferromagnetic shape-
        memory materials (invited)," *Journal of Applied Physics,* vol. 87, pp. 4712-4717,
        2000.

[10]   A. Sozinov, Y. Ezer, G. Kimmel, P. Yakovenko, D. Giller, Y. Wolfus, Y.
        Yeshurun, K. Ullakko, and V. K. Lindroos, "Large magnetic-field-induced strains
        in Ni-Mn-Ga alloys in rotating magnetic field," *Journal De Physique Iv,* vol. 11,
        pp. 311-316, 2001.

[11]   K. Ullakko, J. K. Huang, C. Kantner, R. C. Ohandley, and V. V. Kokorin, "Large
        magnetic-field-induced strains in Ni2MnGa single crystals," *Applied Physics
        Letters,* vol. 69, pp. 1966-1968, 1996.

[12]   R. Kainuma, Y. Imano, W. Ito, Y. Sutou, H. Morito, S. Okamoto, O. Kitakami, K.
        Oikawa, A. Fujita, T. Kanomata, and K. Ishida, "Magnetic-field-induced shape
        recovery by reverse phase transformation," *Nature,* vol. 439, pp. 957-960, 2006.

[13] J. H. Zhang, W. Y. Peng, and T. H. H. Zuyao, "The magnetic field induced strain without prestress and with stress in a polycrystalline Mn--Fe--Cu antiferromagnetic alloy," *Applied Physics Letters,* vol. 93, pp. 122510-3, 2008.

[14] R. D. James and M. Wuttig, "Magnetostriction of martensite," *Philosophical Magazine A,* vol. 77, pp. 1273 - 1299, 1998.

[15] B. Kiefer, H. E. Karaca, D. C. Lagoudas, and I. Karaman, "Characterization and modeling of the magnetic field-induced strain and work output in Ni2MnGa magnetic shape memory alloys," *Journal of Magnetism and Magnetic Materials,* vol. 312, pp. 164-175, 2007.

[16] S. J. Murray, M. Marioni, S. M. Allen, R. C. O'Handley, and T. A. Lograsso, "6% magnetic-field-induced strain by twin-boundary motion in ferromagnetic Ni--Mn--Ga," *Applied Physics Letters,* vol. 77, pp. 886-888, 2000.

[17] P. Mullner, V. A. Chernenko, and G. Kostorz, "Large cyclic magnetic-field-induced deformation in orthorhombic (14M) Ni--Mn--Ga martensite," *Journal of Applied Physics,* vol. 95, pp. 1531-1536, 2004.

[18] A. Sozinov, A. A. Likhachev, N. Lanska, and K. Ullakko, "Giant magnetic-field-induced strain in NiMnGa seven-layered martensitic phase," *Applied Physics Letters,* vol. 80, pp. 1746-1748, 2002.

[19] P. Müllner, V. A. Chernenko, and G. Kostorz, "Stress-induced twin rearrangement resulting in change of magnetization in a Ni-Mn-Ga ferromagnetic martensite," *Scripta Materialia,* vol. 49, pp. 129-133, 2003.

[20] M. Pasquale, "Mechanical sensors and actuators," *Sensors and Actuators A: Physical,* vol. 106, pp. 142-148, 2003.

[21] R. Tickle and R. D. James, "Magnetic and magnetomechanical properties of Ni2MnGa," *Journal of Magnetism and Magnetic Materials,* vol. 195, pp. 627-638, 1999.

[22] A. Vassiliev, "Magnetically driven shape memory alloys," *Journal of Magnetism and Magnetic Materials,* vol. 242-245, pp. 66-67, 2002.

[23] S. A. Wilson, R. P. J. Jourdain, Q. Zhang, R. A. Dorey, C. R. Bowen, M. Willander, Q. U. Wahab, S. M. Al-hilli, O. Nur, E. Quandt, C. Johansson, E. Pagounis, M. Kohl, J. Matovic, B. Samel, W. van der Wijngaart, E. W. H. Jager, D. Carlsson, Z. Djinovic, M. Wegener, C. Moldovan, R. Iosub, E. Abad, M. Wendlandt, C. Rusu, and K. Persson, "New materials for micro-scale sensors and actuators: An engineering review," *Materials Science and Engineering: R: Reports,* vol. 56, pp. 1-129, 2007.

[24] N. N. Sarawate and M. J. Dapino, "Ferroelectric ceramics: History and technology," *Appl Phys Lett* vol. 93, 1999.

[25] J. R. Cullen, A. E. Clark, and K. B. Hathaway, *Handbook of materials science*. Amsterdam: VCH, 1997.

[26] M. Richard, J. Feuchtwanger, D. Schlagel, T. Lograsso, S. M. Allen, and R. C. O'Handley, "Crystal structure and transformation behavior of Ni-Mn-Ga martensites," *Scripta Materialia,* vol. 54, pp. 1797-1801, 2006.

[27]   D. L. Schlagel, Y. L. Wu, W. Zhang, and T. A. Lograsso, "Chemical segregation during bulk single crystal preparation of Ni-Mn-Ga ferromagnetic shape memory alloys," *Journal of Alloys and Compounds,* vol. 312, pp. 77-85, 2000.

[28]   S. H. Guo, Y. H. Zhang, J. L. Li, B. Y. Quan, Y. Qi, and X. L. Wang, "Martensitic transformation and magnetic-field-induced strain in magnetic shape memory alloy NiMnGa melt-spun ribbon," *Journal of Materials Science & Technology,* vol. 21, pp. 211-214, 2005.

[29]   P. Lazpita, G. Rojo, J. Gutierrez, J. M. Barandiaran, and R. C. O'Handley, "Correlation between magnetization and deformation in a NiMnGa shape memory alloy polycrystalline ribbon," *Sensor Letters,* vol. 5, pp. 65-68, 2007.

[30]   M. Pasquale, C. Sasso, S. Besseghini, E. Passaretti, E. Villa, and A. Sciacca, "NiMnGa polycrystalline magnetically activated shape memory alloys," *Ieee Transactions on Magnetics,* vol. 36, pp. 3263-3265, 2000.

[31]   U. Gaitzsch, M. Potschke, S. Roth, N. Mattern, B. Rellinghaus, and L. Schultz, "Structure formation in martensitic Ni50Mn30Ga20 MSM alloy," *Journal of Alloys and Compounds,* vol. 443, pp. 99-104, 2007.

[32]   U. Gaitzsch, M. Potschke, S. Roth, B. Rellinghaus, and L. Schultz, "Mechanical training of polycrystalline 7 M Ni50Mn30Ga20 magnetic shape memory alloy," *Scripta Materialia,* vol. 57, pp. 493-495, 2007.

[33]   U. Gaitzsch, M. Potschke, S. Roth, B. Rellinghaus, and L. Schultz, "A 1% magnetostrain in polycrystalline 5M Ni-Mn-Ga," *Acta Materialia,* vol. 57, pp. 365-370, 2009.

[34]   U. Gaitzsch, R. Roth, B. Rellinghaus, and L. Schultz, "Adjusting the crystal structure of NiMnGa shape memory ferromagnets," *J. Magn. Magn. Mater,* vol. 305, 2006.

[35]   U. Gaitzsch, R. Techapiesancharoenkij, M. Potschke, S. Roth, and L. Schultz, "Acoustic Assisted Magnetic Field Induced Strain in 5M Ni-Mn-Ga Polycrysts," *Ieee Transactions on Magnetics,* vol. 45, pp. 1919-1921, 2009.

[36]   M. Pasquale, C. P. Sasso, S. Besseghini, F. Passaretti, E. Villa, and V. A. Chernenko, "Effect of texturing on the magnetically activated properties of polycrystalline NiMnGa alloys," *Journal De Physique Iv,* vol. 11, pp. 305-309, 2001.

[37]   M. Potschke, U. Gaitzsch, S. Roth, B. Rellinghaus, and L. Schultz, "Preparation of melt textured Ni-Mn-Ga," *Journal of Magnetism and Magnetic Materials,* vol. 316, pp. 383-385, 2007.

[38]   M. Potschke, S. Weiss, U. Gaitzsch, D. Y. Cong, C. Hurrich, S. Roth, and L. Schultz, "Magnetically resettable 0.16% free strain in polycrystalline Ni-Mn-Ga plates," *Scripta Materialia,* vol. 63, pp. 383-386.

[39]   Y. Boonyongmaneerat, M. Chmielus, D. C. Dunand, and P. Müllner, "Increasing Magnetoplasticity in Polycrystalline Ni-Mn-Ga by Reducing Internal Constraints through Porosity," *Physical Review Letters,* vol. 99, p. 247201, 2007.

[40]   S. Blundell, *Magnetism in condensed matter*. Oxford: Oxford University Presse, 2001.

[41]   D. Giles, *Introduction to magnetism and magnetic materials 2ⁿᵈ edition*. Boca Raton CRC Taylor and Francis, 1998.

[42]   W. D. Callister, *Materials Science and Engineering an Introduction*, 6th ed. Hoboken: John Wiley & Sons Inc., 2003.

[43]   B. M. Moskowitz, "Magneto Crystalline Anisotropy," in *Hitchhiker's Guide To Magnetism*, 1991.

[44]   J. Pons, R. Santamarta, V. A. Chernenko, and E. Cesari, "HREM study of different martensitic phases in Ni-Mn-Ga alloys," *Materials Chemistry and Physics,* vol. 81, pp. 457-459, 2003.

[45]   J. Pons, R. Santamarta, V. A. Chernenko, and E. Cesari, "Structure of the layered martensitic phases of Ni-Mn-Ga alloys," *Materials Science and Engineering: A,* vol. 438-440, pp. 931-934, 2006.

[46]   J. Pons, V. A. Chernenko, R. Santamarta, and E. Cesari, "Crystal structure of martensitic phases in Ni-Mn-Ga shape memory alloys," *Acta Materialia,* vol. 48, pp. 3027-3038, 2000.

[47]   U. Gaitzsch, M. Pötschke, S. Roth, N. Mattern, B. Rellinghaus, and L. Schultz, "Structure formation in martensitic Ni50Mn30Ga20 MSM alloy," *J. Alloys Compd.,* vol. 443, 2007.

[48]   A. A. Knowlton, "Preparation and Properties of the Heusler Alloys," *Physical Review (Series I),* vol. 32, p. 54, 1911.

[49]   O. Heczko, L. Straka, N. Lanska, K. Ullakko, and J. Enkovaara, "Temperature dependence of magnetic anisotropy in Ni-Mn-Ga alloys exhibiting giant field-induced strain," *Journal of Applied Physics,* vol. 91, pp. 8228-8230, 2002.

[50]   A. Sozinov, A. A. Likhachev, and K. Ullakko, "Crystal Structures and Magnetic Anisotropy Properties of Ni–Mn–Ga Martensitic Phases With Giant Magnetic-Field-Induced Strain," *IEEE Transactions on Magnetics,* vol. 38, 2002.

[51]   J. W. Christensen, "Thermodynamics and Kinetics of Martensite," in *ICOMAT*, 1979.

[52]   H. K. D. H. Bhadeshia, "Martensitic Transformations: Crystallography and Nucleation " in *Encyclopedia of Materials Science: Science and Technology*, K. Buschow, R. W. Cahn, M. C. Flemings, B. Lischner, E. J. Kramer, and S. Mahajan, Eds.: Pergamon Press: Elsevier Science, 2001, pp. 5203-5206.

[53]   P. Mullner and A. H. King, "Deformation of hierarchically twinned martensite," *Acta Materialia,* vol. 58, pp. 5242-5261.

[54]   V. A. Chernenko, E. Cesari, V. Khovailo, J. Pons, C. Seguí, and T. Takagi, "Intermartensitic phase transformations in Ni-Mn-Ga studied under magnetic field," *Journal of Magnetism and Magnetic Materials,* vol. 290-291, pp. 871-873, 2005.

[55]   V. A. Chernenko, J. Pons, C. Seguí, and E. Cesari, "Premartensitic phenomena and other phase transformations in Ni-Mn-Ga alloys studied by dynamical mechanical analysis and electron diffraction," *Acta Materialia,* vol. 50, pp. 53-60, 2002.

[56]   S. Kustov, J. Pons, E. Cesari, and J. Van Humbeeck, "Chemical and mechanical stabilization of martensite," *Acta Materialia,* vol. 52, pp. 4547-4559, 2004.

[57]   C. Seguí, V. A. Chernenko, J. Pons, E. Cesari, V. Khovailo, and T. Takagi, "Low temperature-induced intermartensitic phase transformations in Ni-Mn-Ga single crystal," *Acta Materialia,* vol. 53, pp. 111-120, 2005.

[58]   M. Palumbo, "Thermodynamics of Martensitic Transformations in the Framework of the CALPHAD Approach," *Calphad,* vol. 32, pp. 693-708, 2008.

[59]   M. L. Richard, J. Feuchtwanger, S. M. Allen, R. C. O'Handley, and P. L`azpita, "Martensite Transformation in Ni-Mn-Ga Ferromagnetic Shape-Memory Alloys," *Metallurgical And Materials Transactions A-Physical Metallurgy And Materials Science,* vol. 38A, pp. 777-780, 2007.

[60]   J. Rodríguez-Aseguinolaza, I. Ruiz-Larrea, M. L. Nó, A. López-Echarri, and J. S. Juan, "A New Quantitative Approach to the Thermoelastic Martensitic Transformation: The Density of Elastic States,," *Acta. Materialia,* vol. 56, pp. 6283-6290, 2008.

[61]   S. Zhang and P. G. McCormick, "Thermodynamic Analysis of Shape Memory Phenomena – I. Effect of Transformation Plasticity on Elastic Strain Energy, ," *Acta Materialia,* vol. 48, pp. 3081-3089, 2000.

[62]   K. Ullakko, J. K. Huang, C. Kanter, V. V. Kokorin, and R. C. Ohandley, "Magnetic-field-induced strain in Ni2MnGa shape-memory alloy," *Journal of Applied Physics,* vol. 81, pp. 5416-5416, 1997.

[63]   K. Ullakko, J. K. Huang, V. V. Kokorin, and R. C. Ohandley, "Magnetically controlled shape memory effect in Ni2MnGa intermetallics," *Scripta Materialia,* vol. 36, pp. 1133-1138, 1997.

[64]   V. A. Chernenko, M. Chmielus, and P. Mullner, "Large magnetic-field-induced strains in Ni-Mn-Ga nonmodulated martensite (vol 95, 104103, 2009)," *Applied Physics Letters,* vol. 95, 2009.

[65]   K. Ullakko, J. K. Huang, V. V. Kokorin, and R. C. O'Handley, "Magnetically controlled shape memory effect in Ni2MnGa intermetallics," *Scripta Materialia,* vol. 36, pp. 1133-1138, 1997.

[66]   L. Straka, N. Lanska, K. Ullakko, and A. Sozinov, "Twin microstructure dependent mechanical response in Ni--Mn--Ga single crystals," *Applied Physics Letters,* vol. 96, pp. 131903-3, 2010.

[67]   I. Aalito, A. Soraka, Y. Ge, O. Soderberg, and S. P. Hannula, "High cycle fatigue of 10M Ni-Mn-Ga magnetic shape memory alloy in reverse mechanical loading " *Smart. Mater. Struct.,* vol. 19, 2010.

[68]   M. Chmielus, V. A. Chernenko, W. B. Knowlton, G. Kostorz, and P. Müllner, "Training, constraints, and high-cycle magneto-mechanical properties of Ni-Mn-Ga magnetic shape-memory alloys," *Eur. Phys. J. Special Topics,* vol. 158, pp. 79-85, 2008.

[69]   T. H. Courtney, *Mechanical Behavior of Materials*. Long Grove: Waveland Press Inc., 2000.

[70]   N. Scheerbaum, O. Heczko, J. Liu, D. Hinz, L. Schultz, and O. Gutfleisch, "Magnetic field-induced twin boundary motion in polycrystalline Ni–Mn–Ga fibres," *New Journal of Physics,* vol. 10, 2010.

[71]   M. Ohtsuka, M. Matsumoto, K. Koike, T. Takagi, and K. Itagaki, "Martensitic transformation and shape memory effect of Ni-rich Ni2MnGa sputtered films under magnetic field," *Journal of Magnetism and Magnetic Materials,* vol. 310, pp. 2782-2784, 2007.

[72]   R. Chulist, W. Skrotzki, C. G. Oertel, A. Bohm, and M. Potschke, "Change in microstructure during training of a Ni50Mn29Ga21 bicrystal," *Scripta Materialia,* vol. 63, pp. 548-551.

[73]   D. C. Dunand and P. Mullner, "Size Effects on Magnetic Actuation in Ni-Mn-Ga Shape-Memory Alloys," *Advanced Materials,* vol. 23, pp. 216-232, Jan.

[74]   L. J. Gibson and M. F. Ashby, *Cellular Solids structure and properties* 2nd ed. Cambridge: Cambridge University Press, 1997.

[75]   S. L. Lopatnikov, B. A. Gama, M. Jahirul Haque, C. Krauthauser, J. W. Gillespie, M. Guden, and I. W. Hall, "Dynamics of metal foam deformation during Taylor cylinder-Hopkinson bar impact experiment," *Composite Structures,* vol. 61, pp. 61-71, 2003.

[76]   D. J. Craik and R. S. Tabbles, *Ferromagnetism and Ferromagnetic Domains*: North Holland Publishing, 1965.

[77]   M. Chmielus, "Training, microstructure an dmagneto-mechanical properites of Ni-Mn-Ga magnetic shape memory alloys," in *Materials Science and Engineering*. vol. Masters of Science Boise: Boise State University, 2007, p. 142.

[78]   G. E. Bacon, *Neutron Physics*. London: Wykeham Publisher, 1969.

[79]   G. E. Bacon, *Neutron Diffraction*. London: Oxford University Press, 1955.

[80]   J. Rhyne, "What's cool about Neutron Scattering, The Basics," in *LANSCE Neutron Scattering School* Los Alamos New Mexico, 2009.

[81]   M. Chmielus, C. Witherspoon, R. C. Wimpory, A. Paulke, A. Hilger, X. Zhang, D. C. Dunand, and P. Mullner, "Magnetic-field-induced recovery strain in polycrystalline Ni--Mn--Ga foam," *Journal of Applied Physics,* vol. 108, pp. 123526-7.

[82]   M. Chmielus, X. X. Zhang, C. Witherspoon, D. C. Dunand, and P. Mullner, "Giant magnetic-field-induced strains in polycrystalline Ni-Mn-Ga foams," *Nat Mater,* vol. 8, pp. 863-866, 2009.

[83]   Y. Boonyongmaneerat, M. Chmielus, D. C. Dunand, and P. Mullner, "Increasing magnetoplasticity in polycrystalline Ni-Mn-Ga by reducing internal constraints through porosity," *Physical Review Letters,* vol. 99, 2007.

[84]   P. Müllner, X. Zhang, Y. Boonyongmaneerat, C. Witherspoon, M. Chmielus, and D. C. Dunand, "Recent Developments in Ni-Mn-Ga Foam Research," in *International Conference on Ferromagnetic Shape Memory Alloys* vol. 635 Bilboa Spain: Materials Science Forum, 2010, pp. 119-124.
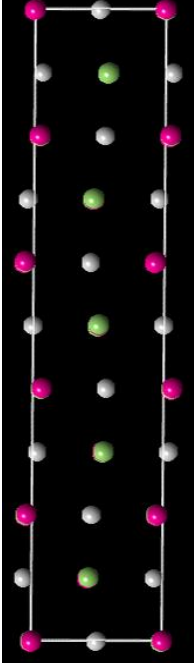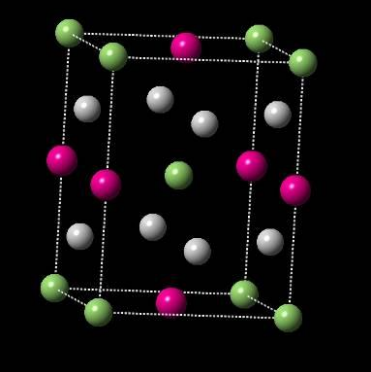
[85]   X. X. Zhang, C. Witherspoon, P. Müllner, and D. C. Dunand, "Effect of pore architecture on magnetic-field-induced strain in polycrystalline Ni-Mn-Ga," *Acta Materialia,* vol. 59, pp. 2229-2239.

[86]   C. Seguí, J. Pons, and E. Cesari, "Effect of atomic ordering on the phase transformations in Ni-Mn-Ga shape memory alloys," *Acta Materialia,* vol. 55, pp. 1649-1655, 2007.

[87]   M. Chmielus, I. Glavatskyy, J.-U. Hoffmann, V. A. Chernenko, R. Schneider, and P. Müllner, "Influence of constraints and twinning stress on magnetic field-induced strain of magnetic shape-memory alloys," *Scripta Materialia,* vol. In Press, Corrected Proof.

[88]   C. P. Henry, D. Bono, J. Feuchtwanger, S. M.Allen, and R. C. O'Handley, "ac field-induced acutuation of single crystal Ni-Mn-Ga," *J. App. Phys,* vol. 91, 2002.

[89]   O. Heczko and L. Straka, "Temperature dependence and temperature limits of magnetic shape memory effect," *Journal of Applied Physics,* vol. 94, pp. 7139-7143, 2003.

[90]   P. Lázpita, G. Rojo, J. Gutiérrez, J. M. Barandiaran, and R. C. O'Handley, "Correlation Between Magnetization and Deformation in a NiMnGa Shape Memory Alloy Polycrystalline Ribbon " *Sensor Letters,* vol. 5, p. 4, 2007.

[91]   H. D. Chopra, C. Bailly, and M. Wuttig, "Domain structures in bent In-22.5 at.%Tl polydomain crystals," *Acta Materialia,* vol. 44, pp. 747-751, 1996.

[92]   A. Gebert, S. Roth, S. Oswald, and L. Schultz, "Passivity of Polycrystalline NiMnGa Alloys for Magnetic Shape Memory Applications," *Corrosion Science,* vol. 51, p. 9, 2009.

[93]   P. Marcus and E. Protopapoff, "Potential pH Diagrams for Sulfur and Oxygen Adsorbed on Nickel in Water at 25 and 300C," *Journal of Electrochemical Society,* vol. 140, p. 5, 1993.

[94]   J. Osterwald and H. H. Uhlig, "Anodic Polarization and Passivity of Ni and Ni-Cu Alloys in Sulfuric Acid," *Journal of Electrochemical Society,* vol. 108, p. 5, 1961.

APPENDIX

Supplementary Crystallographic and Magneto-Mechanical Testing Data

Table A.1 Crystallographic Information for Ni$_2$MnGa Martensites.

	Space Group	Lattice Parameter	Atomic Positions				Illustration
14M	I2/m	a= 4.23Å b=5.50 Å c=29.7 Å β=93.5°	Ga	0	1/2	0	
			Ga	13/21	1	1/14	
			Ga	3/4	1/2	2/14	
			Ga	22/42	0	3/14	
			Ga	41/42	1/2	4/4	
			Ga	18/42	0	5/14	
			Ga	37/42	1/2	6/14	
			Mn	0	0	0	
			Mn	13/21	1/2	1/14	
			Mn	1/42	0	2/14	
			Mn	22/42	1/2	1/14	
			Mn	41/42	0	4/14	
			Mn	18/4	1/2	5/4	
			Mn	37/2	0	6/14	
			Ni	1/2	1/4	0	
			N	1/2	3/4	0	
			Ni	5/42	3/4	1/14	
			Ni	5/42	5/4	1/14	
			Ni	4/7	1/4	2/14	
			Ni	4/7	3/4	2/14	
			Ni	1/42	3/4	3/14	
			Ni	1/42	1/4	3/14	
			Ni	10/21	1/4	4/14	
			Ni	10/21	3/4	4/14	
			Ni	13/14	3/4	5/14	
			Ni	13/14	1/4	5/14	
			Ni	8/21	1/4	6/14	
			Ni	8/21	3/4	6/14	

10M	I2/m	a= 4.23Å b=5.57 Å c=21.5 Å β=90.5°	Ga	0.000	0.50	0.00	
			Ga	0.045	0.50	0.20	
			Ga	0.940	0.50	0.40	
			Mn	0.000	0.00	0.00	
			Mn	0.040	0.00	0.20	
			Mn	0.930	0.00	0.40	
			Ni	0.500	0.25	0.00	
			Ni	0.540	0.25	0.20	
			Ni	0.440	0.25	0.20	
NM	I4/mmm	a= 3.23Å c=5.98 Å	Mn	0	0	1/2	
			Ga	0	0	0	
			Ni	1/2	0	1/4	
			Ni	0	1/2	1/4	
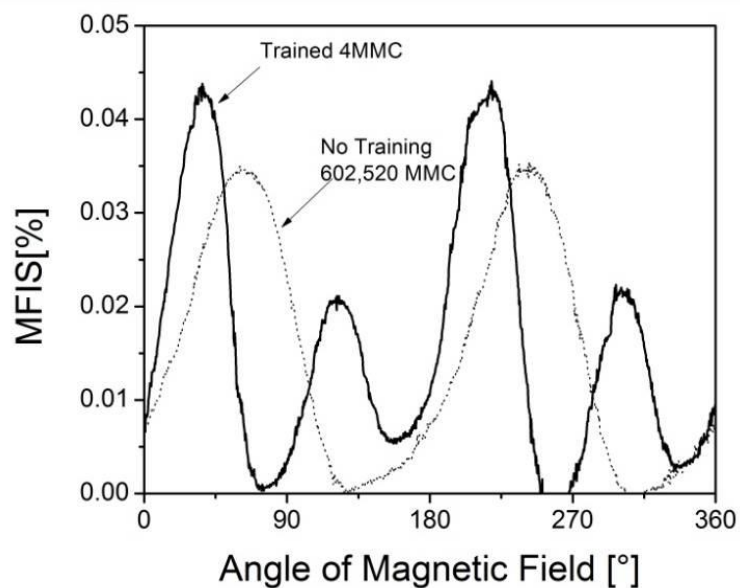
Figure A.1 8-1_b Effect of Thermo- Magnetic Training on MFIS.
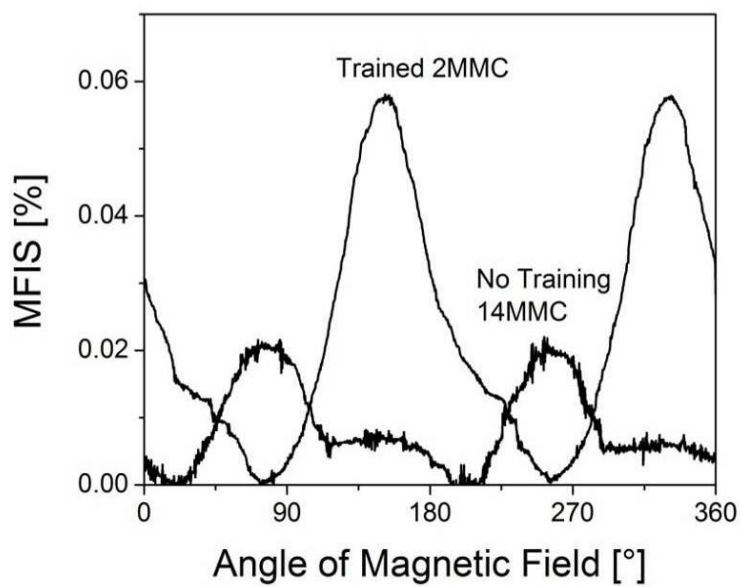
Figure A.2 4-8 H2SO4 Effect of Thermo-Magnetic Training on MFIS.
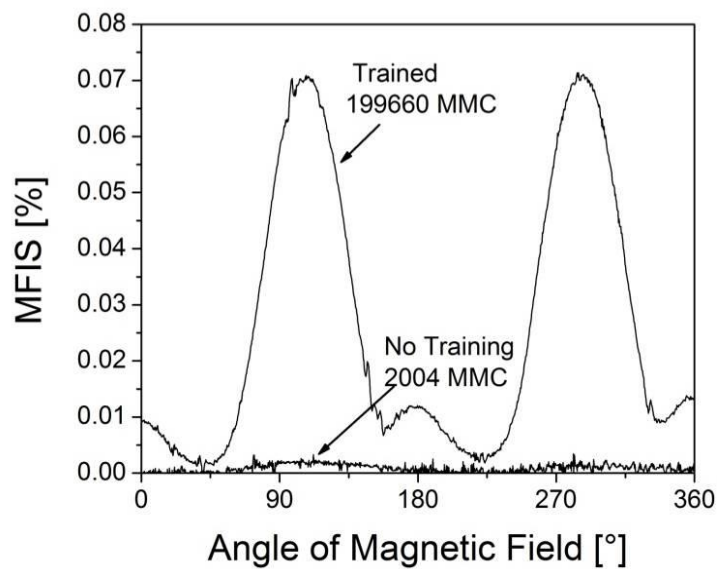
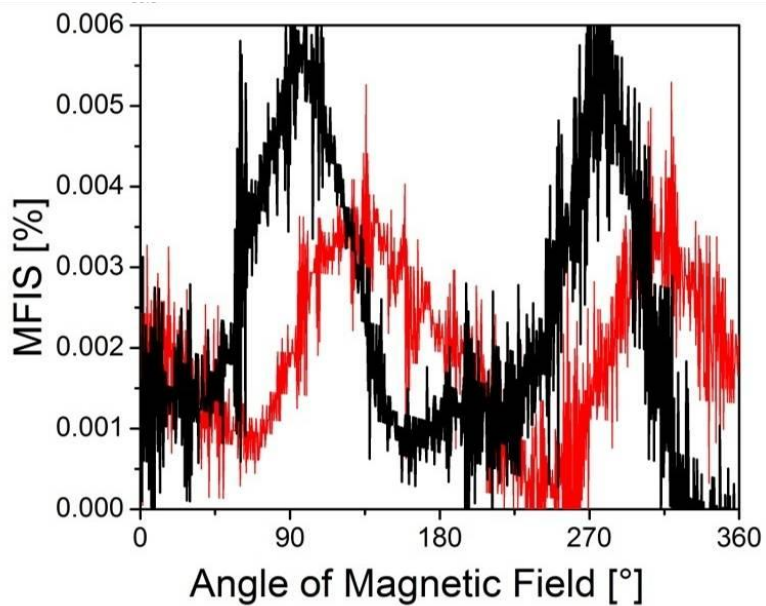**Figure A.3 4-23_3 Effect of Thermo- Magnetic Training on MFIS.**

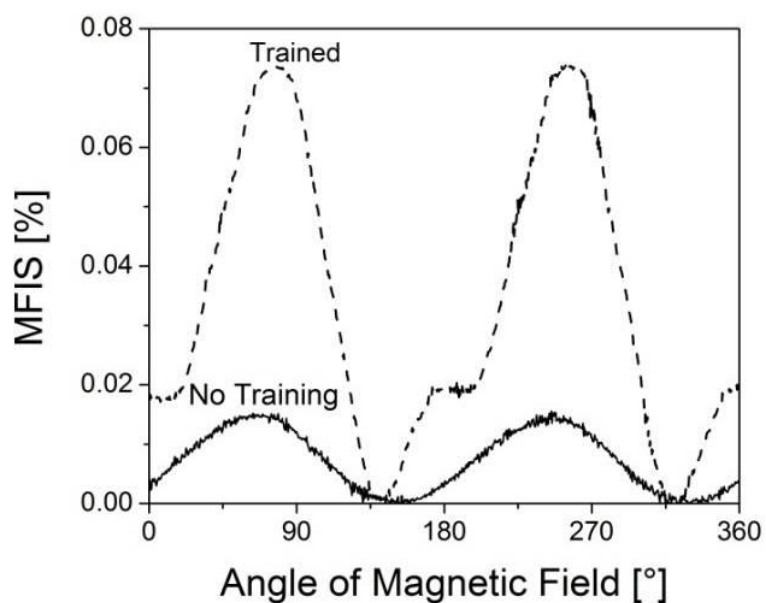**Figure A.4 8-1 HCL Effect of Thermo-Magnetic Training on MFIS.**

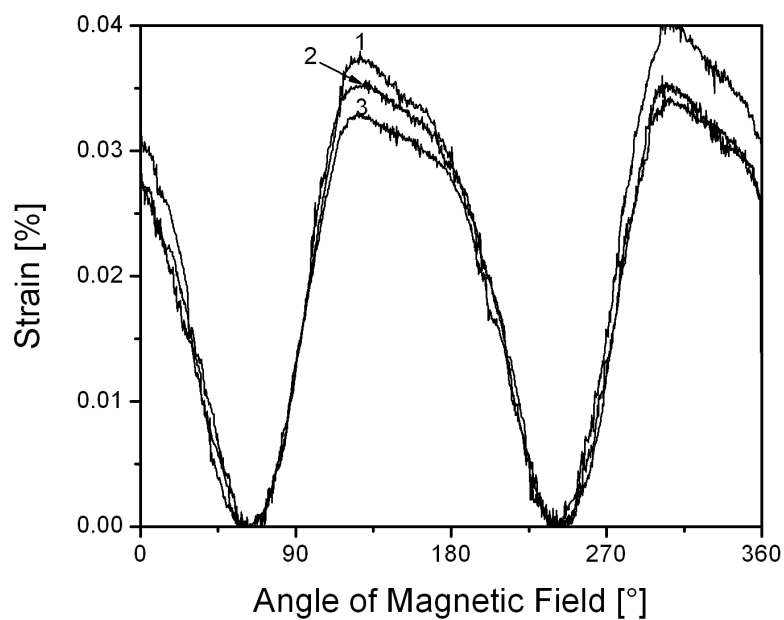**Figure A.5 8-1_a Effect of Thermo-Magnetic Training on MFIS.**

Figure A.6 Magneto-Mechanical Cycling of 8-1b. Curve 1 is 1120 MM Cycles, 2 is 200,000 MM Cycles, and 3 is 800,000 MM Cycles.
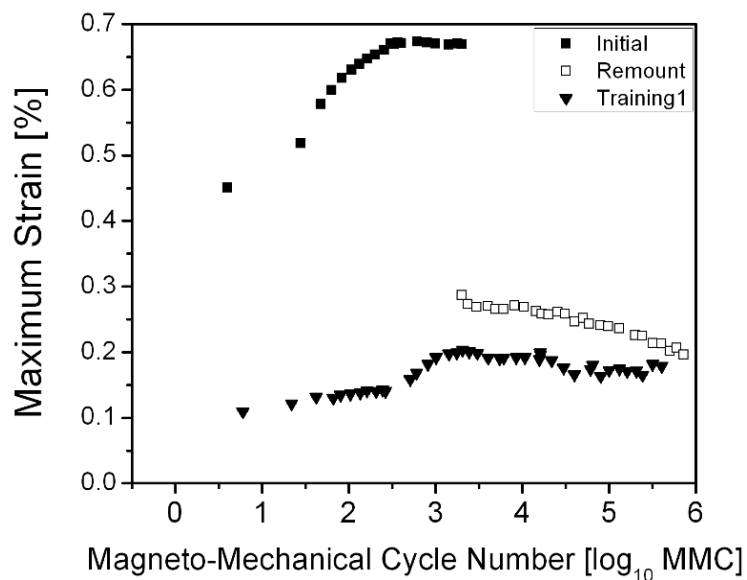
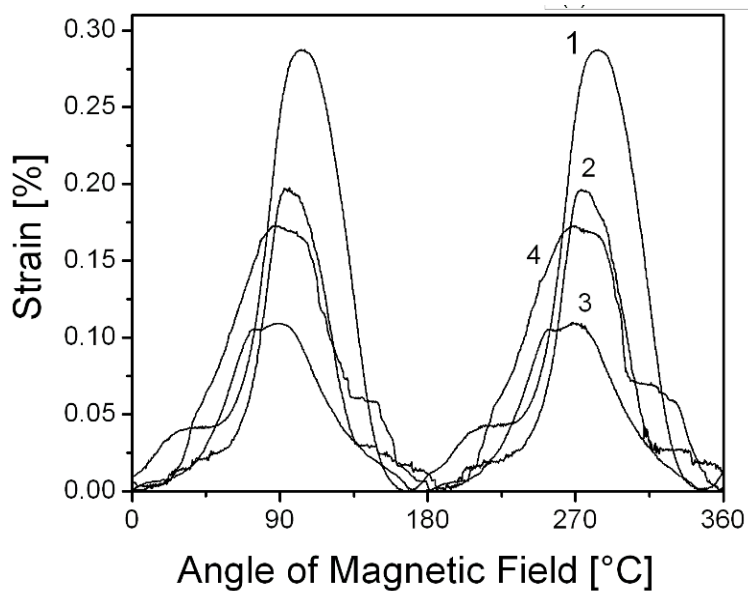**Figure A.7 Magneto-Mechanical Cycle Dependent MFIS of AR20_C11.**

Figure A.8 Magnetic Field Orientation Dependent MFIS of AR20_C11. 1) 1998 MMC, 2) 723442 MMC and after Training MMC Number 3) 2 MMC and 4) 40,1270 MMC.
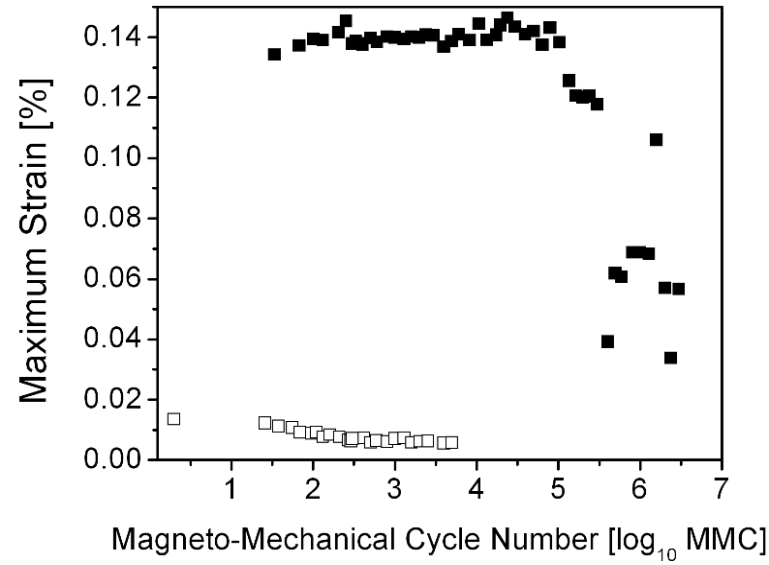
Figure A.9 Magneto-Mechanical Cycle Dependent MFIS of AR3_A2 in the Initial State (Black Squares) and Trained State (Open Squares)